LIÈGE université Library

http://lib.uliege.be https://matheo.uliege.be

Final work : Flutter wizard: development of an automatic tool for safety prediction in compressors and turbines

Auteur : Tavera Guerrero, Carlos
Promoteur(s) : Terrapon, Vincent
Faculté : Faculté des Sciences appliquées
Diplôme : Master en ingénieur civil en aérospatiale, à finalité spécialisée en "turbomachinery aeromechanics (THRUST)"
Année académique : 2018-2019
URI/URL : http://hdl.handle.net/2268.2/8339

Avertissement à l'attention des usagers :

Tous les documents placés en accès ouvert sur le site le site MatheO sont protégés par le droit d'auteur. Conformément aux principes énoncés par la "Budapest Open Access Initiative"(BOAI, 2002), l'utilisateur du site peut lire, télécharger, copier, transmettre, imprimer, chercher ou faire un lien vers le texte intégral de ces documents, les disséquer pour les indexer, s'en servir de données pour un logiciel, ou s'en servir à toute autre fin légale (ou prévue par la réglementation relative au droit d'auteur). Toute utilisation du document à des fins commerciales est strictement interdite.

Par ailleurs, l'utilisateur s'engage à respecter les droits moraux de l'auteur, principalement le droit à l'intégrité de l'oeuvre et le droit de paternité et ce dans toute utilisation que l'utilisateur entreprend. Ainsi, à titre d'exemple, lorsqu'il reproduira un document par extrait ou dans son intégralité, l'utilisateur citera de manière complète les sources telles que mentionnées ci-dessus. Toute utilisation non explicitement autorisée ci-avant (telle que par exemple, la modification du document ou son résumé) nécessite l'autorisation préalable et expresse des auteurs ou de leurs ayants droit.

Flutter Wizard: Development of an automatic tool for safety prediction in compressors and turbines

Master's Thesis

Author: Carlos Alberto Tavera Guerrero
Industrial Supervisor: François Debrabandere
Academic Supervisor: Vincent Terrapon
Company: NUMECA International

Graduation Studies conducted for obtaining the Master's degree in
Civil engineer in aerospace, specialized in "turbomachinery aeromechanics"
by Carlos Alberto Tavera Guerrero

University of Liège
Faculty of Applied Sciences
Academic year 2018 - 2019

Contents

List of Figures

List of Tables

List of Symbols

Variables

$\ddot{q}_i$	Generalized acceleration from mode i
$\ddot{x}$	System acceleration vector
$\dot{q}_i$	Generalized velocity from mode i
$\dot{x}$	System velocity vector
$\mathbf{C}$	Damping matrix
$\mathbf{K}$	Sitffness matrix
$\mathbf{M}$	Mass matrix
A_i	Area at location i
c	Chord
c_n	Normalized true chord
c_p	Specific heat at constant pressure
f	Osiclation frequency
H	Blade span
h_0	Total enthalpy
i	Imaginary number
k	Reduced frequency
KE_{avg}	Average kinetic energy
L_{ref}	Reference length
M	Absolute Mach number
M_{iso}	Isoentropic Mach number
N	Blades number
P	Static pressure

P_{imag}	Imaginary harmonic static pressure
P_{real}	Real harmonic static pressure
P_{ref}	Reference pressure
P_t	Total pressure
q_i	Generalized displacement from mode i
T	Period
t	Time
U	Conservation vector
u	Physical displacement
u_{max}	Imposed physical displacement
U_{ref}	Reference velocity
W_{aero}	Aerodynamic work
x	System displacement vector
y^+	Non dimensional first wall height
y_{wall}	Frist cell wall distance

Greek letters

π	Pressure ratio
Θ	Radial angle
α	Absolute flow angle
β	Relative flow angle
δ	Bending direction angle
γ	Stagger angle
λ	Wave length
ν	Kinematic viscosity
Ω	Rotational speed
ω	Oscilation frequency
ϕ_i	Phase angle at location i
ψ	Modeshape

ρ	Flow density
σ	Interblde Phase Angle
τ	Pitch
$\vec{\tau}$	Shear stress
Ξ	Normalized aerodynamic damping coefficient
ζ	Modal damping

Special notation

$\bar{U}$	Conservation vector mean time
$\tilde{c}_{p_i}$	Unsteady pressure coefficient at location i
$\vec{f}_{aero}$	Aerodynamic force
U'	Conservation vector perturbation

Acronyms

B2B	Blade to blade
BTW	Backward Traveling Wave
CAD	Computer Aided Design
CFD	Computational Fluid Dynamics
EASA	European Aviation Safety Agency
EO	Engine Order
FAA	Federal Aviation Administration
FSI	Fluid-Structure Interaction
FTW	Forward Traveling Wave
GUI	Graphical User Interface
HCF	High Cycle Fatigue
HPC	High Pessure Compressor
HPT	High Pressure Trubine
IBPA	Interblade Phase Angle
LCO	Limit Cycle Oscilation
LE	Leading edge

LPC	Low Pressure Compressor
LPT	Low Pressure Trubine
ND	Nodal Diameter
NLH	Non-Linear Harmoncic
OEM	Original Equipment Manufacturers
PS	Pressure Side
RANS	Reynolds Averaged Navier-Stokes
SS	Suction Side
STCF	Standard Configuration
TE	Trailing edge
VIV	Vortex-Induced-Vibration
ZZENF	Zig Zag shaped Excitation line in the Nodal Diameter versus Frequency

Acknowledgements

A mi familia, por su orientación y apoyo incondicional en cada momento de mi vida.
To my new adopted family from the THRUST program.
A Babe Batman, porciempre.

Abstract

One aeroelastic phenomenon that has to be avoided at all costs in turbomachinery is flutter. Flutter is a self-sustained and self-excited excitation that jeopardizes the structural life in a matter of seconds. This phenomenon is highly dependent on multiple parameters that makes it unable to be predicted a priori. A key factor is the variation of the inter blade phase angle that must be assessed at each operational condition to guarantee the machine integrity. This process generates an enormous amount of computational flutter analysis that is performed manually increasing the engineering time, and it is dependent on the user's expertise. Generating a need of reproducing reliable results without any user interaction resulting in an engineering time reduction.

This need was satisfied by the development of a flutter wizard tool, which works within FINE™/Turbo. The tool is able to set up and analyze a single or multiple rows for one vibrating blade, at one or multiple operational conditions with or without custom user inputs. By making use of the developed flutter wizard tool the engineering time required was strongly reduced, it only took approximately 1.5% of the time when compared to a manual set up and analysis. The wizard also provides a flexible and user-friendly set up so the client can reproduce complex or particular cases if desired.

Seven cases were analyzed with a variety of geometry, operational conditions and imposed motion. Six cases were contrasted against experimental and numerical data, while the seventh just against numerical data from two software. A close match between steady state experimental and current results was found in all cases, except where non-linear effects were encountered. A total of 153 non-linear harmonic cases were run with the wizard, in which for an operational condition it provided a direct output of the aeroelastic stability of the system by means of the aerodynamic damping coefficient. A proportional aerodynamic damping coefficient curve per reference was used, as it proved to remove the scaling factor and retrieve the proportional aerodynamic work for each case with a better agreement among results. A manual detailed analysis of the harmonic content at specific blade height locations were performed to validate results. Thus, a collection of results is gathered and analyzed in detailed, providing a description and correlation of the steady and unsteady results. Finally, future work is proposed as a benchmark on a last stage steam turbine, as the actual machine and stator/rotor interaction is taken into account.

Chapter 1

Objectives

1. To develop a tool that allows the user to retrieve effortless, a full flutter stability analysis by means of aerodynamic damping coefficient within FINE™/Turbo software which is developed at NUMECA International in order to reduce the engineering time.

2. To implement a robust flutter set up to guarantee a reliable result, by means of the Non-Linear Harmonic method by prescribing a convenient amplitude of vibration, for a single or multiple operational points of a single or multiple rows, with the flexibility to provide a custom setup by the user.

3. To utilize the flutter wizard tool to validate the solver results against open source literature cases which contain reliable experimental and numerical data.

4. To investigate the aeroelastic effect of a stator-rotor interaction on a 3D steam turbine geometry, by comparing results from a commercial software and a reference in-house university code by making use of the flutter wizard tool

5. To correlate the flow physics of the steady state, harmonic content of unsteady solutions with its aerodynamic stability coefficient.

Chapter 2

Introduction

Aeroelasticity is a branch of engineering that relates the aerodynamic and dynamic forces acting on an elastic structure. A critical phenomena that might be encounter in an aeroelastic system is flutter. Flutter is defined as a self-excited and self-sustained instability that increased the vibration amplitude of the structure at every cycle exponentially, which can jeopardize the safety of the system in matter of seconds. Flutter in turbomachinery has been evaluated for around sixty years and it is still nowadays a field of research as currently there is no method that predicts in advance if it would be encounter due to its complexity. A key assumption within an aeroelastic system in turbomachinery, is that all blades have the same structural properties, leading to the same vibration frequency and same amplitude, with just a difference in phase from one blade to another which is known as an interface blade angle (IBPA). The current assessment method to determine flutter in a turbomachine is to determine the work done by the unsteady aerodynamic force over the moving structure, which is related to the aerodynamic damping of the system. A negative work is stable as the aerodynamic force removes energy from the system whereas a positive feeds energy, becoming unstable. The aerodynamic damping of the system can be affected by the steady flow field structure, mode shape, vibration frequency, and IBPA among others. Thus, as it is not known a priori at which condition flutter will be encounter, therefore all possible IBPAs from all operational conditions must be evaluated. Therefore, the amount of assessments required increases rapidly on a ratio of the number of available IBPAs times the number of evaluated conditions. For instance a twenty bladed turbine which is assess at six operational conditions would have hundred twenty flutter analysis to be determined. Currently, there is no tool available in any CFD software that can perform an automatic flutter set up without any user interaction and which can evaluate all possible IBPAs from multiple operational conditions automatically. This provided a window of opportunity to develop such tool.

Thus, a flutter wizard tool was developed in Python 2.7 to be implemented within FINE™/Turbo. The tool makes use of the available Fluid Structure Interaction of the Non-Linear Harmonic method by prescribing the modeshape, natural frequency and generalized displacement. The generalized displacement of the imposed mode is automatically calculated as a function of the imposed physical displacement, 0.5% of the blade chord tip, and its maximum modal amplitude. For each IBPA the aerodynamic power is retrieved and it is post processed to recover the aerodynamic damping coefficient, by Fransson scaling method, for each operational condition. The wizard was developed with two possible cases to be run, A and B. The former allows the user to start the flutter analysis starting from a steady state computation, whereas the latter from a reference unsteady case. This configuration satisfies a key objective to provide a user friendly tool that is able to provide the full flutter stability curve for a single or multiple row configuration, for one or multiple operational conditions. Additionally, at each case the wizard gives default conditions but the user is able to impose the desired mode, physical displacement, real and imaginary magnitudes of the

generalized displacement, computation type, among others. For each operational condition the wizard creates an **_Aerodamping_stability.dat* file which contains all magnitudes required to retrieve the aerodynamic damping coefficient, the calculated aerodynamic damping coefficient, the IBPAs, and aerodynamic power, in case the user desired a different aerodynamic damping scaling. Additionally, the aerodynamic damping coefficient curve is provided in **_Aerodamping_stability_curve.png* format for quick overview of the system stability. Furthermore, if multiple operational conditions are selected, the wizard creates a performance curve of the selected computations and for each of them assigns the flag "Flutter free" or "Non Flutter free" condition recovered from the full analysis. This performance curve stability map provides in a simple manner the entire flutter stability of the machine. Another key point achieved is that the wizard will enable the user to obtain reliable flutter results without a full background in aeroelasticity.

The tool was used for seven operational conditions which were compared against reliable numerical and experimental data from two standard configuration cases and a last stage steam turbine, which takes into account the stator/rotor interaction. A strong reduction in engineering time was produced, as the entire set up for each case took between 45 seconds to 1:20 minutes, which is approximately 1.5% of the engineering time without making use of the wizard. In all cases the flutter wizard is used to obtain automatically the aerodynamic damping coefficient curve. For each case a manual detailed analysis of the harmonic content of the results was performed. The assessment was performed at 50% of the blade height, at a reference IBPA of 180° and its corresponding least and most stable IBPA. The aerodynamic damping coefficient, phase and harmonic amplitude were compared with experimental data and numerical data depending on its availability for each case. For each case a description and interpretation of the results with the flow physics is done in an effort to correlate steady and unsteady results as it is rarely encounter in flutter analysis within turbomachinery literature. Therefore, this thesis provides a collection of reliable cases that are compared with a NLH method, which is up to now known as the only available commercially. Finally, this thesis propose the analysis of last state steam turbine without any modification on the machine properties and taking into account the stator/rotor interface as a benchmark within the aeroelastic in turbomachinery community.

Chapter 3

Theoretical background

In the early 1940's there was a quick development of aircraft, which required higher speeds and structural loads. Within them, it rose a new type of problems which link the interaction of the flow and an elastic dynamic structure, known as aeroelasticity. However, this phenomena is not only exclusive of engineering but in nature can be found as well. The interaction of a long tree branch vibrating as the air stream passes through and the feedback of the vibration into the flow surrounding it, or the sudden and strong oscillatory movement of a leaf due to the airflow passing through are good conceptual examples.

Perhaps, one of the most famous cases of aeroelasticity phenomena is the Tacoma bridge in 1940. In which the interaction of the wind over a blunt body ended up in a beautiful but catastrophic self-excited bridge oscillation as shown by Billah and Scanlan [1]. Multiple historical examples of aeroelastic failures are shown by Garrick and Reed [2] and Bendiksen et al. [3]. Nowadays, aeroelastic phenomena is still a point of interest when developing structures such as: bridges, skyscrapers, aircrafts, aero engines, wind turbines, among others. On a general trend, the structures tend to be slender and lighter with higher loading conditions, leading them to be more prone to aeroelastic problems.

Aeroelasiticity can be properly defined as a branch of engineering that joins the interaction of fluid mechanics, solid mechanics and dynamics. Each of these fields is an entire subject that have been studied for more than 200 years. It was until 1946 that Collar [4] merged these three main subjects, as shown in Figure 3.1. The correlation between two vertexes is a complete branch of expertise as well. Furthermore, Collar diagram can be extended into a tetrahedron by including thermal effects and even some authors extend aeroelasticity by taking into account the servo systems [5]. However, the inclusion of thermal loads and servo excitation is not the scope of this thesis. From Collar's diagram, it is clear that aeroelasticity can be divided in two branches: static (e.g. Divergence) and dynamic (e.g. Flutter). Thus, only flutter and buffeting are the fields within the triangle that corresponds to dynamic aeroelastic phenomena within this figure. However, these are not the only phenomena, as Vortex-Induced-Vibration (VIV) and forced response would be also inside the triangle. In other words, aeroelasticity focuses on the study of the aerodynamic and structural dynamic forces acting on an structure.

Figure 3.1, shows that there is a wide palette of engineering applications that are prone to fluid-structure interaction (FSI) which will lie within the triangle, leading to a critical influence on the safety of the design. During the design of any element that would encounter FSI the target is to guarantee that the element will hold at operational conditions and also at expected off-design conditions.

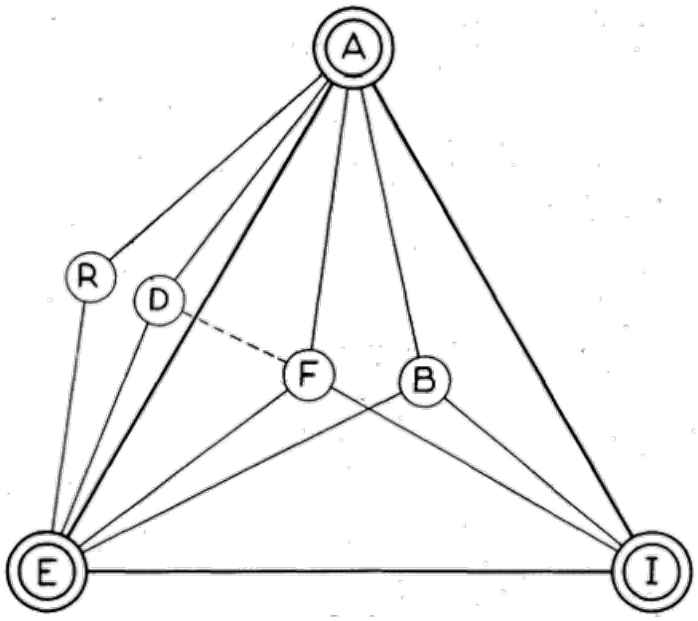

Figure 3.1: Collar triangle: A = Aerodynamic forces, E = Elastic Forces, I= Inertia forces, F= Flutter, B= Buffeting, D = Divergence, R = Reversal control, Collar [4] .

The consequences of this type of phenomena in the vibration response can be classified mainly in two families: non-synchronous and synchronous. The former can lead to a self-excited excitation that triggers an instability condition in which the vibration amplitude will increase until there is a majestic failure or stops by self-limiting, such as flutter and VIV. The latter known as forced response, which is a function of the rotational speed and the amount of nearby structures downstream and upstream. It will produce a specific increase in the amplitude but will not produce an unstable condition as it is not self-excited. However, if the amplitude of vibration is higher than the designed conditions it becomes critical as High-Cycle Fatigue (HCF) failure or contact between one element and its surroundings can occur.

Flutter is a self-excited and self-sustained instability, that leads to an increase of vibration amplitude leading to a quick structural failure due to fatigue or leads to Limit Cycle Oscillation (LCO) in case of structural non-linearities. Flutter is a critical phenomena because it compromises the structural life of the element due to HCF failure and it develops as fast as in one second, as shown by Holzinger et al. [6]. In other words, it has a direct impact in maintenance and reparation costs. An example of it, is the F100 engines for the fighter F-15 which lasted only 100 safe cycles before a blade break which led to economical costs, despite no aeroelastic issues were reported during its testing [7] [8]. For instance, Kielb [8] predicted billions of USD spent due to HCF encountered problems until 2020. Srinivasan [9] highlighted that the expenses of stopping a 500 MW power plant are of the order of millions USD per week. And still in 2000 this was a global problem as almost 50% of the air fighters had HCF issues [10]. The worst case scenario is to compromise the structural integrity of an entire airplane that ends up in deathly losses as 30 years ago with the flight of Boeing midland-737 in Leicestershire [11].

Flutter phenomena can be understand conceptually from the general equation of motion from a structural dynamics system, shown in Eq. 3.1. Where $\mathbf{M}$, $\mathbf{C}$, $\mathbf{K}$, and $\vec{f}_{aero}$ the mass, damping and stiffness matrices, and aerodynamic force respectively. The aerodynamic force when it is linearized it is expanded into two terms, one related to the displacement x of the system and another to the velocity $\dot{x}$. So, one term of the aerodynamic forces contributes to the stiffness of the system and another contributes to the

damping. This last term is known as aerodynamic damping.

$$\mathbf{M}\ddot{x} + \mathbf{C}\dot{x} + \mathbf{K}x = \vec{f}_{aero} \tag{3.1}$$

External aeroelasticy has been widely studied and the scope of this thesis focuses on aeroelastic phenomena in turbomachinery. On them, vibration issues have been identified for more than 100 years [8]. As multiple excitation sources occur within a turbomachinery it is not possible to separate the excitation frequencies from its natural frequencies, hence the idea of adding damping is a common approach to solve the vibration issues. However, Srinvasan [12] proved that the mechanical damping of an aeroengine blade is very small, and the main damping comes from the aerodynamic one. Thus, the total damping of the system is the addition of structural and aerodynamic, but as the structural is very low normally it is assumed that the aerodynamic damping is almost equal as the total damping unless frictional damping is added.

The main characteristic from the aerodynamic damping is that it has the drawback that it can become very small until actually turns negative. Meaning that the flow field will be feeding energy into the system and thus the rapid failure of structures. This phenomena can also be understand from the perspective of a force in phase or out of phase with respect to the structure motion. The force coming from the unsteady aerodynamics over the blade is normally transformed into a complex plane. The angle between the real and imaginary axis is the phase. Thus, if the phase is positive the unsteady force is actually leading the motion of the blade, in other words causing instability whereas if the phase is negative now the motion is leading the force, or the force has a lag. This concept is highly important because if the unsteady force due to the airflow leads the motion will cause flutter. In centrifugal turbomachines, Kammerer and Abhari [13] proved that the aerodynamic damping is 10 times higher than the structural damping. However, it is from the author's knowledge that no negative damping cases have been reported in literature on centrifugal machines.

In turbomachinery another important type of common aeroelastic phenomena is forced response. The physical insight is that there is an external force coming from an excitation source that matches a natural frequency of the system. For instance, the wakes of the upstream and downstream blades, burner cans, etc. In these cases, the blade is feeling the external excitation as an integer of the rotational speed, known as Engine Order (EO). By the diagram created by Campbell [14] shown in Figure 3.2, it is easy to correlate the natural frequency of the structure as a function of the rotational speed versus the excitation frequencies. On this diagram, all the intersections are resonant points. These, represent a possible risk as this will lead the highest amplitude response from a frequency response function that might cause an undesired vibration amplitude. The natural frequencies of the structure will vary as a function of the rotational speed as the centrifugal forces produces normally a stiffening effect.

From the Figure 3.2, the regions in which forced response will occur are highlighted with a circle and those of flutter with an asterisks. The above diagram is extremely useful when analyzing forced response, but not as much when analyzing flutter. The only flutter information available is that flutter occurs close to the natural frequency of one mode. However, it is not known at which mode will occur, nor close to which EO. This is the root cause of why flutter is highly complicated to predict, because no clear information that can lead to its identification is known a priori.

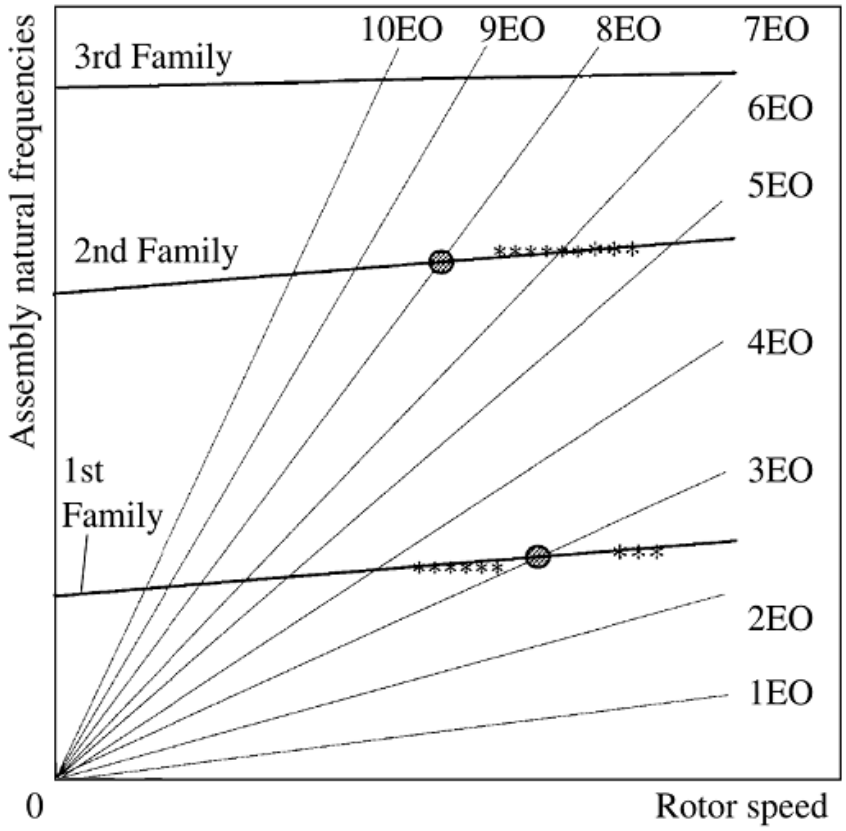

Figure 3.2: Campbell diagram example with flutter and forced response regions, Marshall and Imregun [15]

Inherently a turbomachine works on the basis that it is required a local change of total enthalpy from the fluid which is obtained by a fluctuation in pressure [8]. Therefore, the turbomachines are inherently an unsteady system. The aerodynamic forces, shown on the right hand side from Equation 3.1 can be highly complex. A brief introduction to those flow structures and the physical insight of them are display in Figure 3.3 in which the flow structures of a compressor rotor and turbine rotor are displayed. It is clear that the flow is highly dominant by 3D effects and viscous effects near the hub and shroud. Tip leakage vortices, separation, passage vortex, wakes, rotating reference frame, mixing of secondary flow regions, shocks and a mixing plane between stator-rotor interface are flow structures within a turbomachine. This is a clear argument that the solutions of the flow field should be in 3D and not on a 2D plane for complex operational conditions.

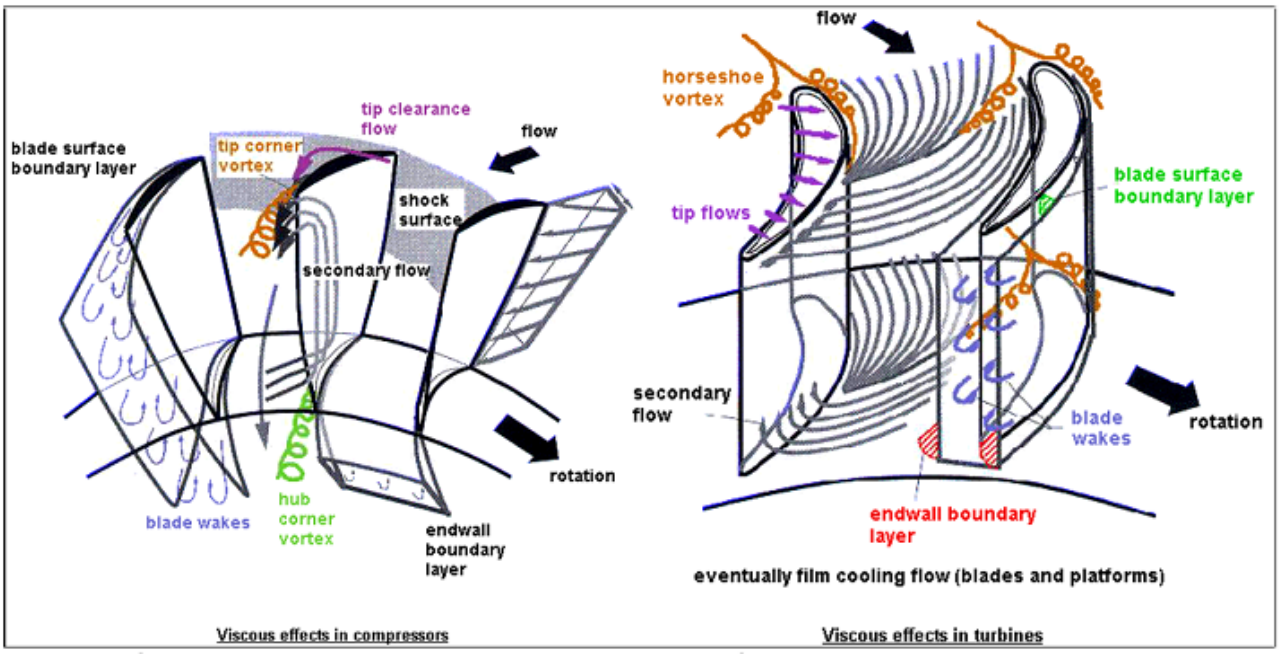

Figure 3.3: Flow field in turbomachinery: compressor and turbine, Fransson [8]

Great efforts have been done in order to have a better understanding of the factors that affect flutter. A contrast of a pictorial conceptual understanding sketch in AGARD manual (Figure 3.4) to an Ishikawa diagram from Montogomery et al. [16] (Figure 3.5) shows a more mature understanding gained in the last sixty years. Figure 3.5 provides a quick overview of all the possibilities of the root cause of this phenomena, which basically is the extension in words of the general equation of motion (Eq. 3.1).

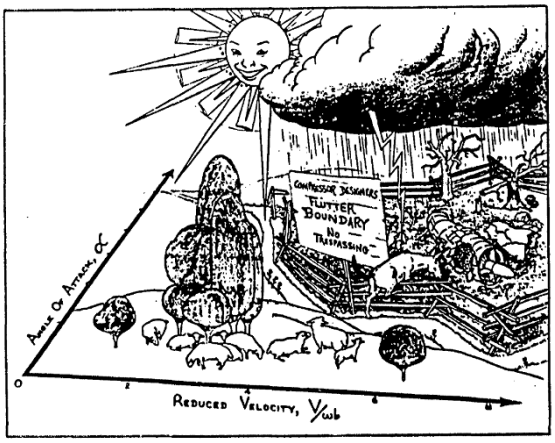

Figure 3.4: Pictorial sketch of flutter, Sisto [17]

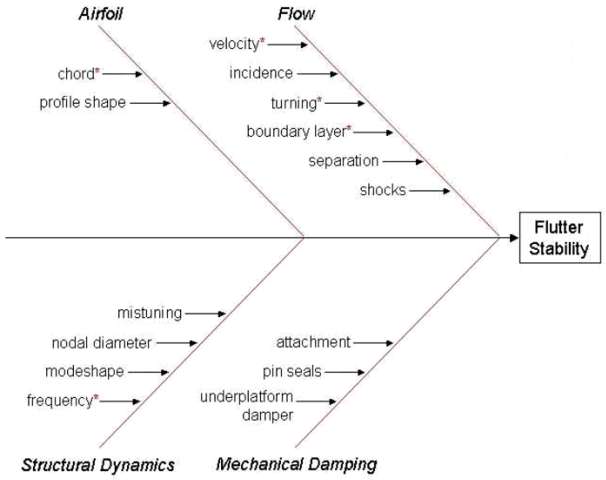

Figure 3.5: Flutter sensitivity parameters, Montgomery et al. [16]

Among these factors, it has been found by several authors [18] to [25] that the parameters that have the highest influence are: Mode shapes, nodal diameter, inter-blade phase angle (IBPA), reduced frequency, shock position and steady sate conditions. Therefore, there is a wide range of variables to take into consideration as any of these parameters might onset or avoid flutter.

3.1 Structural dynamics in turbomachinery

The structural dynamics of a turbomachine can be classified in two main branches: blade modes and disk modes. The former, can be decomposed mainly in three fundamental modes: Bending/Flex/Flap (B), Edgewise (E) and Torsion (T). B mode is perpendicular to the chord, E mode is parallel to the rotational axis and T mode produces a rotation along the radial direction. These modes are based on the assumption that the blade is perfectly fixed to the base and the disk is highly stiff that it does not have an influence on the modes. This leads to modes similar to the ones found on a cantilever flat plate. Figure 3.6 shows a modal analysis representation of the blade modes. As the only boundary condition is on the hub, further modes will appear as a combination of these three with the characteristic of having nodal lines, which will affect the unsteady pressure field. The nodal lines are the locations along the blade in which there will be no modal displacement.

The latter branch is the disk modes. This also can be separated into three fundamental modes: Axial (A), Radial (R) and Tangential (T). Axial is the most common encountered mode as shown in Figure 3.7, it produces a combination of positive and negative displacement in the axial direction and the locations where there is no displacement are known as Nodal Diameters (ND). This type of mode has the main property that produces a wave movement of the blades on the disk known as *traveling wave*. This traveling wave can be either forward (FTW) or backward (BTW) with respect to the rotation of the machine, and depends on the amount of nodal diameters which is a function of the number of blades (N) depending if its even or odd number of blades as shown by Equations 3.2 & 3.3) respectively:

$$ND = \pm\frac{N}{2} \tag{3.2}$$

$$ND = \pm\frac{(N-1)}{2} \tag{3.3}$$

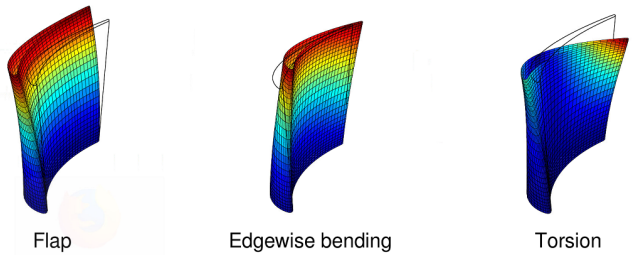

Figure 3.6: Basic blade modeshapes, Vogt [10].

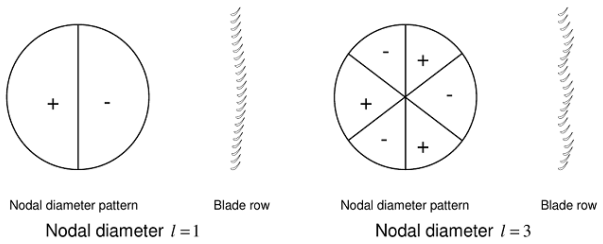

Figure 3.7: Disk nodal diameters, Vogt [10].

Lane [26] found that the blades vibrate at the same amplitude but with a vibration phase between one another as a function of the nodal diameters. This phase is known as the inter blade phase angle (IBPA), denoted by the Greek letter σ, which is valid for a tuned system. A tuned system is defined as a configuration in which all the blades have the same structural characteristics. This conditions is never achieved in practice due to manufacture variations. Nevertheless, this assumption is valid as long as no intentional mistuning is added. The IBPA is defined as a function of the nodal diameters and the number of blades as shown in Eq. 3.4.

$$\sigma = \frac{2\pi ND}{N} \tag{3.4}$$

Flutter in turbomachinery is a single mode phenomena compared to external flutter that is a two mode coupling. In turbomachinery the coupling from one blade to another is done by the fluid inside the passage with the IBPA as the phase from blade to blade as a function of the ND and normally this is assumed to be a constant value. However, Marshal and Imregun [15] highlighted that the modeshape is in fact part of the solution of a flutter analysis. As coupling of structural modes and transonic flow has been encountered in experimental data leading to no longer a constant value of IBPA. The most common way to approach this non-linear effects is to keep assuming a constant IBPA for all possible nodal diameters and have the least stable as the reference.

In reality a turbomachine is a structure that is either blade dominated or disk dominated as a function of the nodal diameters. If the blades are large compared to the outer diameter of the disk, and the disk is highly stiff the behavior of the structure will be blade dominated, as in a Low-Pressure Compressor (LPC), Low-Pressure Turbine (LPT) or a Fan. On the other hand, if the disk is softer and the blades are small as encounter in the High-Pressure Turbine (HPT), High-Pressure Compressor (HPC) the structure will be disk dominated. The effect of this can be found in the Figure 3.8. The *veering* region is where the interaction of blade and disk modes are higher. In this figure the red plot shows the bladed dominant modes, whereas the blue displays a disk dominant modes.

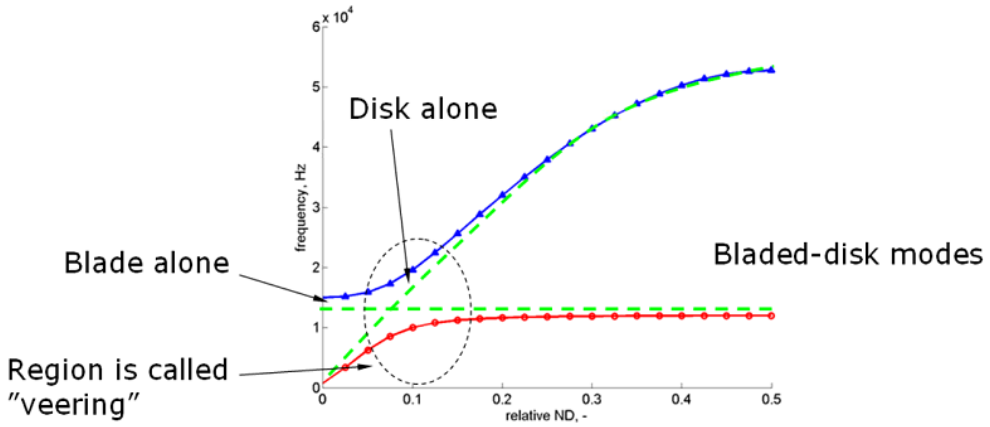

Figure 3.8: Bladed disk family modes, Vogt [27].

This diagram has two main benefits. The first, highlights that for bladed-dominant modes, the low modes are the disk dominated but it switches to blade dominance as the number of nodal diameters is increased. The second, it can be used to create a ZZENF (Zig Zag shaped Excitation line in the Nodal diameter versus Frequency) diagram, Figure 3.9. This diagram, correlates the natural frequency, the blade-disk family mode and the excitation frequency. This is useful to have a specific reference for a forced response problem but of less impact for a flutter analysis, as no mode, nodal diameter nor operational conditions are known in which flutter can occur.

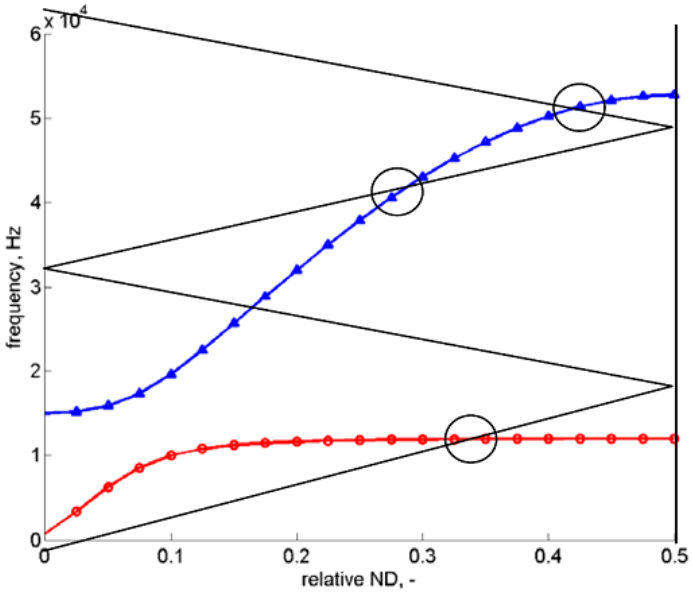

Figure 3.9: ZZNEF diagram, Vogt [27].

3.2 Reduced Frequency

Another parameter that has found to be critical is the reduced frequency (k) introduced by Meldahl [28]. The general trend is that for a given configuration, if k is reduced the system has a tendency of instability. The reduced frequency is defined as equation 3.5. Here it is clear that there are two ways to approach the physical understanding of it. The first, as the time (t) of the fluid flowing through the chord per period of oscillation (T). Assuming a constant chord, if the velocity is the dominant term this would imply that the flow field is crossing very fast leading to a quasi-steady condition. Another approach can be seen from the second definition provided by Srinivasan [9] in which relates the chord (c) and the wave length (λ). If λ increases is clear that k would tend to a small value, meaning that the flow has a quasi-steady condition. On the other hand, if the wave length is small means that there is a high perturbation leading to high values of k and the flow is highly unsteady.

$$k = \frac{2\pi f c}{U_{ref}} = \frac{t}{T} = \frac{c}{\lambda} \tag{3.5}$$

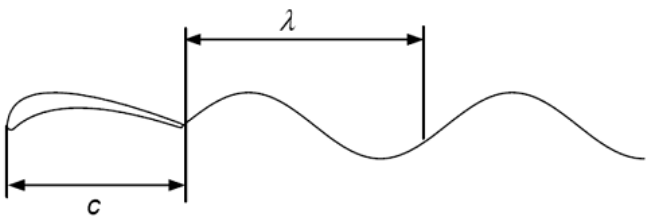

Figure 3.10: Reduced frequency interpretation, Vogt [29].

Thus k can be seen as a measured of the unsteadiness in the flow field, the ranges in which flutter has been documented to occur at low reduced k, for instance Srinivasan [9] provides a reference from 0.4-0.7

from multiple experiments. Nevertheless, this values ranges are found to be case dependent, from 0.1 to 1 as shown by Vogt [10] and used as reference rather than guidelines, Zhai et al. [20] and Holzinger et al. [6].

3.3 Flutter regions

Flutter is prone to occur in slender and light structures, such as fans, LPC and LPT. When analyzing a compressor map in the available literature, it is clear that there are multiple flutter regions and each of them would produce different physical phenomena within the passage as shown in Figure 3.11.

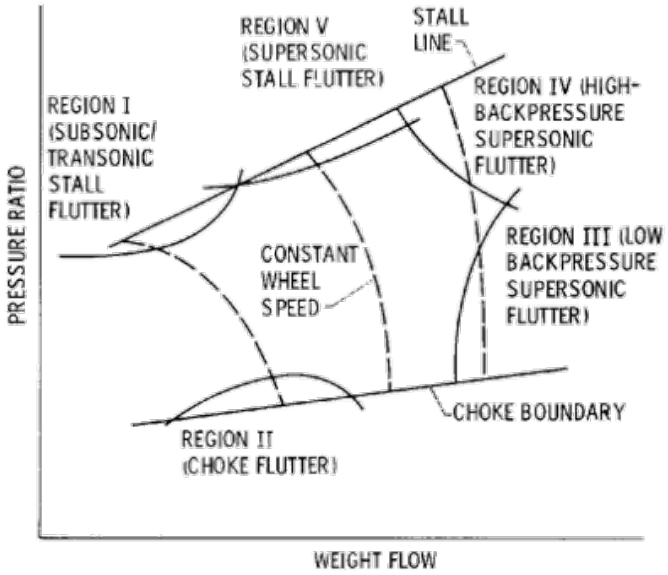

Figure 3.11: Compressor map flutter regions, Lubomski [30].

Lubomski [30] and Adamczyk et al. [31] provides a description of five main flutter regions, shown in Fig. 3.11 based on experiments on turbofan and turbojet engines (1-5). Bendiksen et al. [3] also describes flutter regions in compressors but with less physical insight. However, includes a brief description of LPT flutter (6) and complements the supersonic flutter. Thus, the types of flutter are summarized as follows:

1. Subsonic/transonic stall flutter: Characterized by a high incidence angle that produces separation of the flow at either the suction or pressure sides. The location of the detachment point is of high importance to determine the system stability. The harmonic frequency of the separated flow has found to be similar, but not exactly, to the imposed blade vibration. This type of instability may or may not occur at the boundary of the stall line. These flow field characteristics, allows this condition to be predicted before it might occur.

2. Choke flutter: Characterized by a small incidence angle with the flow fully attached to the blade, but partial or full choke regions within the blade passage. Flutter frequency is close to the vibration frequency but it is affected by the inlet boundary conditions, and it is not possible to be anticipated.

3. Low-back pressure supersonic flutter: Characterized by occurring at the maximum rotational speed, which occurs from a region close to the operational working line to the choke line. At this region the stability is highly dependent on the reduced frequency.

4. High-back pressure flutter: Characterized by occurring on the the same working speed as low-back pressure but as there is a high back pressure the flow physics changes to a region close to the stall line. At this condition if the reduced frequency is decreased a first bending flutter mode might be onset.

5. Supersonic stall flutter: Also known as system mode instabilities, is characterized by a full attached flow around the blade, but with a variation of flutter onset physics due to the structural or aerodynamic properties. Can include, or not, mode coupling (bending and torsion) as a function of the type of blade (shrouded or not shrouded). One characteristic is that the frequency and the amplitude might be not longer independent but linked, which it might be due to structural non-linearities due to the high loads and mistuning

6. LPT flutter: The best known and possible to analyze as a 2D cases in preliminary designs as it occurs on a positive pressure gradient with low viscous effects, leading to no surge effect.

3.4 Aeroelastic solutions

The aerodynamic forces for a flutter analysis can be obtained by multiple methods as shown by Marshall and Imregun [15]. The most common is by solving a Reynolds-Averaged Navier-Stokes (RANS), in which the variables are replaced by its time-averaged which require the usage of a turbulence model to close the system. This method is used as it is accurate for aeroelastic systems, and is based on a Finite Volume Method (FVM). The aeroelastic methods to analyze a FSI problem can be separated in two main branches: classical and integrated methods.

1. Classical: This type is characterized because the modal properties of the structure are obtained on a free-vibration analysis and the aerodynamic forces do not affect them. This is also known as a one-way coupling. It provides reliable solution as long as the assumption of small displacements is valid. The most common method is the energetic one, which is based on the work done on the blade by the unsteady forces over one cycle. If the work has a negative sign it means that the blade is reducing its energy (stable), but if the work is positive means that the system is actually gaining energy (unstable).

2. Integrated: This type of coupling is based on the fact that the fluid produces an effect on the structure and vice-versa. At each time step there is an exchange of information by the interaction from one to another. This is known as two-way coupling. The main advantage is that is able to take into account non-linear responses such as LCO and friction. And this type is subdivided in two categories: partially and fully integrated. The former, provides more flexibility as it communicates two different solvers, with the drawback of a lag between one another. The latter uses one unique solver with no lag. As the scope of this thesis is not based on the integrated methods, if the reader is interested it is suggested to refer to [32], [33], [34], [35] for further details.

The amount of flutter analysis increases rapidly for instance, for a new aircraft designs because currently there is no method to fully predict flutter [36]. The aircraft must comply with the FAA and EASA regulations to prove that the aircraft is flutter free over the flight envelope with a damping margin [37], [38]. The need to be able to predict a priori experimental tests that the aircraft will not suffer flutter is of high importance to minimize the experimental costs and to have a high fidelity product. This situation applies as well in turbomachinery, in which it is not known a priori in which mode, nodal diameter or at which operational condition flutter might occur, producing an enormous amount of conditions to assess.

Therefore, improvements in CFD solution methodologies, meshing techniques and robust designs are a main target to achieve to enhance the design process.

One of the targets is to obtain reliable results in a relative small amount of time. Thus research on CFD and comparison with experimental results has been carried out for the last 30 years [39]. In general the flow field solution can be analyzed in time domain [40], [39], frequency domain [41], [42], [43], [44] and a hybrid time-frequency harmonic [45].

3.5 Harmonic methods

The solutions in time domain, can be done either by a non-linear approach or a linearized-time methodology. One great advantage is that all the CFD algorithms can be implemented to guarantee robustness and efficiency, and additionally is not restricted to one excitation frequency. Nevertheless, the main drawback is that the computational time is still not feasible as the time steps need to be very small to have stability and in many cases the full annulus system needs to be evaluated.

On the other hand, in frequency domain a spatial and time periodicity is used to simplify the control volume of a turbomachine by applying periodic boundary conditions, leading to the need of just several passages or just one passage but not the full machine. Additionally, the time derivatives are replaced by complex frequency terms, leading no time variable within the conservation equations. There are four main types of methodologies to solve the flow equations in the frequency domain, those are: Linear harmonic, Non-linear harmonic (NLH) Ning and He [41] Vilmin et al [43], Harmonic balance Hall et al. [42] and Phase-shift method by Rahmati [44]. From these, the key advantage of NLH among other methods is that all the equations are solved on the frequency domains, in contrast with the Harmonic Balance that goes back to the time-domain by an inverse Fourier transformation. Thus, this method provides a good accuracy and faster convergence when compared to time-domain methods. This method is available in FINE™/Turbo, and allows a one and two way coupling fluid-structure interaction [46].

3.6 Non-linear harmonics

NLH is an extension of the linear harmonic. In this method it is assumed that the conservation vector, $U(\rho, \rho\vec{v}, \rho e)$, can be decomposed in a non-dependent time term and a sum of periodic perturbations. On linear harmonics the non-dependent time term refers to the steady state value, whereas on NLH it refers to the time-averaged which includes the unsteadiness. The perturbation then is assumed to be a Fourier Series, in which the base frequency corresponds to the perturbation frequency (natural frequency) [43] [47].

$$U(\vec{x}, t) = \bar{U}(\vec{x}) + \sum_{n=1}^{N_{pert}} U'_n(\vec{x}, t) \tag{3.6}$$

$$U'(\vec{x}, t) = \sum_{k=1}^{N_{harm}} \left(\tilde{U}_k e^{i\omega k t} + \tilde{U}_{-k} e^{-i\omega k t} \right) \tag{3.7}$$

Furthermore, the addition of the time-averaged terms in NLH leads to non-linearities and produces the so called "deterministic stresses" which are similar to the Reynolds stress terms. The system is solved in the frequency domain and the unsteady problem is turned into two steady problems one for the time-averaged and another for the perturbation. This leads to more equations to solve but as they are steady, the CPU costs is cheaper than an unsteady. Also, this method would just require one passage to be meshed, which reduces significantly the computational resources. This method solves five conservation equations plus one of turbulence model for the mean part. For the perturbation part, it solves 5 complex equations and 5 corresponding to its complex conjugate, per harmonic. The total amount of equations is proportional to $6 + 10k$ where k is the total number of harmonics for one the perturbations.

Equation 3.8 is a simplification from the general equation of motion, Eq. 3.1. It consists only on a free vibration problem without damping nor force. It is shown by Equation 3.13 that the only non trivial solution solution is when the determinant is zero, meaning that the liner transformation is reducing one dimension the space. Thus the only vectors that will lie on this space reduction are in fact eigenvectors.

$$\mathbf{M}\ddot{x} + \mathbf{K}x = \vec{0} \tag{3.8}$$

$$\vec{u}^T M\vec{u}\ddot{f}(t) + \vec{u}^T K\vec{u}f(t) = \vec{0} \tag{3.9}$$

$$\ddot{f}(t) + \frac{\vec{u}^T K\vec{u}}{\vec{u}^T M\vec{u}}f(t) = \vec{0} \tag{3.10}$$

$$\ddot{f}(t) = -\lambda f(t) \tag{3.11}$$

$$-\lambda M\vec{u}f(t) + K\vec{u}f(t) = \vec{0} \tag{3.12}$$

$$det|(K - \lambda M)|\vec{u}(t) = \vec{0} \tag{3.13}$$

Thus, a transformation from the physical displacement by its modal form is done by Equation 3.14. It links the physical displacement with its corresponding modal generalized displacement. By making use of the orthogonal properties of the eigenvectors and enforcing that the modal mass to 1, the system is decoupled into multiple single degree of freedom. This process is known as orthonormalizing and Equation 3.15 shows a single degree of freedom modal equation for an i mode, including a Raygleigh damping.

$$\vec{x}(t) = \psi\vec{q}(t) = \sum_{m=1}^{N_{modes}} q_m\vec{\psi}_m \tag{3.14}$$

$$\ddot{q}_i + 2\zeta_i\omega_i\dot{q}_i + \omega_i^2 q = \psi_i^T\vec{f}_{aero} \tag{3.15}$$

Additionally, the same logic from the conservation vector U, applies to the general displacements, which are decomposed as follows:

$$q(t) = \bar{q} + \sum_{n=1}^{N_{pert}} q'_n(t) \tag{3.16}$$

$$q'(t) = \sum_{k=1}^{N_{harm}} \left(\tilde{q}_k e^{i\omega kt} + \tilde{q}_{-k}e^{-i\omega kt}\right) \tag{3.17}$$

$$q(t) = \bar{q} + \sum_{n=1}^{N_{pert}} \sum_{k=1}^{N_{harm}} 2\tilde{q}_{nk}(cos(\omega kt) + sin(\omega kt)) \tag{3.18}$$

As the physical displacement is related to the generalized displacement then also the physical displacement can be split into its mean and perturbation driven by the generalized displacements as:

$$x(t) = \psi q(t) = \sum_{m=1}^{N_{modes}} (\bar{q}_m + \sum_{n=1}^{N_{pert}} q'_{mn})\psi_m = \bar{x} + \sum_{n=1}^{N_{pert}} x'_n \tag{3.19}$$

$$\bar{x} = \sum_{m=1}^{N_{modes}} \bar{q}_m \psi_m \tag{3.20}$$

$$x' = \sum_{m=1}^{N_{modes}} \left[\sum_{k=1}^{N_{harm}} 2\tilde{q}_{mk} e^{i\omega kt} \right] \psi_m \tag{3.21}$$

As in flutter analysis there is only one perturbation, the system is at one frequency with just one mode and assuming no mean displacement. The physical displacement can be correlated as:

$$\vec{x} = 2\tilde{q}e^{i\omega t}\vec{\psi} \tag{3.22}$$

From equation above, the amplitude of the generalized displacement is of interest rather than its corresponding cosine and sine magnitudes, as in all cases the modulus of the corresponding harmonic content will be the unity. In order to guarantee a linear behavior of the general equation of motion, a physical displacement of 1% of the blade tip chord (c_{tip}) has been commonly used by different authors such as Zhai et al. [20], Sun et al. [48], Qui et al. [49] and Fruher and Vogt [50].

The method in which the Non-Linear Harmonic set up is defined within FINE™/Turbo is that it requires a mechanical coupling of the vibrating structure. An elastic deformation of modal type has to be set with a Forced Motion. In this case each generalized displacement per mode is imposed to retrieve its corresponding physical displacement. Thus, the amplitude of the harmonic generalized displacement can be rewritten on a general basis as Equation 3.23 and simplified as Equation 3.24 by substituting the physical displacement u as a function of a percentage ($X\%$) of the blade tip chord. As the effect of the generalized displacement is linear, a variation in the imposed physical displacement will produce also a linear response in the aerodynamic power.

$$\tilde{q} = \frac{u}{2|\psi_{max}|} \tag{3.23}$$

$$\tilde{q} = \frac{X\% c_{tip}}{2|\psi_{max}|} \tag{3.24}$$

3.7 Aerodynamic damping

One of the key parameters in current aeroelastic assessments is the aerodynamic damping. On a general basis, damping values have two main physical insights. The first is that it provides a representation of the direction of energy flowing within the system. And the second how fast is the feeding or dissipation of this energy in the system. On a similar basis, the aerodynamic damping determines whether or not the system is stable or not (e.g. flutter onset). The aerodynamic damping in general is a scaling or normalization from either the aerodynamic power or the aerodynamic work performed by the blade vibration in one period.

Throughout recent aeroelasticity history, multiple methodologies and definitions for obtaining this parameter have been assessed in literature. Some methods are proposed by Carta et al. [51], Verdon [52], Fransson [8], Panovsky and Kielb [21], Benvenuto et al. [23], Rice et al. [25], Mayorca [53], Debrabandere [54], Sun et al. [48]. Among these, the common terminology for this aerodynamic damping coefficient or Logarithmic-Decrement is, Ξ. Some of its mathematical representations are shown by Equation 3.25.

$$\Xi = -\sum_{i} \tilde{c}_{p_i} A_i sin(\phi_i) = -\frac{W_{aero}}{4KE_{avg}} = -\frac{W_{aero}}{\pi H u_{max}^2 P_{ref}} \tag{3.25}$$

A negative value of Ξ physically means that the aerodynamic force is supplying more energy into the structure by being in phase with the blade motion. This is an unstable condition, as the structure physical displacement would increase exponentially. On the other hand, if the value is positive means that the aerodynamic force is lagging the motion producing a dissipation of energy in the structure, in which no exponential growth will be present.

In recent investigations most of the authors adopt the logarithmic-decrement as it relates the work done by the blade with its average kinetic energy. Nevertheless, a *correct* definition of this parameter leads to a debatable topic as multiple options are available. As all of them are based on the energetic method, the main driver to determine a flutter-free condition is the sign of the aerodynamic work. Some authors, make use of the magnitudes of the aerodynamic damping to try to quantify how close or far from the stability limit the current operational condition is, Rice et al. [25]. In general, the aerodynamic damping is a scaling of the aerodynamic power done by the unsteady pressure over the blade surface due to its harmonic motion.

The suitability for each stability parameter depends on which physical properties are included to have a better physical insight of the stability parameter. Or against which reference data will be compared with. Nevertheless, is highly important to keep in mind that the selection of an interpretation of the aerodynamic damping is a scaling factor and its qualitative result is of a high interest. Another main important outcome from a flutter analysis is to interpret the results to find correlations between the steady and unsteady cases to the stability parameter.

3.8 Chapter conclusion

Flutter is an aeroelastic phenomena that has to be avoided at all costs, for all design conditions as it can be onset in matter of a couple of seconds. It produces an exponential increase in amplitude vibration that will lead to a structural failure. It can be self-limited by non-linear structural effects in which a HCF failure will occur. Currently, there is no method to predict flutter in advance. This phenomena is a function of the mode shape, operational condition, rows interaction, shock position, IBPA, among others. However, its assessment can be performed by an energetic method. The aerodynamic work done by the fluid over the blade is the main driver to determine the stability of the system. A negative sign means that the fluid is subtracting energy from the blade which generates a stable condition, whereas an unstable condition occurs when the fluid adds energy into the system, characterized by a positive sign of the work. NLH method provides a great advantage as all conservation variables are solved in the frequency domain. Unsteady computational costs are transformed into two steady computations. To guarantee a flutter free design, it is required to assess the full span of operational conditions per blade mode per disk mode (ND). The number of assessments increase its engineering and CPU costs quickly. Multiple definitions of aerodynamic damping are available in literature. The differences rely on the reference variables to normalize the aerodynamic work. A common reference to provide the aerodynamic damping is by the logarithmic decrement as it reassembles a physical insight as the mechanical damping. This is done by normalizing the work by the kinetic energy of the blade, which is still a scaling factor. A qualitative and quantitative damping assessment is normally done to determine how close to an onset flutter condition the system is. Lately, a common reference for the physical displacement is to impose 1% of the tip true chord, thus a percentage of the physical displacement will be set as reference as the effect of the generalized displacement is linear over the unsteady pressure as long as the displacement is small. Finally, among the reference literature it has not been found a method nor tool that enables engineers to produce a complete and automatic flutter set up and post process of results. Therefore, there is an opportunity to develop such a tool that can help the user to reduce the engineering time, such tool is introduced in the following chapter.

Chapter 4

Flutter Wizard tool

The Flutter Wizard tool will allow an automatic user-friendly interaction to investigate the aeroelastic stability of a single-stage or multistage configuration of one or multiple operation conditions. The aerodynamic damping stability by means of the aerodynamic damping coefficient from [39] versus the IBPAs will be provided as a final output for the user. If multiple operational conditions are selected, a performance map will be displayed indicating if each point stability status. The tool makes use of the Non-Linear Harmonic solution method available in FINE™/Turbo. The set up uses only one harmonic and one perturbation as flutter occurs only at one frequency which corresponds to its natural perturbation. The generalized displacement is set as the magnitude that allows the recover of the imposed physical displacement from its modal displacements. This process is shown by the Equation 3.24 in Section 3.6.

Therefore, the main scope is to provide intuitive and understanding guidance to any user, who is not fully involved in flutter within turbomachinery, in order to obtain a flutter stability curve. A comparison of timing between a full set without the tool and with the tool is introduced. One of the main benefits from the tools is to reduce the engineering cost and to produce reliable results independently from the user's experience.

The tool was developed in two modules. The first, corresponds to a class that contains all the available functions for the flutter wizard functionality. The second, is a main running file that calls the required functions to be used depending on the flutter type case. A Graphical User Interface (GUI) is not developed within the tool as it is out of scope. Nevertheless, the tool is implemented as to allow a straight-forward GUI development. Therefore, the tool asks for a minimum number of inputs from the user, these are dependent on the flutter case selected and whether or not is a single or multiple stage. These options provide the user versatility allowing a flexible interaction with the user. Its corresponding, flow charts in general and in particular are addressed in Section 4.1 and Appendix A.

4.1 Implementation

The development of the tool is based on the programming language Python 2.7, as an extensive quantity of inputs and commands from FINE™/Turbo have been adapted in this language. Currently, Python is used in multiple areas such as web development, engineering, software development among others. Details of its syntax and specific applications can be found in [55]. With Python, an oriented object programming methodology was used to provide a blocking-structure layout for robust implementation. The general flowchart of the tool is shown in Figure Figure 4.1. This figure displays a general insight of the logic within the flutter wizard tool. The tool was developed to have two types of flutter cases. These, are referred as

Case A and B. The former starts from a given steady state simulation, whereas the latter is initialized with an existing unsteady simulation. Case B takes into account if the user needs to have a specific set up that is not captured directly by the default configuration of the wizard, Case A, providing user flexibility.

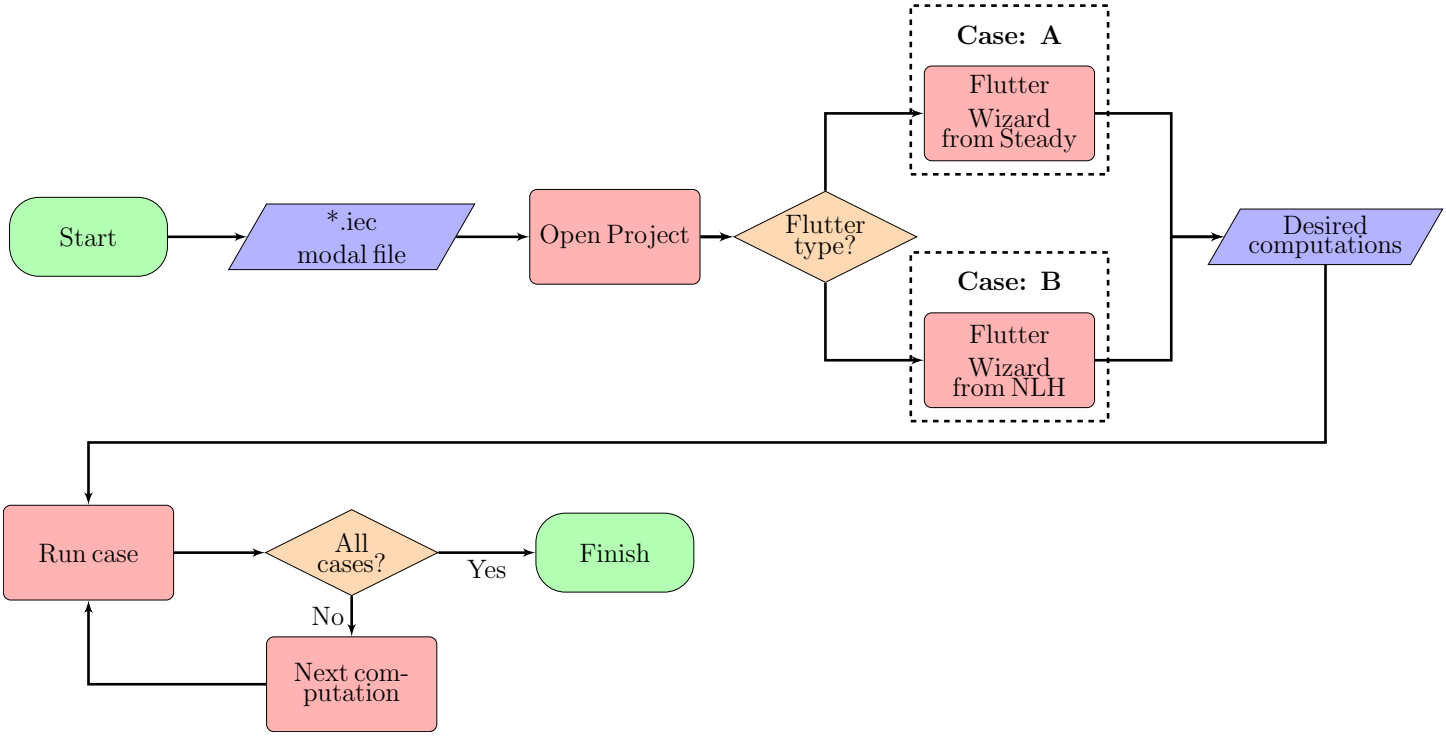

Figure 4.1: Flutter Wizard general flowchart

Both cases will ask the user a set of inputs as a function of the type of simulation provided and the chosen case. A default set up is also allowed for the user, if desired. However, mandatory inputs must be provided, such as the main working project directory path and its corresponding modal file. The modal file must be in agreement with the format specified by FINE™/Turbo User Manual [56]. The following input from the user is to select the type of flutter that will be set. The last input is to select the desired computations in which the tool will be executed along with the computational type (Serial, Parallel or Partition Parallel). In either case, an additional parameter of percentage of extra real memory input is required based on the user convenience. The last input block provides a main advantage, because it allows the user to potentially input the entire operational compressor map or just one operational condition. If multiple operational condtions are given as inputs,, a flutter stability map figure with the stability status (Flutter free or None-Flutter free) for each operational condition is generated.

Figure 4.2 displays a detailed flowchart of the blocks applied. The blocks are labeled with the first letter of the corresponding case and its corresponding counter. This blocking system allowed a straightforward usage From Case A blocks into Case B. The detailed flowchart of Case B can be found in Appendix A, which only contains two new blocks and the rest are used from the previous developed ones. Therefore, by a combination of including and removing blocks further cases can be superposed and implemented easily.

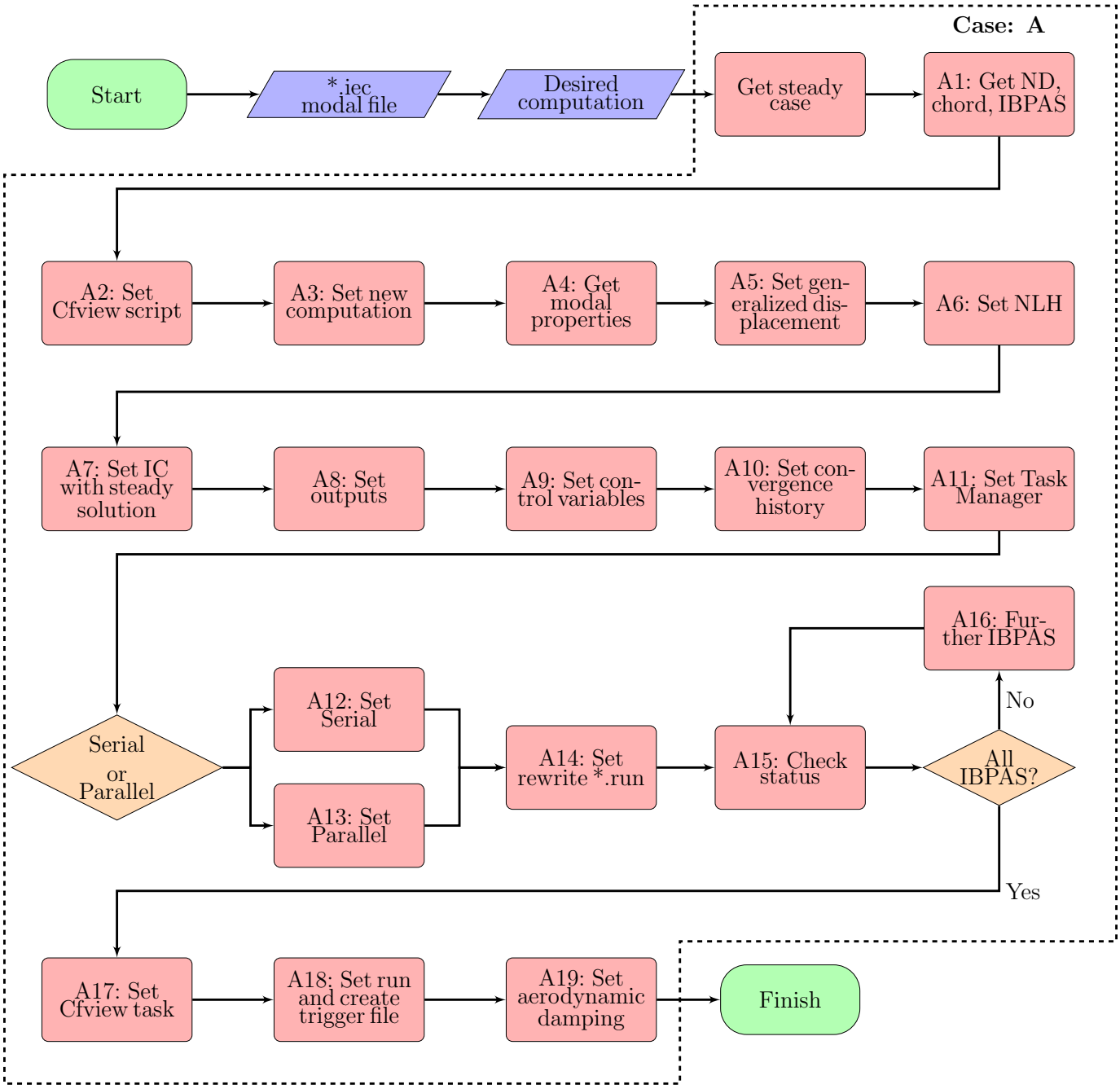

Figure 4.2: Flutter Wizard Flow chart: Case: A

For the sake of simplicity the blocks do not contain its specific steps, inputs nor outputs. Nevertheless, the above mentioned flowcharts provide a clear general step by step process. In each block an input-process-output methodology was used, allowing a straight forward cascade of information. Among all blocks, the key ones during the development process are: A1, A4, A5, A6 and A19. These blocks are the main driver to guarantee a correct flutter analysis within a turbomachine.

Block A1, determines if the selected computation is a single blade or multi row configuration. The user will provide which row will be varying its IBPAs in case of a multi row configuration. The available Nodal Diameters and IBPAs are determined as a function of the number of blades of the chosen row. Currently, there is no direct way to obtain the chord within FINE™/Turbo. Thus, a reconstruction of the intersection

locations from the given blade with the hub and shroud was developed. The intersection points are located at the leading edge and trailing edge of the blade. With them, the true chord is recovered. The average error with respect to the actual chord length has been found from a range between 0.03% and 1.3%. The intersection points are computed analytically, but the root cause from this variations is dependent on the precision in which the blade surfaces and sections were created. Nevertheless, the recovered true chord has been shown to be in agreement with multiple cases. One limitation of this block is that the blade should be generated by only one surface however, this characteristic does not always hold as the blades can be formed from multiple surfaces. When this condition occurs, this block will try to retrieve the chord and if an exception occurs it will ask the user to input the chord tip length in the units set within the mesh.

Block A4, locates the corresponding natural frequency and modal displacements from the selected mode to be analyze. At each nodal coordinate the modulus of the modal displacement is obtained to determine what is the maximum amplitude. Block A5, restricts the physical displacement to be a percentage of the blade tip chord. There is few available literature that provides a reference value, in the current available the target used was 1% of the blade tip chord. However, during the development it was concluded that in some cases this magnitude would not be robust. Thus, a proposed magnitude 0.5% percent of the tip of the true chord proved to work in all tested cases. Equation 4.1, shows that the physical displacement will have a linear scaling effect over the generalized displacement, which will be linearly related to the aerodynamic power. Therefore the setup of the generalized displacement by the desired physical displacement is the main driver to obtain reliable results by the FSI NLH method.

$$\tilde{q} = \frac{u}{2|\psi_{max}|} = \frac{0.5\% c_{tip}}{2|\psi_{max}|} \tag{4.1}$$

Block A6, sets up the FSI properties of the vibrating blade. It prescribes the desired natural frequency, IBPA, mean generalized displacement with its real and imaginary components. This block will be updated for every further simulation as the IBPA is modified until all IBPAs have been evaluated. By default the flutter wizard sets the entire harmonic amplitude recovered in Block A4 on its real component, leading to zero imaginary content. But it also allows the user to input a specific generalized displacement with its components, if desired. The balance of the real and imaginary components do not have any effect within the flutter analysis. The effect can be described by the complex unit circle. After one revolution of a cosine and a shifted cosine functions both will reproduce the same amplitude with just a shift of the starting point. Therefore, as the blade motion is harmonic, at only one mode, there will be no effect on the proportion of the amplitude in real and imaginary as long as the modulus is kept.

Finally Block 19, corresponds to the computation of the aerodynamic damping coefficient which will be provided for the user. The output aerodynamic damping coefficient is given by [39] definition as it is used in eleven standard configurations which up to date are still used as reference data. There are two outputs generated within this block. The first, a **_Aerodamping_stability.dat* file that contains the geometrical blade properties, reference pressure of the case and its modal properties of the analyzed condition. This file, also contains a status of "Flutter free" or "Non flutter free". This file provides four columns, corresponding to the IBPA, Nodal Diameter, aerodynamic damping Ξ, and the aerodynamic power. The second output, is in a (**_Aerodamping_stability_curve.png*) format, which contains the flutter stability curve. This curve, displays the variation of the aerodynamic damping coefficient against its IBPAs. Which as a remainder, every value below zero has a physical interpretation of unstable vibration amplitude.

4.2 User application and time reduction

Assuming a modal analysis has been already performed, the time required to make an accurate first flutter assessment for a specific mode and IBPA is directly proportional to the amount of user's expertise. Thus, the total time for an analysis can be split in engineering and computational time. In most cases the computational time will be from the same order of magnitude, regardless of the user's experience. However, engineering time will be directly dependent on the previous experiences and theoretical background from the user.

As reference, starting from a given steady state analysis and without any reference on the generalized displacement. The time required to get the first set up with a background in aeroelasticity but not in NLH with FSI in FINE™/Turbo, for a 20 bladed single row case is around 40 min and a post processing of around 15 min after all computations have finished. Therefore, a key target within the flutter tool is that the setup time could be independent of the user's background in aeroelasticity. This would lead to a considerable, reduction in engineering time. The engineering time then becomes a function of the number of available IBPAs within the desired row to be analyzed and the post processing method. For the above mentioned reference case in which the previous timings were extracted, when the tool is applied it takes around 45 seconds, after all inputs were set, to get all the cases with an automatic post process of results. This represents around 1.3% of the engineering time previously mentioned, which is a remarkable reduction and satisfies a key objective of this thesis.

An example of the tool application for an automatic and a user defined case are shown in Figures 4.3 and 4.4. The former, shows that for an automatic set up only 8 inputs are required after selecting case A, in which the default values are within parenthesis. The latter, case corresponds to a multistage analysis with multiple blades vibrating in which it would require for this case 22 inputs, if the user would like to define all parameters. Additionally if the user inputs a "q" will automatically exit the script, allowing an exit at any given input. The range of variation in the number of inputs is a consequence of allowing flexibility with the user interaction. This flexibility targets the objective of providing a user-friendly tool.

```
**** USER INPUT ****
Select the type of solution
Select (1) for a Steady Solution (2) for an NLH
Enter the desired value you want (1):   1

**** USER INPUT ****
Which computation is the steady?
Enter the desired values you want (1):  3

**** USER INPUT ****
Select (1) for Serial computation, (2) for Parallel computation or (3) for Parallel partition computation
Enter the desired value you want (1):   1
The default increase of memory percentage is:   1.5

**** USER INPUT ****
Select (1) for keeping it or (2) to increase the memory
Enter the desired value you want (1):

**** USER INPUT ****
Select (1) for automatic set up or (2) for a specific IBPA
Enter the desired value you want (1):

**** USER INPUT ****
Select (1) for automatic set up or (2) for a specific mode
Enter the desired value you want (1):

**** USER INPUT ****
Select (1) for automatic set up or (2) for a specific physical displacement
Enter the desired value you want (1):

**** USER INPUT ****
Select (1) for automatic set up or (2) for a specific generalized displacement
Enter the desired value you want (1):

**** USER INPUT ****
Select (1) for automatic set up or (2) for a specific steering control variables
Enter the desired value you want (1):
```

Figure 4.3: User inputs for automatic setup

```
**** USER INPUT ****
Select the type of solution
Select (1) for a Steady Solution (2) for an NLH
Enter the desired value you want (1):

**** USER INPUT ****
Which computation is the steady?
Enter the desired values you want (1):  3

**** USER INPUT ****
Select (1) for Serial computation, (2) for Parallel computation or (3) for Parallel partition computation
Enter the desired value you want (1):
Error in the input. Enter an integer or "q" to exit
Enter the desired value you want (1):   2

**** USER INPUT ****
Insert the number of processors:
Enter the desired value you want (1):   2
The default increase of memory percentage is:   1.5

**** USER INPUT ****
Select (1) for keeping it or (2) to increase the memory
Enter the desired value you want (1):   2

**** USER INPUT ****
Insert the new percentage increase in  memory:
Enter the desired value you want (1.2):

**** USER INPUT ****
Insert the number of reals in  memory:
Enter the desired value you want (3000.0):

**** USER INPUT ****
Insert the number of integers in  memory:
Enter the desired value you want (30):

**** USER INPUT ****
Input which row will be varied its IBPA$
Enter the desired value you want (1):   2

**** USER INPUT ****
Input which other rows will be vibrating as well or "None" to finish this input
Enter the desired values you want (None):

**** USER INPUT ****
Select (1) for automatic set up or (2) for a specific IBPA
Enter the desired value you want (1):   2

**** USER INPUT ****
Insert the desired IBPA:
Enter the desired value you want (0):

**** USER INPUT ****
Select (1) for automatic set up or (2) for a specific mode
Enter the desired value you want (1):

**** USER INPUT ****
Select (1) for automatic set up or (2) for a specific physical displacement
Enter the desired value you want (1):   2

**** USER INPUT ****
Insert the physical displacement in 0.001 units:
Enter the desired value you want (1):   2.05

**** USER INPUT ****
Select (1) for automatic set up or (2) for a specific generalized displacement
Enter the desired value you want (1):   2

**** USER INPUT ****
Insert the real generalized displacement:
Enter the desired value you want (1):   0.5

**** USER INPUT ****
Insert the imaginary generalized displacement:
Enter the desired value you want (0):   0.1

**** USER INPUT ****
Insert the mean generalized displacement:
Enter the desired value you want (0):   0.001

**** USER INPUT ****
Select (1) for automatic set up or (2) for a specific steering control variables
Enter the desired value you want (1):   2

**** USER INPUT ****
Insert the maximum number of iterations:
Enter the desired value you want (300.0):

**** USER INPUT ****
Insert the convergence criteria:
Enter the desired value you want (-6):

**** USER INPUT ****
Insert the saving frequency:
Enter the desired value you want (100):
```

Figure 4.4: Flutter Wizard: Custom option

4.3 Flutter Wizard outputs

A representative example of the final outputs provided by the Flutter Wizard are shown in this chapter, shown in Figure 4.5. For each operational condition, a figure and a file are created. In case of multiple operational conditions as input an additional figure is created to show the stability flutter map. All outputs are stored in the directory in which the project file (*.iec) is located.

Figure 4.5a, shows the stability file layout of the ouput **_Aerodamping_stability.dat*. The first row shows the title of the file. The second displays a flag that explains if flutter was encounter or not. The next eight lines correspond to the mesh units, blade tip chord, reference pressure of the steady state simulation, analyzed mode, real component of the generalized displacement, imaginary component of the generalized displacement, natural frequency of the selected mode and the physical displacement, which is in mesh units. The following line contains three columns which shows the IBPA variation, the resultant aerodynamic damping coefficient Ξ and the aerodynamic power obtained for each case. Figure 4.5b, shows the stability curve output, in which all values above zero are stable conditions and all values below zero mean that flutter is being onset. The layout naming for this figure is **_Flutter_stability_curve.png* in which the base name is the steady state computation and is recovered from the first and second column of **_Aerodamping_stability.dat* file .

```
Aerodynamic damping file output
Stability status:   Non Flutter free case
Units = 1.00000e-03
Chord = 1.690e+02
Reference Pressure = 1938.031 [Pa]
Mode analyzed =  1
Generalized displacement real = 1.009e-03
Generalized displacement imag = 0.000e+00
Natural frequency = 132.080 [Hz]
Physical displacement = 2.05000e-03
IBPA[deg]       Xi[-]               Aeropower[W]
-177.23         5.5276e+00          -2.0098e+00
-171.69         5.0897e+00          -1.8506e+00
-160.62         4.0445e+00          -1.4706e+00
-149.54         3.1759e+00          -1.1548e+00
-138.46         2.7939e+00          -1.0159e+00
-127.38         2.5443e+00          -9.2510e-01
-116.31         1.8449e+00          -6.7081e-01
-105.23         3.5203e-01          -1.2800e-01
-94.15          -1.8454e+00         6.7098e-01
-83.08          -3.3419e+00         1.2151e+00
-72.00          -3.5225e+00         1.2808e+00
-60.92          -3.0671e+00         1.1152e+00
-49.85          -1.9964e+00         7.2588e-01
```

(a) Flutter Wizard: Aerodynamic damping stability file

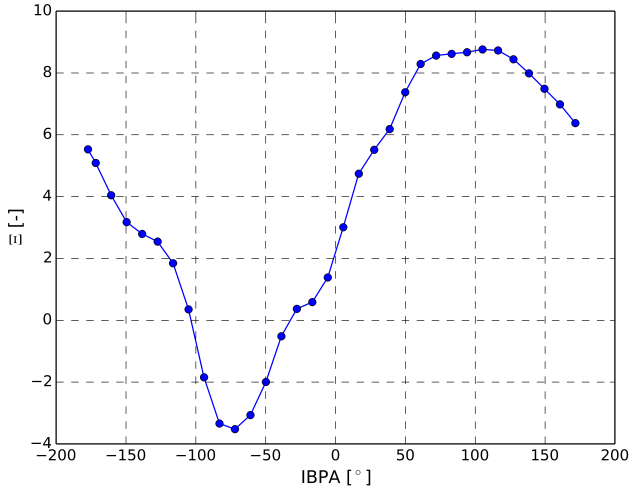

(b) Flutter Wizard: Aerodynamic damping stability curve

Figure 4.5: Flutter Wizard Outputs: Stability curve and stability file.

Thus, these outputs provide a full assessment of the stability of the system by providing the user a visual assessment of the stability. By providing all the reference data to the user in case, it is possible to obtain a different scaling factor for the aerodynamic work. Therefore, this provides flexibility to the user even in the post processing of the results, achieving a flexible and user-friendly environment.

4.4 Chapter conclusion

A flutter wizard tool has been developed with Python 2.7 within FINE™/Turbo to produce and automatic FSI set up with the Non-Linear Harmonic method by prescribing the generalized displacement. The tool provides an automatic set up which detaches the user expertise from a reliable flutter assessment. The tool is set up to work with one harmonic and one perturbation which represents flutter phenomena in turbomachinery. The aerodynamic power is directly related to the desired physical displacement, which has been prescribed as 0.5% of the true chord tip. The tool is able to work on a single or multiple rows, for a single or multiple operational conditions. The wizard has been designed to provide flexibility to the user to achieve a user-friendly inputs. Two types of flutter types are available within the Flutter Wizard, the first starts from a steady state case and the second from a given NLH-FSI case, in case a particular set up is required. A strong reduction in time invested to have a complete set up of a 20 bladed single turbine row, from around 55 minutes including post processing time to $\approx 45s$ by just imposing only 8 default inputs for an automatic set up. This time reduction represents only 1.3% of the time used without the wizard, proving a great advantage in terms of engineering time reduction. The wizard outputs a *_Aerodamping_stability.dat* file with its corresponding stability curve **_Aerodamping_stability_curve.png*. The first file, contains all the physical data used to obtain the aerodynamic damping coefficient by means of Fransson scaling factor as it still currently used in eleven standard configuration cases, and the computed aerodynamic power. These files are created for each operational condition analyzed. Additionally, in case multiple operational conditions are selected by the user, a stability map is created. The stability map relates the pressure ratio and mass flow, in which at each operational it is highlighted the stability status. The next chapter introduces the usage of the developed tool into multiple configurations, in which a detailed comparison against reference data is done.

Chapter 5

Validation

In order to assess the results provided by the automatic set up of the Flutter Wizard, it is mandatory to have a reference frame of contrast. Experimental data is the primary target which is assumed to be the most reliable source, and most of the time taken as *The truth*, which does not always hold. In the turbomachinery field, reliable experimental data is challenging to obtain and rare to encounter in open literature. Additionally, experimental data in aeroelastic turbomachinery is sparse. However, in the late 1980's a comprehensive and detailed set of different configurations of cases were analyzed in steady and unsteady conditions in which comparison of experimental and theoretical results by Bölcs & Fransson [57] at the University of Lausanne. These configurations are still up to date used to validate numerical codes. An additional case was also developed afterwards on the same experimental rig facility, leading to a total of 11 standard configurations (STCF).

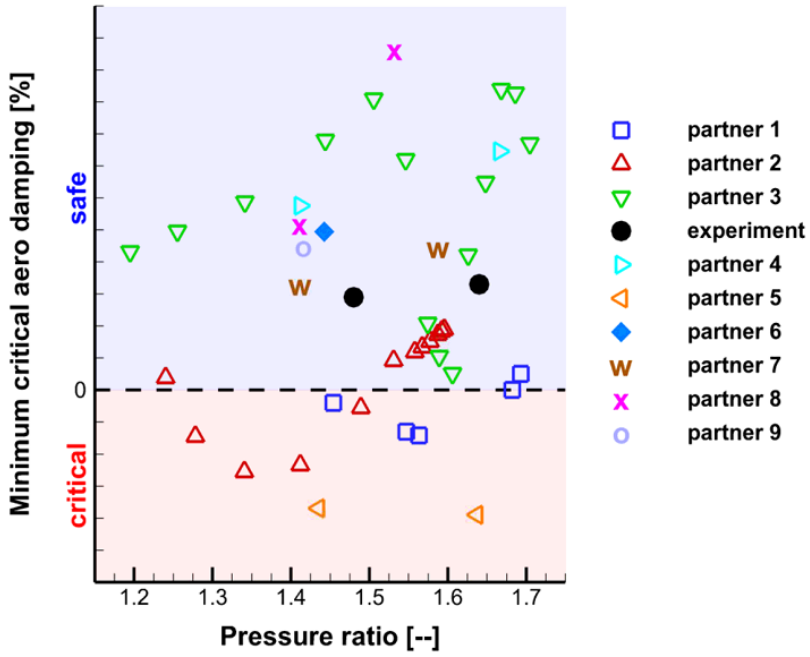

Figure 5.1: OEMs flutter prediction, Holzinger et al. [6]

Despite the multiple advances in numerical techniques in aeroelasticity, there are still significant differences in results, mainly due to the different methodologies and solvers used. An example of these differences can be found in Figure 5.1. This figure, shows the least aerodynamic damping for multiple pressure ratios and compared to the experimental results. These results were obtain by multiple Original Equipment Manufacturers (OEMs) and Universities with their own best practices and in-house solvers. The results provide a clear difference despite the fact that all of them analyze the same case as shown by Holzinger et al. [6]. Therefore, it is mandatory to have a verification process. In this thesis among these eleven standard configurations (STCF), two have been chosen. The selected configurations are: STCF4 and STCF11, which correspond to turbines cases with a bending prescribed motion, representing the first bending mode. These cases, were used as comparison reference against the results obtained from FINE™/Turbo.

In all cases the resultant data is analyzed at 50% of the blade height. The imposed blade motion generates a non-zero displacement at the hub. Details of this profile can be found in Jöcker [58] which corresponds to STCF11 as a function of the operational conditions. Also, Ott [59] establishes that the results obtained on STCF4 match when the motion location is the same as STCF11. However, it is not mentioned from which operational condition the motion is imposed. Case B from the flutter wizard tool was used in STCF11 and STCF4. This case had to be selected, as the prescribed motion include movement of the hub. The inclusion of the hub on the modal displacement is a particular case as in general it only corresponds to the blade. Additionally, the specific blade displacement that is prescribed is not dependent of the blade chord. Thus, in order to have a quantitative contrast the Flutter Wizard was used by specifying a generalized displacement and to retrieve the aerodynamic damping coefficient stability curve. After obtaining the curve, both experimental al numerical results were compared at the same reference IBPA of 180°, so as the least and most stable conditions.

5.1 Standard Configuration 11

This configuration is one of the most common used as reference for comparison of numerical codes. Examples of usage of this configuration has been done by Rice et al. [25], Patil et al. [45], Cinnella et al. [60], Debrabandere [61], He [62]. This case corresponds to a test rig with 20 turbine blades designed for an isoentropic Mach number outlet of 1. The general geometrical characteristics of the blades are found in Table 5.1.

STCF 11	
c [mm]	77.8
γ [°]	- 40.85
τ [mm]	56.55
b [mm]	40
h_{gap} [mm]	0.8

Table 5.1: STCF11: Blade geometrical characteristics

This configuration has two operational conditions (OPC) with their corresponding experimental results. The first operational condition (OPC1) corresponds to the design point, which is a high-subsonic flow. The second (OPC2) is at off-design point with a transonic flow with high inflow angle. Each of these cases contains numerical and experimental results of the first harmonic content of the unsteady pressure.

However, only at $\sigma = 180°$, all numerical results are available in terms of harmonic pressure coefficient and phase. The full aerodynamic damping stability curve is just available for a potential flow solver. The description of the mean operational conditions are found in Table 5.2. The boundary conditions were recovered from [63], where further details can be found.

STCF11		
	Subsonic case (OPC1)	**Transonic Off-design (OPC2)**
M_1 [-]	0.31	0.4
β_1 [°]	15.2	34
$M_{2_{is}}$ [-]	0.69	0.99
k [-]	0.2134	0.1545
u/c [-]	0.0054	0.0035
f [Hz]	209	212
P_{t_1} [kPa]	124.6	229.8
P_1 [kPa]	116.4	206.3
P_2 [kPa]	90.7	122.4

Table 5.2: STCF11: Operational conditions

5.1.1 Steady state results: OPC1

Within the first operational condition, a mesh independence analysis was perform to obtain the best trade off between CPU resources and accuracy. Three meshes cases were analyzed: Coarse, Medium and Fine. The mesh properties are shown in Table 5.3. The selection of the first cell height from the wall is suggested in the user manual of FINE™/Turbo [56] and [64] by Equation 5.1 corresponding to the Blasius equation. Where the dimensionless height y^+ is set between a range from 0.1-50. The range of values shown in Table 5.3 are the ones obtained after achieving a converged solution.

$$y_{wall} = 6 \left(\frac{U_{ref}}{\nu} \right)^{-\frac{7}{8}} \left(\frac{L_{ref}}{2} \right)^{\frac{1}{8}} y^+ \tag{5.1}$$

Additionally, Table 5.3 shows that the physical properties such as efficiency, torque, thrust, mass flow and pressure ratio does not display any significant change. The variation of these magnitudes are around 1.8% from Coarse to Fine. The variation from Medium to Fine can be neglected as they are lower than 0.1%. Concluding that a mesh independence convergence have been obtained, being the medium mesh the one that produces the best trade-off of accuracy versus computational time.

	Mesh 1 Coarse	Mesh 2 Medium	Mesh 3 Fine
Number of points $[1E6]$	≈ 0.75	≈ 1.6	≈ 2.2
y^+	1.21-18.4	0.0659-5.741	0.0665 -5.74
Spanwise points	49	105	121
Efficiency [%]	91.00	90.35	90.31
Torque $[N \cdot m]$	-226	-221.9	-221.9
Thrust $[N]$	1033	1045	1045
Mass flow $[kg/s]$	6.091	5.98	5.981
Pressure ratio	0.976	0.9742	0.9741

Table 5.3: STCF11 OPC1: Physical outputs variation due to mesh independence

In this configuration and in all the following, a mesh independence study was performed by comparing the isoentropic Mach at 50% of the blade span against the normalized true chord (c_n). Additionally, as second instance with the numerical and experimental reference data. Numerical results come from potential small perturbation flow (FINSUP), linearized Euler (NOVAK), non-linear Euler (INST) and non-linear viscous flow solvers (VOLFAP). For comparison purposes only the viscous flow results and the experimental are kept. The non-linear viscous flow solver (VOLFAP) is prescribed with Baldwin-Lomax as turbulence model whereas the obtained results have Spalart-Allmaras as turbulence model.

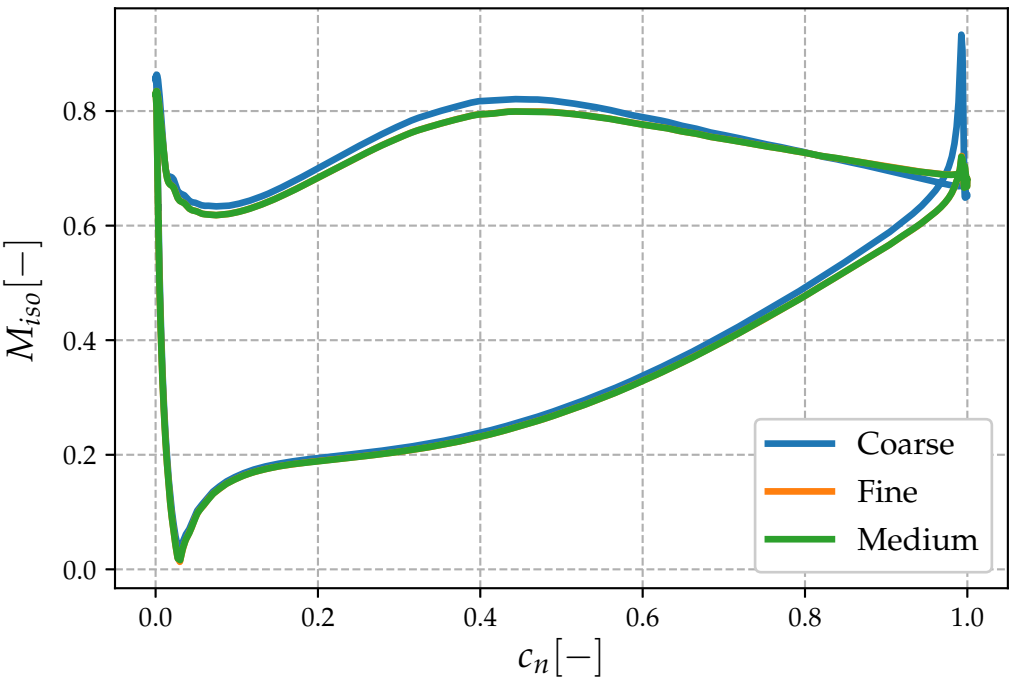

Figure 5.2: STCF11 OPC1: Mesh independence of M_{iso} vs c at 50% span

The variation of the isoentropic Mach number during the mesh independence analysis is shown in Figure 5.2. The results from the three cases on the pressure side are almost identical until 80% of the chord where an over prediction of accelerations is shown by the Coarse mesh. The suction side are slightly

different at the maximum acceleration of the flow around 40% of the chord. At this location, the Coarse mesh predicts a slight higher isoentropic Mach number than the other meshes. Medium and Fine meshes are in fact overlapping in the plot as they provide identical results. Therefore, it is accurate to proceed with the experimental comparison with the Medium mesh and correlate the physics of the results.

Figure 5.3 shows the isoentropic Mach number at 50% of the span comparing the Medium mesh solution against the reference data. From a general view, the result obtained by FINE™/Turbo is in agreement with the experimental results in both pressure and suction sides. VOLFAP results are closer to the results obtain with the coarse mesh with differences in the pressure side (PS) around 70%c_n and on the suction side (SS) at 40%c_n. This changes occur in regions with higher static pressure gradients. This difference might be because VOLFAP case was run with ≈8350 elements in the mesh. Therefore, as VOLFAP results have a similar trend as found previously in a not refined mesh and the experimental data match with the current results, it is assumed that this steady case is valid and can be used as an input for the unsteady analysis.

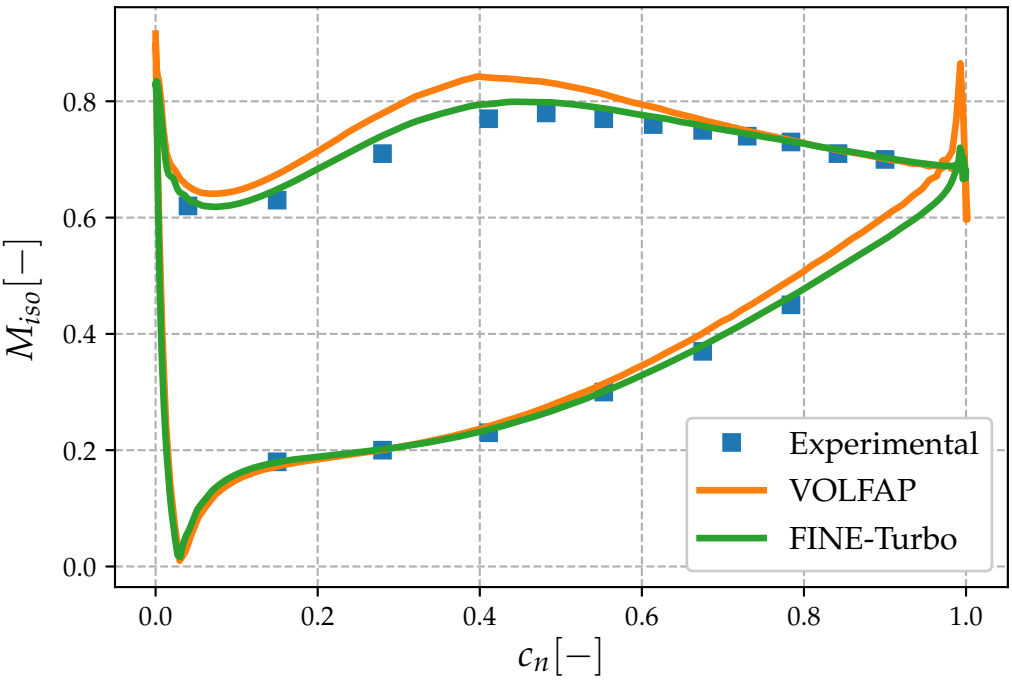

Figure 5.3: STCF11 OPC1: Validation of M_{iso} vs c at 50% span

Figure 5.4 displays the Mach number contour at 50% of the span. The stagnation point is close to the trailing edge at the PS. At the leading edge of the SS, the flow's momentum is increased locally and as the incidence angle is not as abrupt (≈ 16°), the flow is kept fully attached. As the fluid moves from leading edge to trailing edge the flow is accelerated again to its maximum close to the 40% of the blade chord. Along the PS the flow has less velocity gradients until the trailing edge. At this region the SS and PS flow mixes leading to local separation at the trailing edge. Numerical results from VOLFAP over predicted the velocity at these regions, in which the maximum velocity is found, in accordance with in Figure 5.3.

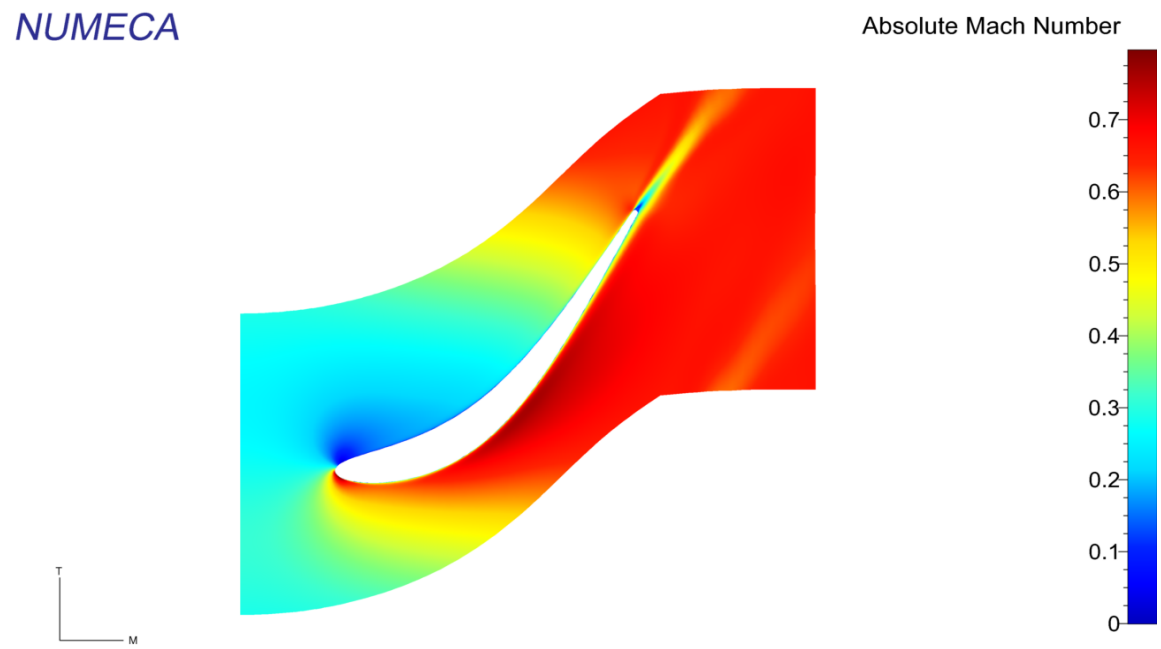

Figure 5.4: STCF11 OPC1: B2B Mach Number view at 50% span

5.1.2 Unsteady results: OPC1

After guaranteeing a reliable steady state solution, an unsteady analysis was performed by using the developed Flutter Wizard tool. This case required to be analyzed on a B case as the hub had a prescribed movement which is not capture by the default configuration of case A. Thus, a specific NLH set up was developed in FINE™/Turbo to initialize the Wizard. The first harmonic content, phase and harmonic pressure coefficient, of the unsteady pressure is the main driver to be compared. Additionally as the aerodynamic damping coefficient is the main output from the Flutter Wizard tool, it will be compared against the references as well. The definitions of the above mentioned quantities are display below as specified in the standard configurations.

$$\tilde{c}_p = \frac{c}{uP_{ref}}\sqrt{P_{real}^2 + P_{imag}^2} \tag{5.2}$$

$$P_{ref} = P_{t_1} - P_1 \tag{5.3}$$

$$\phi = arctan\left(\frac{P_{imag}}{P_{real}}\right) \in [-180°, 180°] \tag{5.4}$$

$$\Xi = -\sum_{i=1}^{n} \tilde{c}_{p_i} A_i sin(\phi_i) \tag{5.5}$$

Where A_i in Equation 5.5, is the local normalized area by the chord of the i^{th} element in which the harmonic content has been measured. The local phase is represented by ϕ_i and the local pressure coefficient by $\tilde{c}_{p_i}$. This equation can be rewritten in terms of the aerodynamic power as shown in Equation 5.6, which is refer as Fransson aerodynamic damping coefficient.

$$\Xi = -\frac{\dot{W}_{aero}}{2u^2 P_{ref} f c} \tag{5.6}$$

The reference location for the comparison of the phase and pressure coefficient amplitude is at 50% of the blade span. The specific physical displacement imposed by Jöcker is shown in Equation 5.7. It is as a function of the blade height H with coefficients L_{shaft}, L_0 and L_{0r} obtained from the experimental setup [58]. Finally $(u/c)_{mid}$ is the reference location at which the measurements were taken, in which for this case is 0.0054.

$$u = \frac{(u/c)_{mid}}{H_{mid} + L_{shaft} + L_0 - L_{0r}} \left(H + L_{shaft} + L_0 - L_{0r}\right) c \tag{5.7}$$

By using Equation 3.23 the generalized displacement can be rewritten as Equation 5.8, which is clear that as the modulus of the imposed displacement ψ is in fact the prescribed displacement u so the generalized displacement is reduced as 0.5.

$$\tilde{q} = \frac{u}{2|\psi|} = 0.5 \tag{5.8}$$

The aerodynamic power is computed as Equation 5.9 as specified in FINE™/Turbo Manual [56]. Where the first argument of the integral is taking into account force done by the pressure and viscous effects and $\vec{V}_g$ corresponds to the velocity of the deforming wall of the grid.

$$\dot{W}_{areo} = \int_S \left(P\vec{n} + \tau\vec{t}\right) \vec{V}_g dS \tag{5.9}$$

The initial unsteady results presented an oscillating convergence history, mainly in global residual variations and harmonic residuals as well. In order to have a smoother convergence some parameters in the flow solver were updated based on best practices obtained at the company. The details of the expert parameters modifications are found in Table 5.4. The effect of this parameter to achieve convergence has been assessed by Debrabandere [54]. These changes provided a clear effect in the stability of the system, with a small variation in the aerodynamic power $\approx 3\%$ but as the linear behavior was still retrieved it is assumed this does not produce any significant change.

Therefore, after setting up the first NLH condition with a generalized displacement of 0.5, the Wizard was run. All computations were performed on a computer with processors Intel(R) Xeon(R) CPU E3-1230 v5 @ 3.40GHz. The tool set up the entire range of IBPAs in $\approx$ 45 seconds and the full stability was analyzed and post processed after around 34 hours with 3 processors. For each IBPA analyzed, the tool saved the aerodynamic power to later be post processed as described above. The output from the *_*Aerodamping_stability.dat* file is shown in Figure 5.5. All values below the red horizontal line are cases in which the system is unstable, meaning the unsteady aerodynamic force is feeding energy into the system. In this figure two IBPA conditions are unstable ($\sigma = -54\,^\circ$ & $-36\,^\circ$), occurring on a backward traveling. For this operational condition the reference pressure retrieved by the Wizard is $P_{ref} = 6901.574\ Pa$. Therefore, by making use of the Flutter Wizard, the global stability of the operational condition was obtained automatically and it is predicted that it is not a stable condition. However, in order to have a

Solver expert parameters	
Parameter	Value
CORMOD	1
HAVMOD	3
IBOTH	1
IDISMO	42
MVGAP	1
HARAV2	1E-3
VIS2	0.5
VIS4	0.05

Table 5.4: FINE™/Turbo expert parameters modifications

detailed comparison of the harmonic content a manual contrast against the experimental and numerical reference data will be presented.

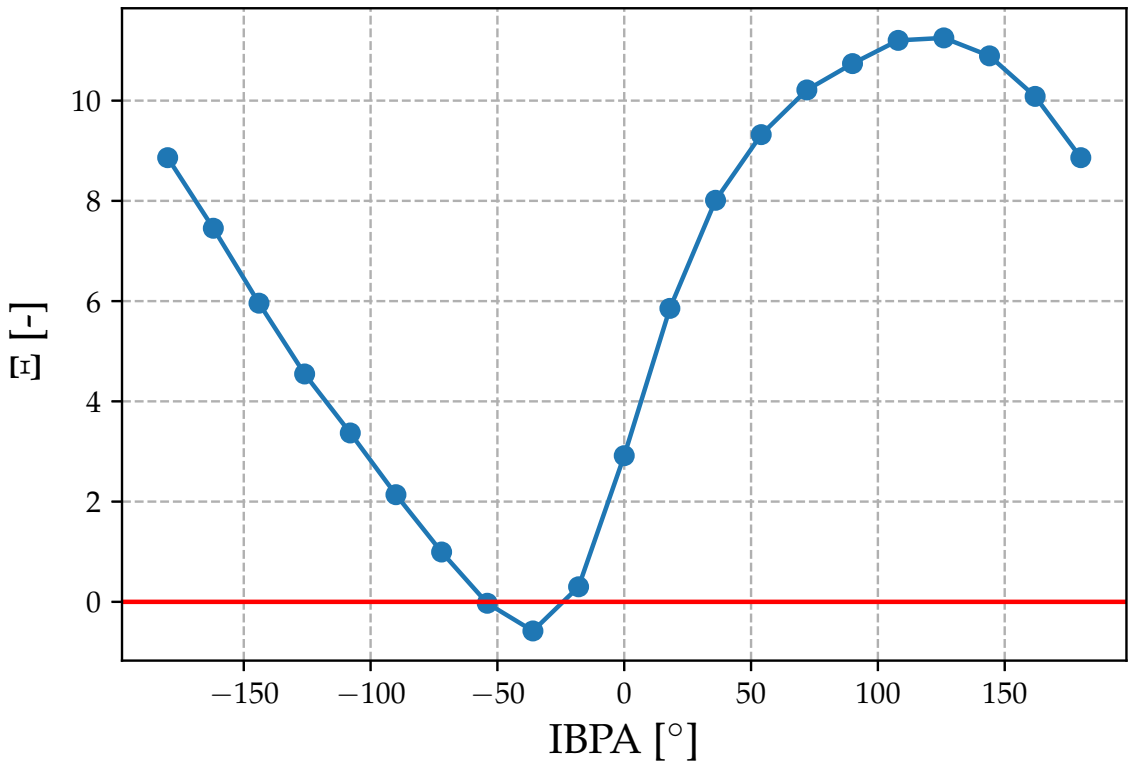

Figure 5.5: STCF11 OPC1: Aerodynamic damping coefficient output from Flutter Wizard tool

The reference IBPA that will be used to compare results is $\sigma = 180°$ as is the only IBPA which contains results for the experimental results and the multiple numerical references. The comparison of results between the multiple methods within this case is observed in Table 5.5. Additionally, FINSUP solver is the only solver that contains the IBPA variation with its corresponding stability coefficient. The obtained result is in agreement with the solvers and in particular with VOLFAP with a difference of 4.5%.

$\sigma = 180°$	
Software	Ξ
FINSUP	10.8
NOVAK	9.1
INST	9.7
VOLFAP	8.4
FINE™/Turbo	8.8

Table 5.5: Unsteady aerodynamic damping comparison

For a further comparison, Figure 5.6 shows the comparison among, the current results, VOLFAP, Experimental, and Patil et al. [45], who used a commercial software (CFX™) with an harmonic method. The comparison quantities are the phase and harmonic pressure coefficient. In this figure, the experimental results are shown by blue squares and this will be used for all further cases. Sub figure 5.6a displays that along the pressure side all results predict an in-phase condition but at the trailing edge. Experimental data suggests a smooth trend up to 60% of the chord when a phase increase is predicted; this trend is not captured by FINE™/Turbo. Patil and VOLFAP predict an increase in the phase as moving towards the trailing edge. Regarding the suction side all numerical results over predict the location in which the change of phase occurs by the experiments. The experiment predicts the change around 25% of the chord, which is before the maximum acceleration point. This might have kept increasing the phase until the discontinuity which produces a jump. In general the three numerical methods have the same trend with the only difference of the out of phase region.

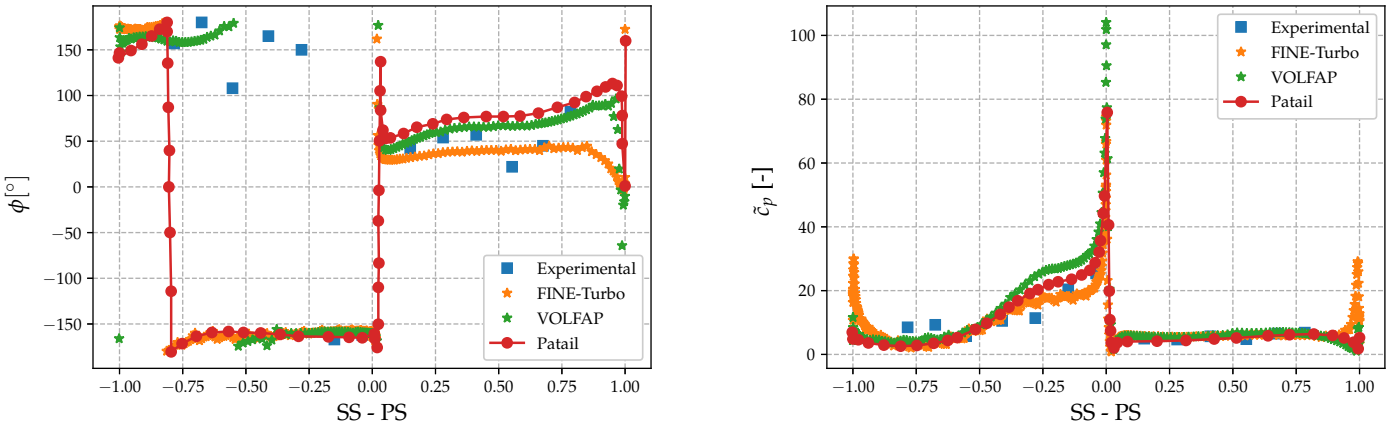

(a) ϕ : $\sigma = 180°$

(b) $\tilde{c}_p$: $\sigma = 180°$

Figure 5.6: STCF11 OPC1: Harmonic content at $\sigma = 180$ ° at 50% span

Sub figure 5.6b displays the contrast in the harmonic pressure coefficient. In this case all the four methods are in agreement with one another, with variations towards the trailing edge. This variation is assumed to be either because of a high mesh refinement at the trailing edge and also the moving elements at this region have high harmonic gradients at the wake, which might produce the peaks. The pressure side is in general with good agreement, whereas the main differences occur at the suction side within its first quarter of the chord. In this region FINE™/Turbo and Patil et al. are in good agreement with the experimental results. It has been found that the amplitude is not as sensitive as the phase. Thus, it is

concluded that the result for $\sigma = 180°$ is in agreement with the experimental data.

Finally, a physical approach of the results is obtained by recovering the aerodynamic stability coefficient. It, is obtained by the relation between the phase and pressure coefficient. As a reminder, a positive phase means that the unsteady aerodynamic force is leading the motion of the blade (unstable) whereas a negative phase the force is lagging the motion (stable). For instance the phase at the SS from FINE™/Turbo results, is almost constant around 50 degrees in-phase. However, the amplitude of $\tilde{c}_p$ is small all along the same region, thus the unsteady effect is diminished by this counter effect. On the other hand, the suction side phase has stable and unstable regions, but from 0 to 75% of the chord is stable. Most of the high amplitude of $\tilde{c}_p$ are occurring within this chord range and therefore in general at this location the stability parameter would be positive.

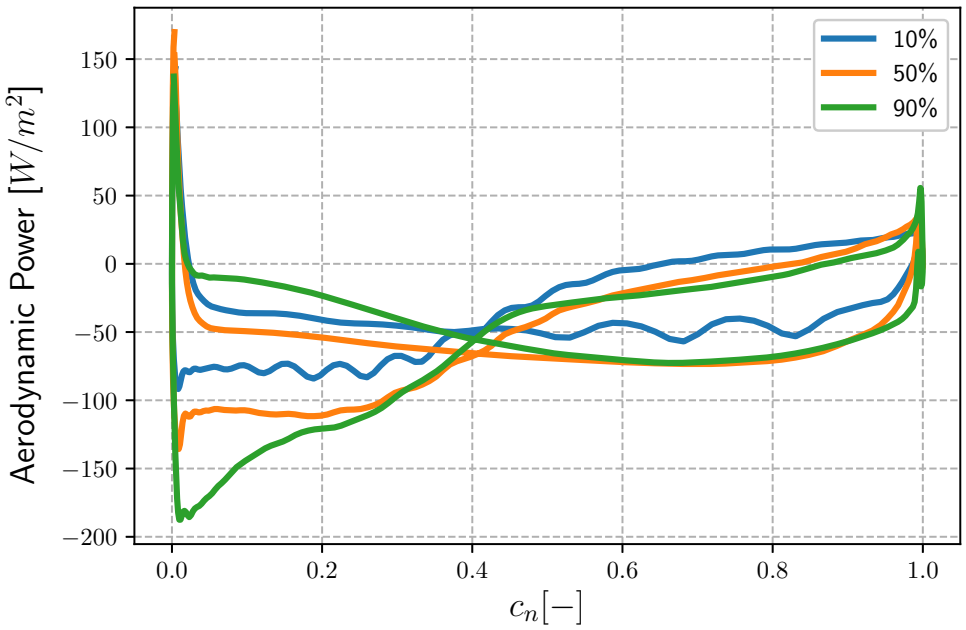

Figure 5.7: STCF11 OPC1: Aerodynamic power per unit surface vs chord at different blade heights

Figure 5.7 displays the variation of the aerodynamic power, along the blade height, per unit area. The evaluated sections are 10%, 50% and 90% of the blade height. Most of the aerodynamic power is obtained at the tip of the blade, which correlates with the imposed bending motion. The leading edge produces the highest contribution, whereas the trailing edge produces an unstable effect. The unstable area is small compared to the stable region, therefore it does not provide a global unstable effect. Both surfaces produce almost the same aerodynamic power at 40% of the chord, it is unclear the root cause of this intersection location.

Figure 5.8 shows the contrast of aerodynamic damping coefficient among FINE™/Turbo, FINSUP and Patil et al. In this figure, the IBPA range from the Wizard was modified to be in agreement with the reference data. There is a clear difference in maximum amplitude in the most stable and least stable cases. The current results and Patil et al. predict an unstable condition at $\sigma = 324°$. The aerodynamic damping coefficient is a scaling of the aerodynamic work done by the blade, its qualitative properties are of higher

interest than its quantitative magnitude which can be affected by the reference pressure and the reference physical displacement. In order to reduce this potential variations and to recover the proportional aerodynamic work per IBPA, the aerodynamic stability coefficient is normalized against its maximum for each case. Sub figure 5.8b shows the normalized trend, which highlights that the same rate of work per IBPA is conserved from most of stability curve. Therefore, this figure removes the apparent differences and have a better qualitative and quantitative contrast

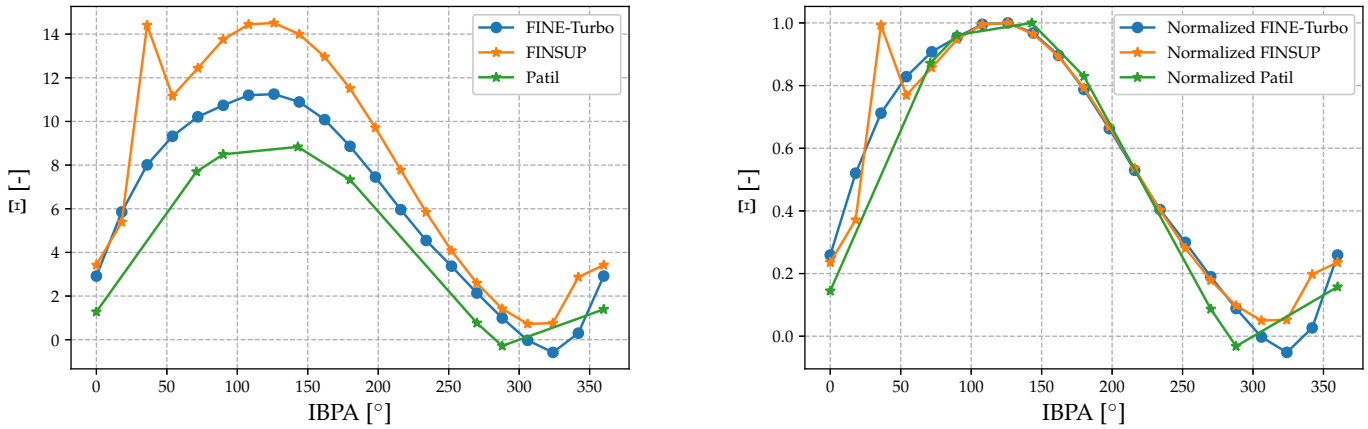

(a) Stability Parameter vs IBPA

(b) Normalized stability Parameter vs IBPA

Figure 5.8: STCF11 OPC1: Aerodynamig damping stability curve validation

FINSUP solver and the obtained result follow almost the same rate of change except at an IBPA equal to 36°, 306°, 324° and 342°. Patil et al. shows an unstable region at 288 ° whereas FINE™/Turbo at 324° and 342°. The last three IBPAs from Patil suggest that there is a minima between 270° and 360° but it is not known if the minima corresponds to 288° as no further IBPAs were analyzed. The reference Ξ from Bölcs contains a difference of 23% depending on the solver used as shown in Table 5.5. In this table, FINSUP solver provided the most optimistic results whereas the viscous non-linear solver provided the most conservative. Additionally, as the experimental data is reliable at specific regions, these local values are the main reference rather than the specific value of the stability parameter. From the shown results it is assumed that the system is indeed unstable but further numerical data is required to determine if the trend shown by the current results and by Patil et al. are displaying a true condition.

Figure 5.9, and 5.10 display comparison of the most stable and least stable conditions, $\sigma = 126°$, and $\sigma = 324°$, respectively. Both figures compare the pressure and suction sides distribution of the pressure coefficient of the phase of the first harmonic pressure. The former figure has a low amplitude trend as most of the blade both suction and pressure sides contain a low amplitude. It is only the suction side at $\sigma = 126°$ that has a localized amplitude at the leading edge. This figure provides a misleading intuition that as the magnitudes of the least stable case are much more smaller it should not have encounter flutter. But as mentioned before, the phase is the key parameter to determine whether or not flutter is onset. In both figures along the chord a *wave* trend is found, which is due to the harmonic displacement in the mesh also has this wave behavior. This occurs as the harmonic displacement recovered by the interpolation of the modal file into the CFD mesh produces such waves, as shown in Appendix B.

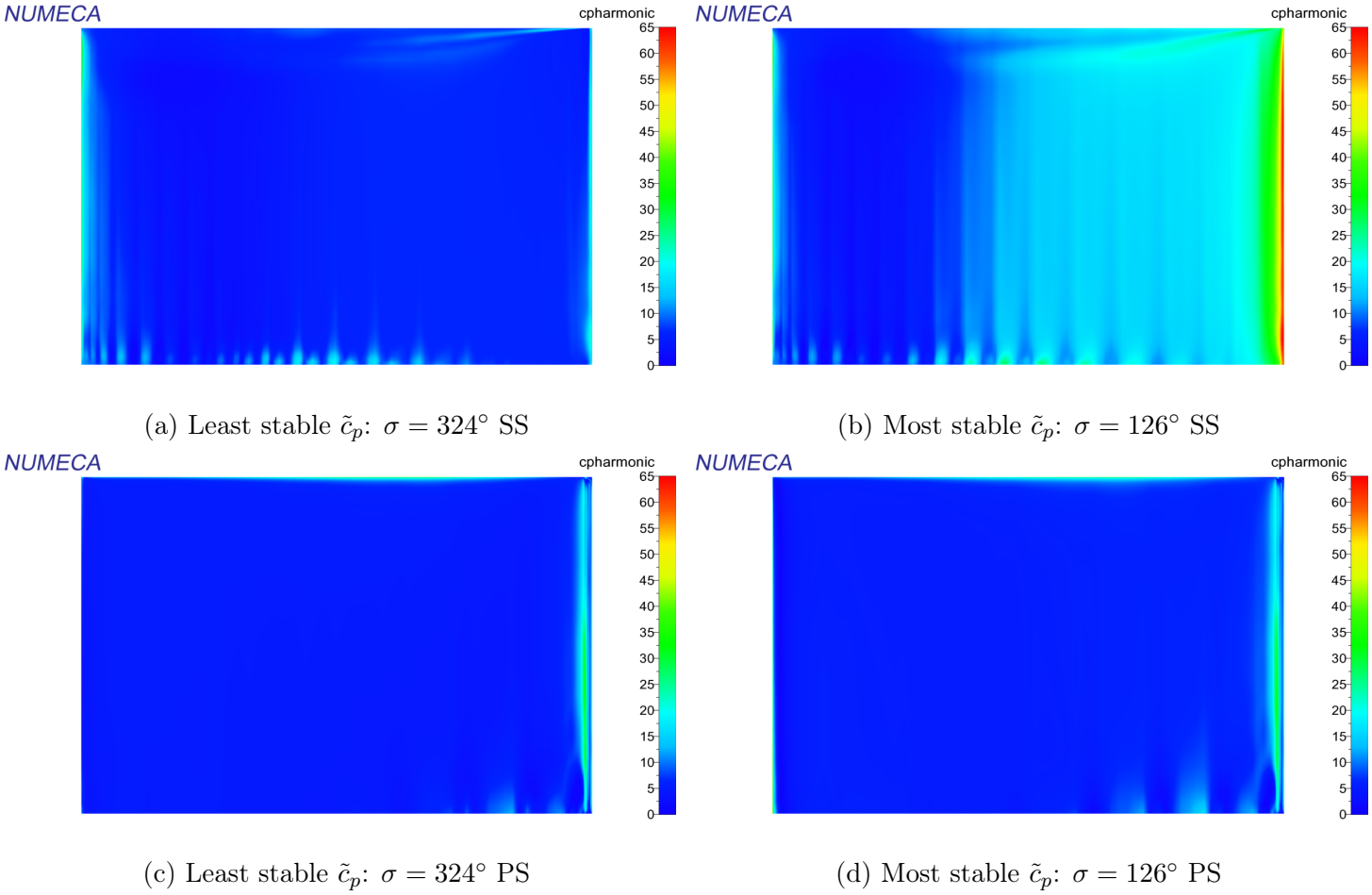

(a) Least stable $\tilde{c}_p$: $\sigma = 324°$ SS

(b) Most stable $\tilde{c}_p$: $\sigma = 126°$ SS

(c) Least stable $\tilde{c}_p$: $\sigma = 324°$ PS

(d) Most stable $\tilde{c}_p$: $\sigma = 126°$ PS

Figure 5.9: STCF11 OPC1: $\tilde{c}_p$ distribution at SS and PS for the least and most stable σ

Figure 5.10 shows the clear variation of phase for the two selected cases at both pressure and suction sides. The pressure side in both cases has an in-phase condition at a small phase angle with a small gradient at the leading edge. In contrast, the suction side is shown to be the root cause of flutter onset. The unstable condition shows that most of all the suction side is in phase with the motion with the highest phase close to the trailing edge. In contrast, the stable condition shows the opposite trend, where almost all the surface is highly out of phase of the motion except from a region close to the trailing edge. Therefore at the most unstable condition, the low amplitude of the pressure coefficient in the suction side is producing an unstable condition as most of the force is in-phase, generating a positive work. In both cases the trailing edge at the suction side has a highly in-phase condition. This location is dominated by the wake potential effect and its corresponding trailing edge vortexes as shown in Figure 5.4. In both cases the PS contains a lower phase; at this region, the Mach gradients normal to the blade surface are much smaller compared to the suction side. It is assumed that, as the motion is perpendicular to the blade movement, there is an induced velocity in the same direction. It would have a higher perturbation in regions with small velocities such as at the wake. Additionally, the contraction and expansion of the channel as a function of σ appears to generate either an stable or unstable effect, with a localized effect at the trailing edge. As in this case only a backward traveling wave (BTW), produces decrease in the aerodynamic power. Additionally, it was found from the steady state solution that, the regions with low static pressure contains the highest harmonic pressure coefficient, besides the wake. This occurs at the leading and trailing edges, also at the blade tip due to the tip leakage. These regions are assumed to be highly sensitive as the harmonic component of the unsteady pressure can have a similar magnitude as the static pressure, whereas in high

pressure regions the harmonic unsteady pressure effect is minimized. Finally, there is a pulsating trend from hub to shroud in the harmonic phase and pressure coefficients. This, is due to the interpolation of the specified physical displacement into the CFD mesh but this effect did not show any significant difference in the results from sub figures 5.6b and 5.6a, so it is assumed that it has a negligible effect.

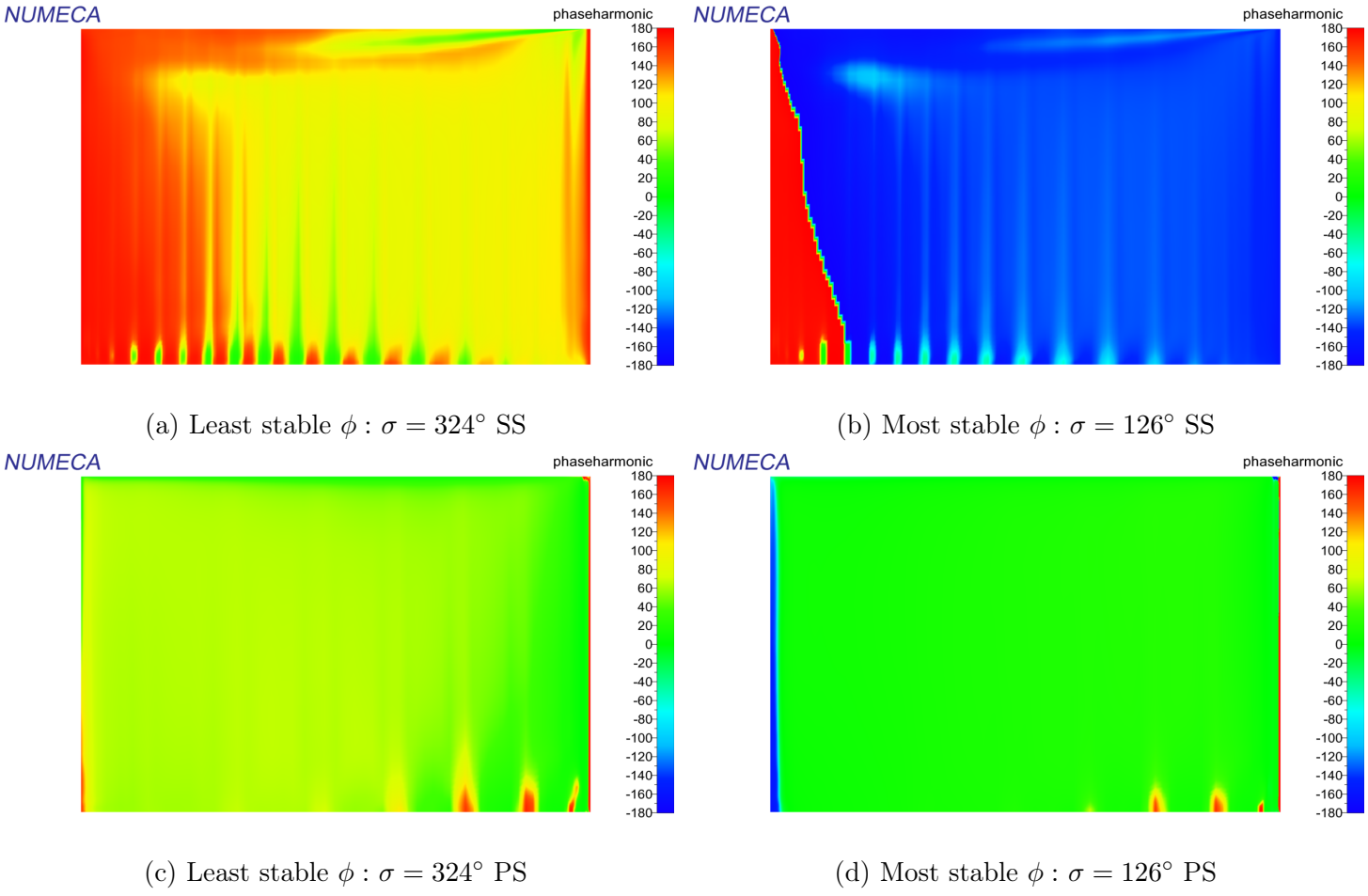

(a) Least stable $\phi : \sigma = 324°$ SS

(b) Most stable $\phi : \sigma = 126°$ SS

(c) Least stable $\phi : \sigma = 324°$ PS

(d) Most stable $\phi : \sigma = 126°$ PS

Figure 5.10: STCF11 OPC1: ϕ distribution at SS and PS for the least and most stable $IBPA$

Finally, Figure 5.11 compares the experimental results from the least stable conditions against the numerical results in terms of $\tilde{c}_p$ and ϕ. Sub figure 5.11a displays the phase. Both experimental and numerical predict an in-phase condition all along the chord. In this figure there is a better agreement at the SS whereas the highest differences are at the PS. Additionally, the peaks in phase are captured at the leading edge of the suction side and towards the trailing edge of the same side. The numerical results from the PS, are conservative in magnitude but show a decrease as moving towards the trailing edge and an recover peak in-phase. The numerical result proves to be in alignment of the phase sign but not with the magnitudes. On the other hand, sub figure 5.11b displays the $\tilde{c}_p$ variation. There is a better agreement with the experimental results in both suction and pressure sides. The available experimental data is up to 75% of the chord. The general trend of this subplot reassembles the one found at 180 ° but with a high decrease in amplitude at the first quarter of the SS. Numerical results match the experimental data along the PS and small variations are found at the SS at 12% and 55%. In general terms, the pressure coefficient matches, and the phase is under predicted by the numerical results but all along the blade are in-phase. There is no further documentation of experimental data at different blade heights to determine if

the unstable trend was captured. However as this location is highly unstable, it is assumed that the blade is producing an unstable condition based on the experimental data. When reproducing the dot product of the harmonic pressure coefficient and the phase indeed a negative value is found, which means a flutter condition. Thus, this behavior matches the prediction of instability at $\sigma = 324°$ by FINE™/Turbo. This trend might also lead to the validity of the unstable region predicted by Patil et al. at 288 °.

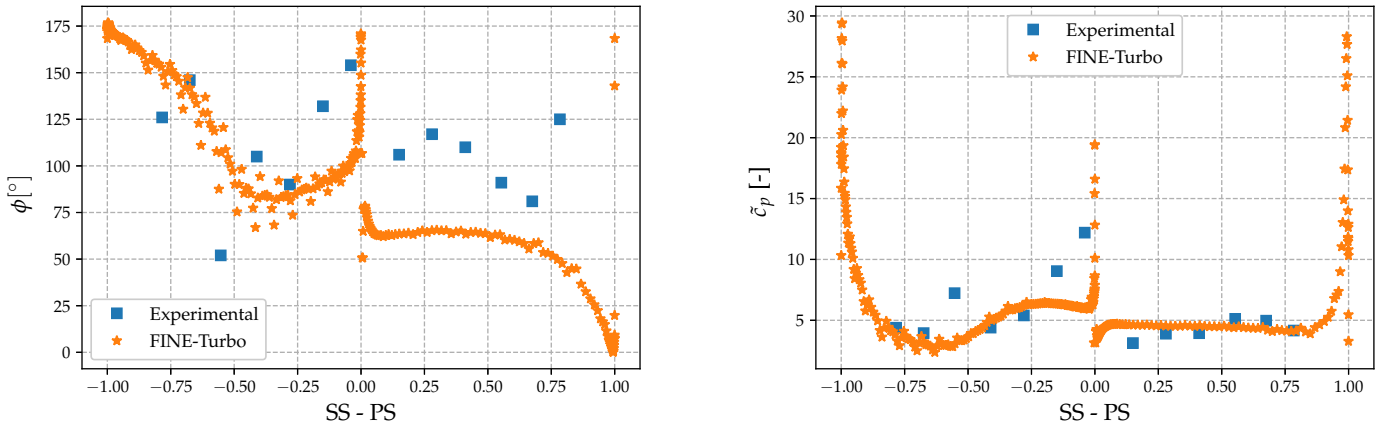

(a) Least stable ϕ: IBPA 324 [°]

(b) Least stable $\tilde{c}_p$: IBPA 324 [°]

Figure 5.11: STCF11 OPC1: Harmonic content at $\sigma = 324$ ° at 50% span

5.1.3 Steady state results: OPC2

In this subsection the second operational condition is analyzed and compared with the experimental data as done for the first operational condition. Nevertheless, in this case the flow physics at the off-design condition is much more complex as strong viscous effects are present. The increase of complexity lies on an appearance of a large laminar separation bubble and shock waves along the suction side. This configuration is also used as reference validation due to its complexity. Figure 5.12 displays the isoentropic Mach number at half of the blade height at off-design conditions. A contrast between experimental data an VOLFAP solver is included. The results along the pressure side are in agreement between the experimental and the two numerical methods. The only significant difference rises at the trailing edge as it is the location of mixing flow from both surfaces. On the other hand, there is a clear difference between the two numerical solutions along the suction side at $18\%c_n$ and from $60\%c_n$ up to the trailing edge. FINE™/Turbo results have a better agreement with the experimental data before 80% of the chord. This region is where the normal shock wave was measured, and the steep local reduction in Mach number is not captured by none of the numerical results. Thus, further references were included in order to determine the reliability of both solutions.

Figure 5.13 shows a contrast with different publications performed by Patil et al. [45], Cinnella et al. [60], and He [62] that compare solutions from Harmonic methods at the same operational condition. In general all of them replicate the same trend as the experiments. The main difference between the current result and the further references occur at $30\%c_n$, as the current results predict a reattachment around $22\%c_n$. Also, no numerical reference is capturing the maximum Mach and its steep decrease, but they have a better agreement with experimental data except at this mentioned location. A further mesh refinement was performed, but no significant change on the reattachment location nor shock were found.

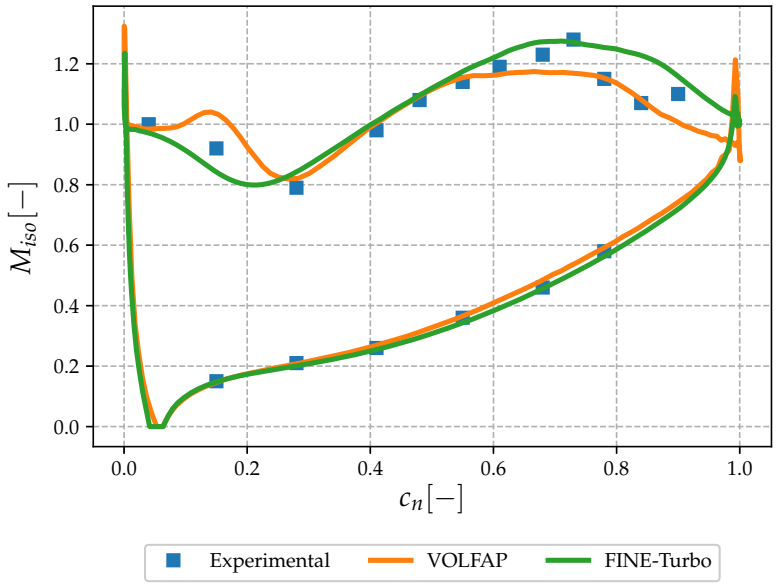

Figure 5.12: STCF11 OPC2: M_{iso} vs c at 50% span validation

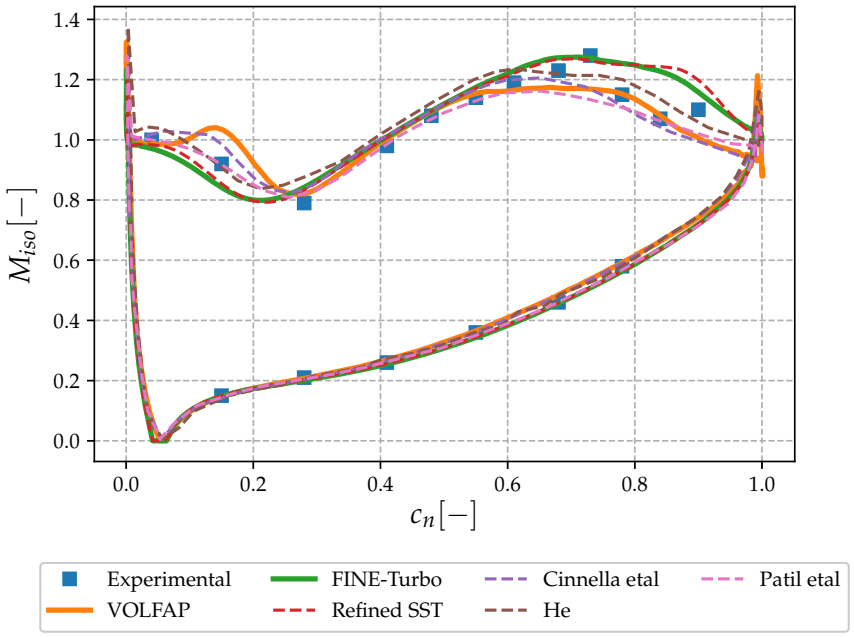

Figure 5.13: STCF11 OPC2: M_{iso} vs c at 50% span comparison

Additionally, it was performed a change in turbulence model to Shear Stress Transport (SST) to capture better the viscous effects but no significant effect was found neither (Dotted red line in Figure 5.13). It is assumed that this difference might be from a different boundary condition at the outlet as is the main driver of the location of the shock wave. The results from this thesis make use of the profile imposed at inlet and outlet which were obtained from [39]. A characteristic of the current results is that its maximum isoentropic Mach matches with the experimental one, being this result the only one capturing this location. Therefore it is assumed that the results are valid to be used as input for the unsteady case.

In order to have a further understanding of the Mach number results, the contour of the absolute Mach number is shown at the same reference blade height in Figure 5.14. The suction side operates at transonic conditions and most of the velocity gradients occur along it. The PS is characterized by the high stagnation region due to the high incidence angle. Sub figure 5.15a shows a zoom region, in which a strong increase in the Mach number at the leading edge of the SS due to a drop in static pressure which is correlated to the separation point. At this region there is a local adverse gradient which causes a laminar separation bubble that is extended around 25% of the chord. After this location, there is a positive pressure gradient again producing a flow acceleration. As it is accelerated the flow gains momentum and reattaches to the suction side. Finally at the trailing edge there are two low momentum vortex due to the wake as highlighted in sub figure 5.15b, which produces a local increase on the static pressure.

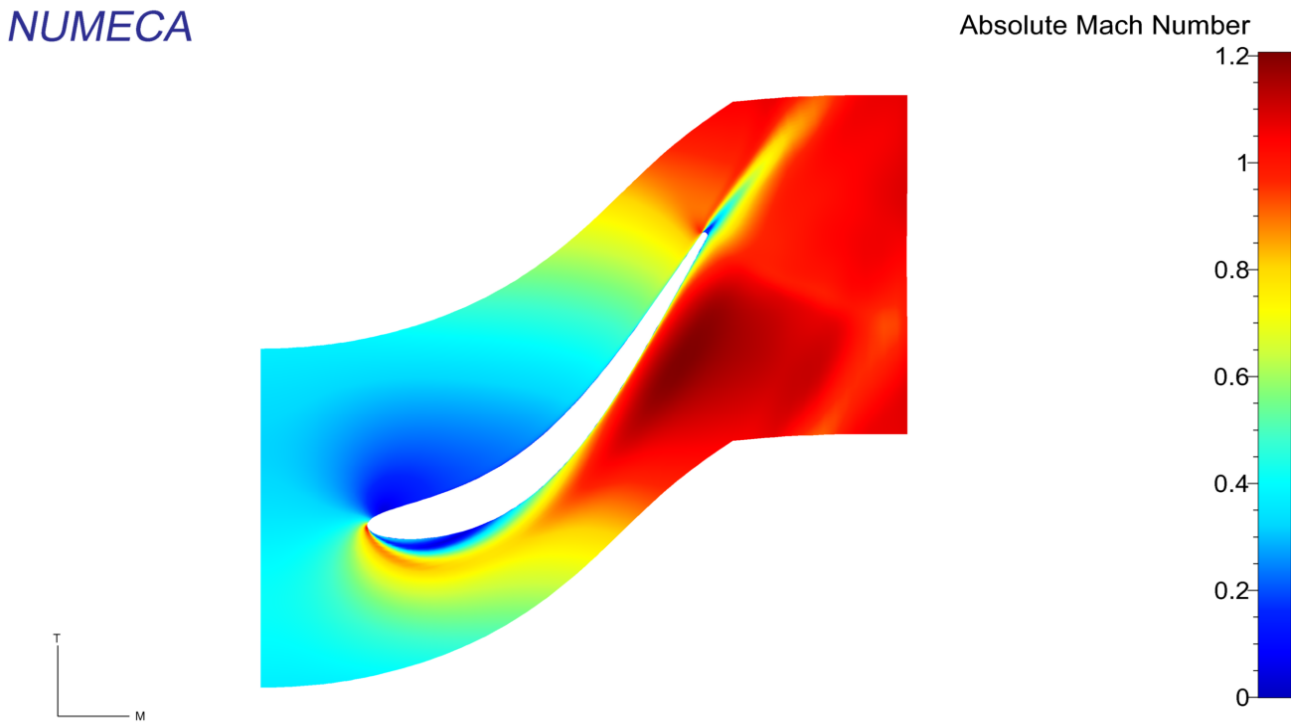

Figure 5.14: STCF11 OPC2: B2B Mach Number view at 50% span

The fluid physics found in Figures 5.14 and 5.15 matches with the one encountered by the reference data from Figure 5.12 in a global trend. In particular, the results from this thesis and the reference data show a shift of around 5% of the chord in the reattachment location. The maximum isoentropic Mach and its location is well captured. However, experimental data shows a much stronger adverse pressure gradient followed by a favorable gradient at 90% of the chord. This trend is not capture by any of the numerical analyses, as it only predicts the effect of a smoother adverse gradient. The main difference between VOLFAP and all other software is that, it predicts the separation bubble but with a faster reattachment location around 5% of the chord. After, another separation is predicted and finally reattaching around 30%. This trend is not capture by the experimental data, but the root cause of this is behavior is unclear as it might be related to the mesh or the boundary conditions as explained before.

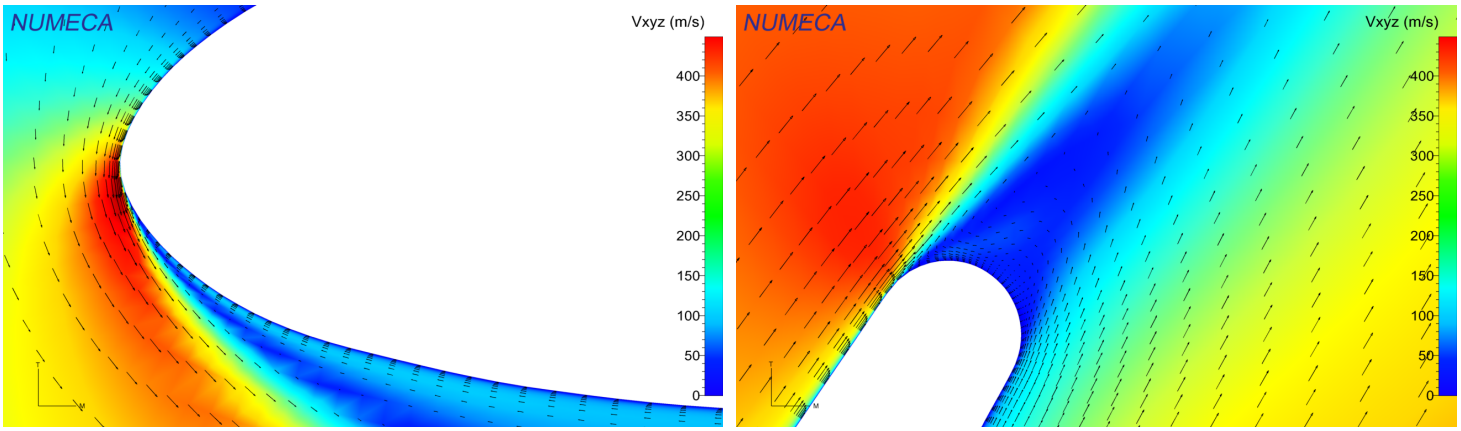

(a) Velocity flow field at LE

(b) Velocity flow field at TE

Figure 5.15: STCF11 OPC2: Absolute velocity field at LE and TE

5.1.4 Unsteady results: OPC2

On a similar basis as in OPC1 in Section 5.1.2, the unsteady analysis of OPC2 was performed by use of the Flutter Wizard tool. The main difference is that the prescribed motion as a function of the span is different. The displacement is recovered by making use of Equation 5.7, but with $(u/c)_{mid} = 0.0035$. Its corresponding generalized displacement is the same as the one found in OPC1 as it has the same physical to imposed displacement ratio. The last difference with respect to OPC1, is that the blade excitation frequency is $f = 212Hz$. The set up time for this case was the same as Section 5.1.2, but at this operational condition the Wizard ran for around 57 hrs with 3 processors. Figure 5.16, shows the result obtained from the output *$\_Aerodamping\_stability.dat$ file of the Wizard with a recovered reference pressure of $P_{ref} = 20.148kPa$. For this condition, the Wizard predicts three unstable conditions on a backward traveling wave at $\sigma = -36\ °, -54\ °\ \& -72\ °$, showing a general instability of the system . Additionally, it predicts two other IBPA values that are close to a flutter region, at $\sigma = 90°\ \&\ 18°$. The maximum condition is found at $\sigma = 126°$.

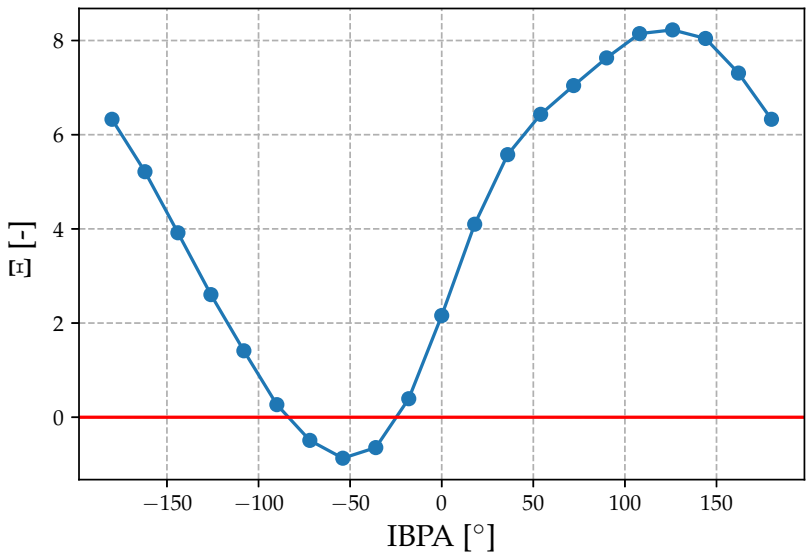

Figure 5.16: STCF11 OPC2: Aerodynamic damping coefficient output from Flutter Wizard tool

A further and detailed analysis is performed manually based on the points of interest from the flutter wizard tool and from the experimental data available. Thus, the first reference IBPA is at $\sigma = 180°$. At this condition the obtain aerodynamic damping coefficient is $\Xi = 6.32$ and its contrast with the references is found in Table 5.6. In this table, it is clear that NOVAK and INST solvers over predict the aerodynamic damping coefficient with respect to the other references. Surprisingly, FINSUP predicts a similar magnitude as all other solvers that include viscous effects (FINE™/Turbo, Cinnella, Patil, VOLFAP). However, this might have been a coincidence as it has been proven that high viscous effects are present in OPC2. The result obtained in this thesis is the most conservative with the lowest prediction, but is in range with the other references with variations up to 29% with respect of VOLFAP.

$\sigma = 180°$	
Software	Ξ
FINSUP	8.4
NOVAK	11.7
INST	11.0
VOLFAP	8.9
FINE™/Turbo	6.32
Cinnella et al.	7.9
Patil et al.	8.4

Table 5.6: STCF11 OPC2: Aerodynamic damping coefficient comparison

In order to determine the root cause of differences found from Table 5.6 a detailed comparison of harmonic content is performed in Figure 5.17. Regarding the phase, sub figure 5.17a shows an underestimation of the phase at the PS but in agreement that this location produces an unstable condition. Towards the trailing edge only Patil et al. is able to capture the in-phase increase. The higher differences rise in the suction side, the first quarter results are congruent for all references. FINE™/Turbo shows a high out of phase until the shock location around 75% where a sudden phase occurs. It is predicted, from all other numerical results, that the shock produces an increase in phase until 180 degrees are achieved, when the phase jump occurs. All numerical results are in disagreement with the experimental results whereas PS shows a good agreement. It is assumed that the main source is in fact the complexity of the shock and that the location of it produces high variation in the static pressure after it. As the experimental data has a confidence level of 95% even for transonic sensitive cases, it is assumed to be the most reliable source and taken as the main reference. This leads that at SS, none of the numerical methods is capturing the physical flow behavior.

Regarding the pressure coefficient, sub figure 5.17b shows a good agreement in the pressure side against the experimental data. However, the current results amplitude of $\tilde{c}_p$ at SS are under predicted by more than a half in the first quarter of the SS. At 75% there is a sudden increase in amplitude, due to the shock, which is clearly captured by VOLFAP and experimental data. The harmonic solutions from He and Patil et al. display a trend of capture the shock but with much lower amplitude as experimental results. FINE™/Turbo does not capture the effect of the shock.

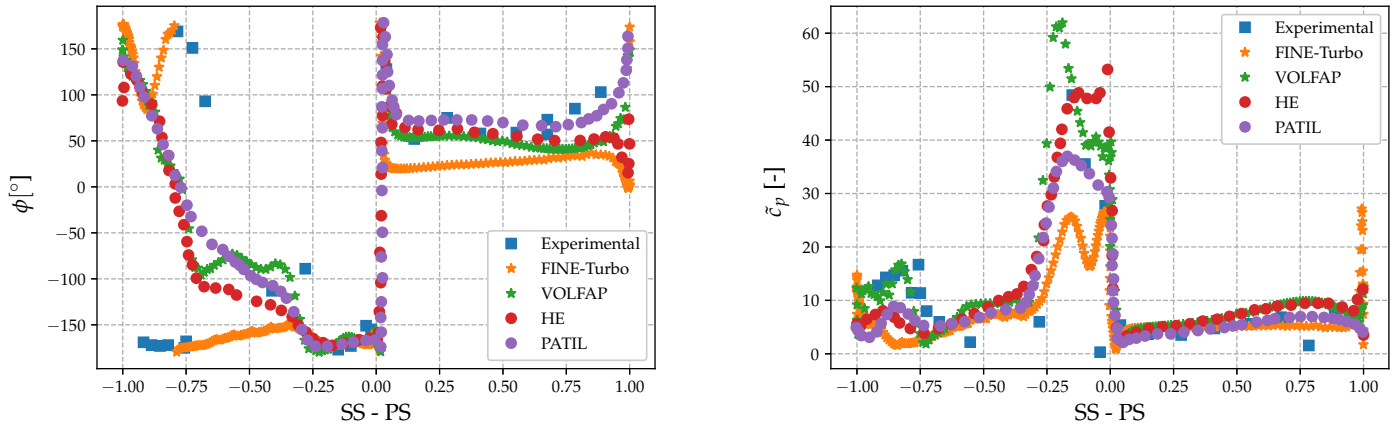

(a) ϕ: $\sigma = 180°$ (b) $\tilde{c}_p$: $\sigma = 180°$

Figure 5.17: STCF11 OPC2: Harmonic content at $\sigma = 180°$ at 50% span

Figure 5.18 displays the comparison of the results obtain by the Flutter Wizards against the multiple references in terms of the aerodynamic damping coefficient. In this figure, the range of IPBAs was re-arranged to match the reference literature. Sub figure 5.18a, displays the general trends of the stability curve for multiple references being compared with the current results. All of them predict a non-flutter free condition on a backward traveling wave except Cinnella et al. The local magnitude of the coefficients vary in some regions by a factor of 2, e.g. $\sigma = 108°$. But at $\sigma = 180°$ there is a relative good agreement between all the results. After normalizing each curve by its own maximum, sub figure 5.18b displays that all the reference have almost the same rate of change up to $\sigma = 100°$ but clear differences are found by Cinnella et al. and Patil et al. starting from $\sigma = 180°$. These differences might be related to the solution from the steady state that is matching in good agreement with the experimental data, and that at the first quarter of the suction side the unsteady pressure coefficient is over predicted providing higher stability.

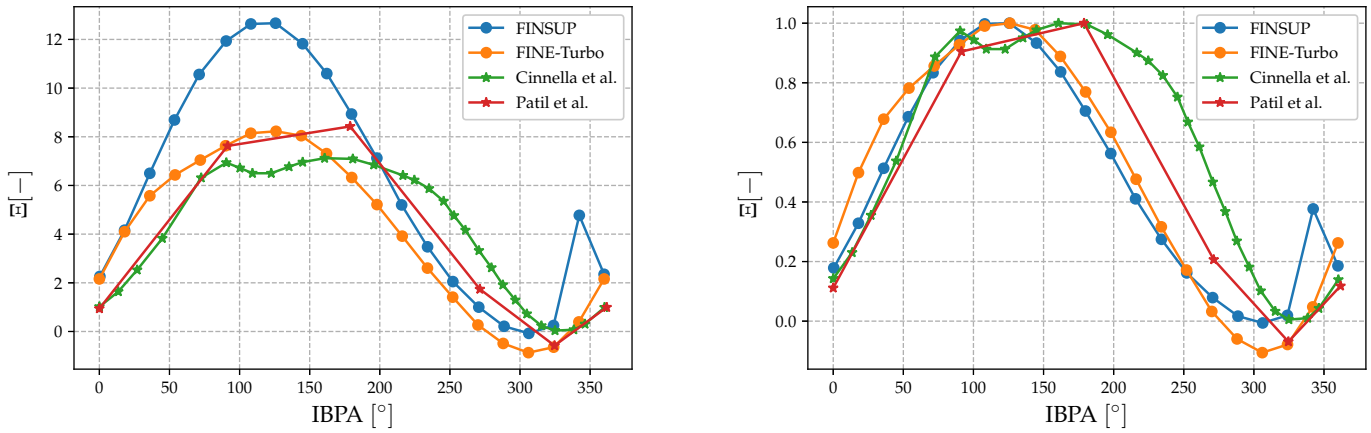

(a) Stability Parameter vs IBPA (b) Normalized stability Parameter vs IBPA

Figure 5.18: STCF11 OPC2: Aerodynamic damping stability curve validation

The experimental data for this operational conditions does not have information of its harmonic content for the least stable conditions ($\sigma = 306°$). Nevertheless, it does provide experimental data for $\sigma = 324°$. Therefore, this updated IBPA will be used as a new reference to compare the numerical results against experimental data, its results are found in Figure 5.19. Sub figure 5.19a shows that the experimental data predicts an almost complete in-phase unsteady pressure at all the chord. The current results are not able to predict the same phase magnitude at the PS but it does predict half of the magnitude with the same trend being in-phase. Regarding the SS, the variations of numerics and experimental results are clear. At the leading edge and at the shock location there is a change in phase, producing a local stable value. Only the last, location is captured after the shock position by the current result.

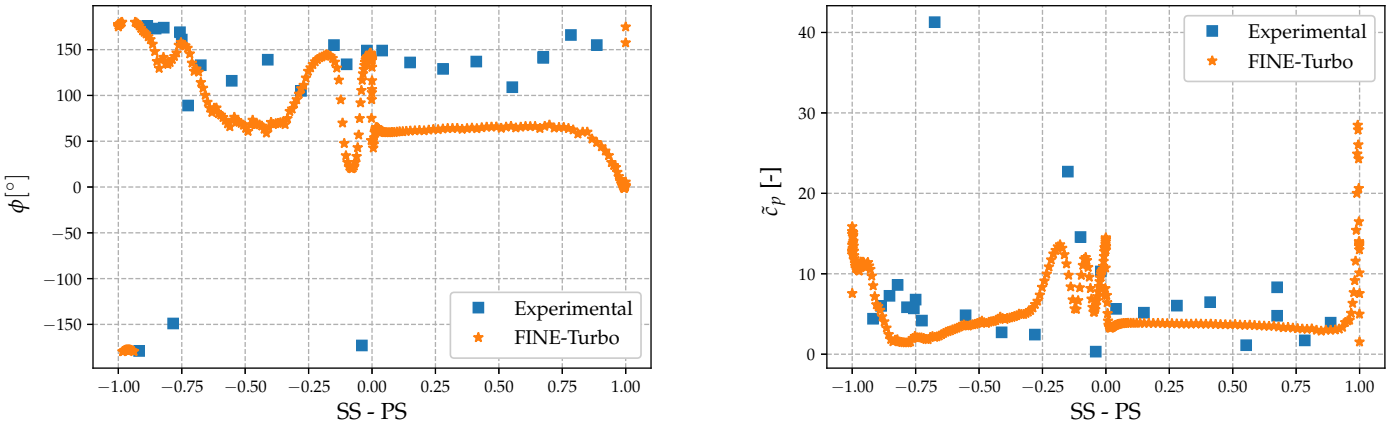

(a) ϕ: $\sigma = 324°$ (b) $\tilde{c}_p$: $\sigma = 324°$

Figure 5.19: STCF11 OPC2: Harmonic content at $\sigma = 324°$ at 50% span, least stable IBPA

Sub figure 5.19b displays the harmonic coefficient variation. The pressure side magnitudes are congruent between numerical and experimental results up to 90% of the chord. At the trailing edge there is a high amplitude prediction, assumed to be caused by the mixing unsteadiness of the wake. Regarding the SS, clear differences are found particularly at 70% of the chord in which a difference of one order of magnitude. At 75% a small peak is obtained experimentally, this sudden change is being captured around 90% of the chord with a lower amplitude. This clear differences are assumed to be caused because the sudden pressure drops at the normal shock wave that are not captured numerically.

Finally, a global understanding of the harmonic content is shown by figure 5.20. The main regions with high pressure coefficient are located at the leading edge and its magnitudes is diffused along the suction side. Regarding the PS, there is a very small harmonic content at the trailing edge. This behavior is assumed to occur at as the incidence angle is high, around 20% of the blade contains a great influence of the stagnation point. Thus the motion of the structure does not have a significant effect on the unsteady field on the PS. The phase along the PS, contains high in-phase magnitudes almost at all the locations of the this blade side. The SS, is as well with high in-phase magnitudes from the leading edge up to 90% of the chord in which a phase shift is found. However on a global perspective the SS is the one with higher contribution in magnitude and in phase, whereas the PS provides a significant contribution due to its phase but not its magnitude. Therefore, flutter is prone to occur at this operational condition proving numerical results are in agreement with the harmonic content of experimental results.

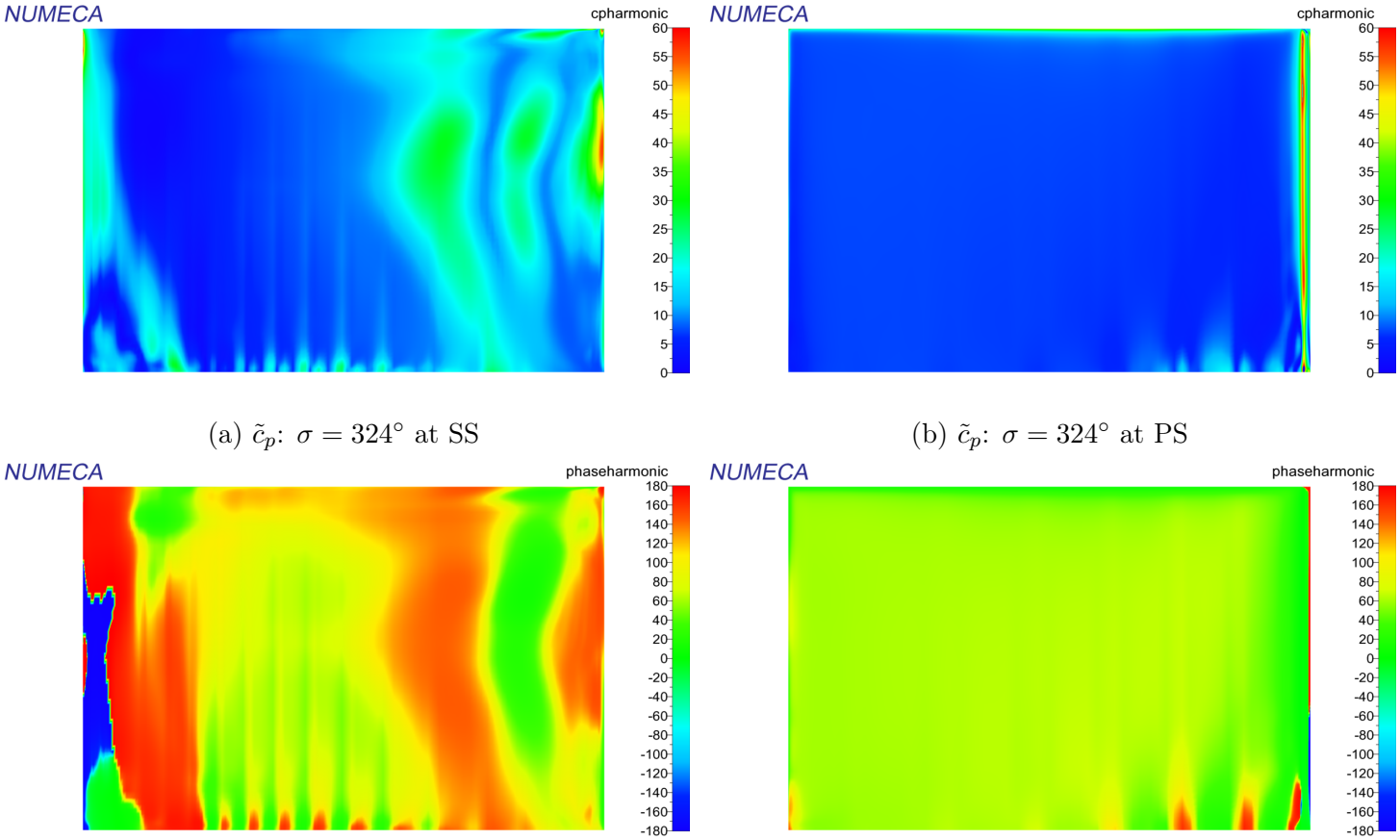

(a) $\tilde{c}_p$: $\sigma = 324°$ at SS

(b) $\tilde{c}_p$: $\sigma = 324°$ at PS

(c) ϕ: $\sigma = 324°$ at SS

(d) ϕ: $\sigma = 324°$ at PS

Figure 5.20: STCF11 OPC2: $\tilde{c}_p$ and ϕ distribution at SS and PS for the least stable case

5.2 Standard Configuration 4

The standard configuration 4 (STCF4) has been widely used in literature by Panovsky and Kielb [21], Waite [24], Cinnella et al. [60], Arnone et al. [65], Hall and Lorence [66]. This configuration corresponds to a high loaded turbine rotor in which the operational conditions are high subsonic. This configuration has 20 thick blades which represent a common cross section of a turbine. The experimental data assessed multiple operation conditions by changing vibration frequency, outlet static pressure, and IBPA. Further details regarding the experimental setup can be found in [57], original paper, and an updated revision in the web site [63], which contains three additional cases. Within this section, four operational points are evaluated, three corresponding to the updated revision and one obtained from the Annex 5 of the original paper, which will be refer only as Annex 5 and shall not be confused with any Annex from this thesis.

Several inconsistencies were found within the updated version in terms of dimensions. The chord does not correspond to the one mentioned in the original version. Additionally, the pitch matches between both references but, by using the web site's specified chord the pitch dimension can not be recovered. Therefore, the final chord length and stagger angles were chosen to be in agreement with the original document [57]. Nevertheless, the updated revision contains three well detailed cases with its corresponding boundary conditions in terms of flow physics and blade vibration. Additionally, this reference contains experimental values of the aerodynamic damping coefficient which is highly valuable as this information is sparse. The

experimental blade vibration was measured at midspan with a bending direction of 60.4° with respect to the true chord axis. Among the three cases, the blade vibration target is not specified but multiple blade amplitude vibrations are provided. From the reported vibration amplitudes of Cases 624, 627, and 628, the mean displacement out of 513 measurement, is 0.295 mm. Thus, the assumed blade vibration amplitude in this thesis corresponds to 0.3 mm at 50% of the blade span. This approached was used as well for the blade vibration of Annex 5, in which the vibration amplitude was of 0.22 mm. These magnitudes of physical displacement were introduced into the input section of the Wizard as a custom option. Additionally, as the mode shape is in fact the imposed motion, the generalized displacement still holds to be 0.5 as in Section 5.1. Table 5.7, provides a summary of the geometric properties of this configuration.

STCF 4	
c [mm]	74.4
γ [°]	56.6
b [mm]	40
upstream plane [m]	$0.09c$
downstream plane [m]	$1.14\ c$
h_{gap} [mm]	0.3
δ [°]	60.4
f $[Hz]$	149, 150 & 152
u $[mm]$	0.3 & 0.22

Table 5.7: STCF4: Geometric properties

The 2D airfoil coordinates were recovered from the updated revisions that can be found in [63]. The 3D blade geometry is the result of staggering the airfoil along its center of gravity (CG). Its corresponding CG was retrieved by the Computer Aided-Design (CAD) software *SIEMENS - NX12.0™* as this location is not specified in any reference literature. Thus, the 2D profile was imported, and an extruded solid perpendicular to the 2D plane was generated in order to obtain the inertial properties of the airfoil. Figure 5.21, displays the center of gravity found by this methodology with a black dot with its corresponding coordinates in mm.

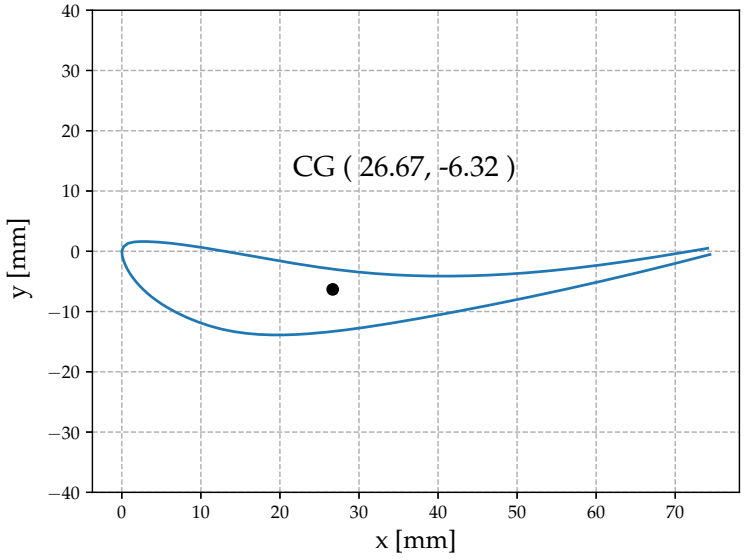

Figure 5.21: STCF4: Airfoil stagger location

The provided airfoil profile has an open trailing edge. The trailing edge can be closed by either a smooth rounded curve or a complete blunt configuration as shown in Figures 5.22. Numerical results were obtained for both cases in order to assess the geometry influence. The rounded configuration has a radius of 0.5 mm, which represents a geometry variation of 0.6% with respect the airfoil chord. It is expected that this geometric change, shall be only affecting regions close to the trailing edge.

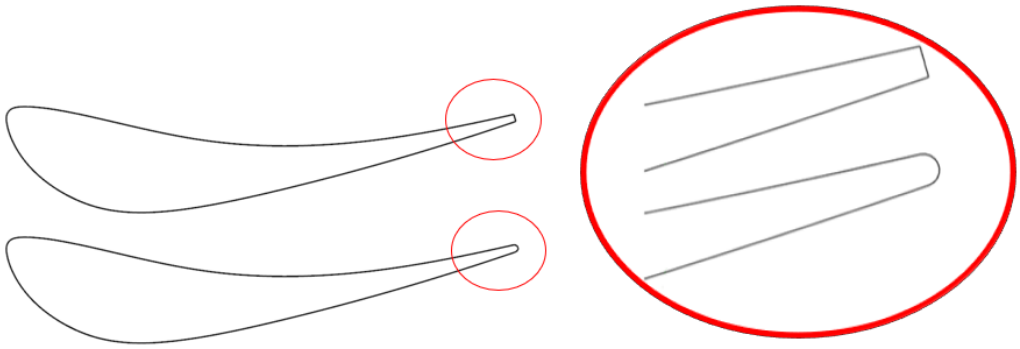

Figure 5.22: STCF4: Blunt and rounded trailing edge geometry

The 3D geometry of the blade was obtained by prescribing the profiles at root and tip into IGG™/AutoGrid5™, which is a structured grid generator module within FINE™/Turbo. Also, the profiles of the hub and shroud are prescribed to generate the passage. After, in Autogrid5™the passage is created on a meridional plane. Figure 5.23 displays the meridional view of the passage with its corresponding dimension upstream and downstream the blade as a function of the real chord.

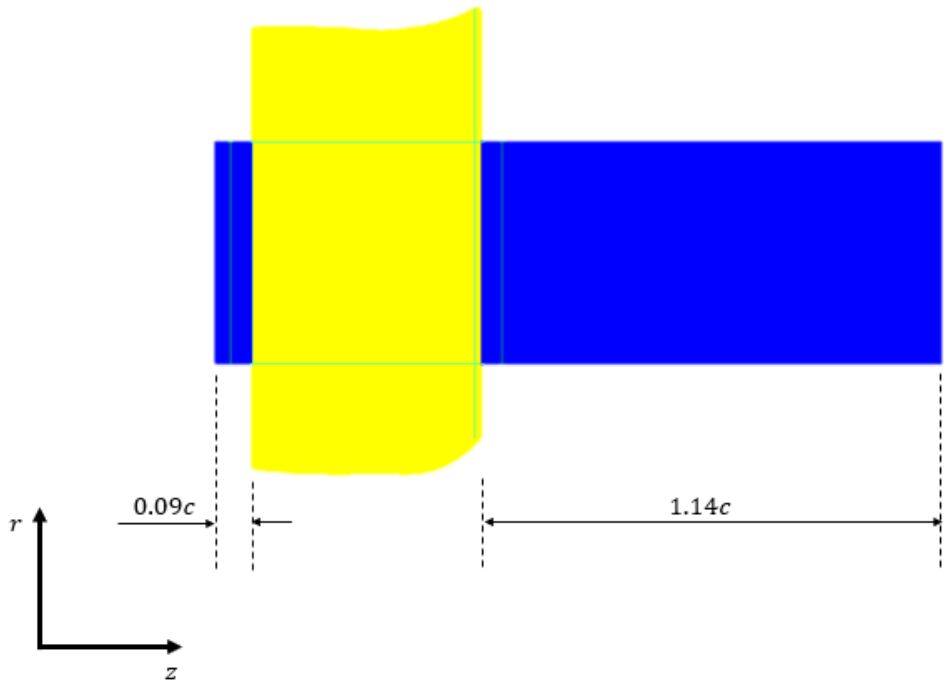

Figure 5.23: STCF4: Meridional view

STCF4 contains three operational conditions: Case 624, Case 627, Case 628. Which corresponds to transonic and supersonic cases, and its operational conditions can be found in Table 5.8. The initialized boundary conditions profiles at the inlet and outlet were used as specified in [63]. The profiles contain information of the fluid flow angle, total pressure at the inlet, and static pressure at the outlet along the span.

	Case 624	**Case 627**	**Case 628**
P_{t_1} [kPa]	199.0	160.9	217.1
P_1 [kPa]	193.2	156.8	211.0
α_1 [°]	-21.4	-15.2	-12.0
$M_{1_{iso}}$ [-]	0.21	0.19	0.2
P_2 [kPa]	100.8	100.7	66.2
$M_{2_{iso}}$ [-]	1.04	0.85	1.42
f $[Hz]$	149	149	152
u $[mm]$	0.3	0.3	0.3

Table 5.8: STCF4: Mean boundary conditions per case

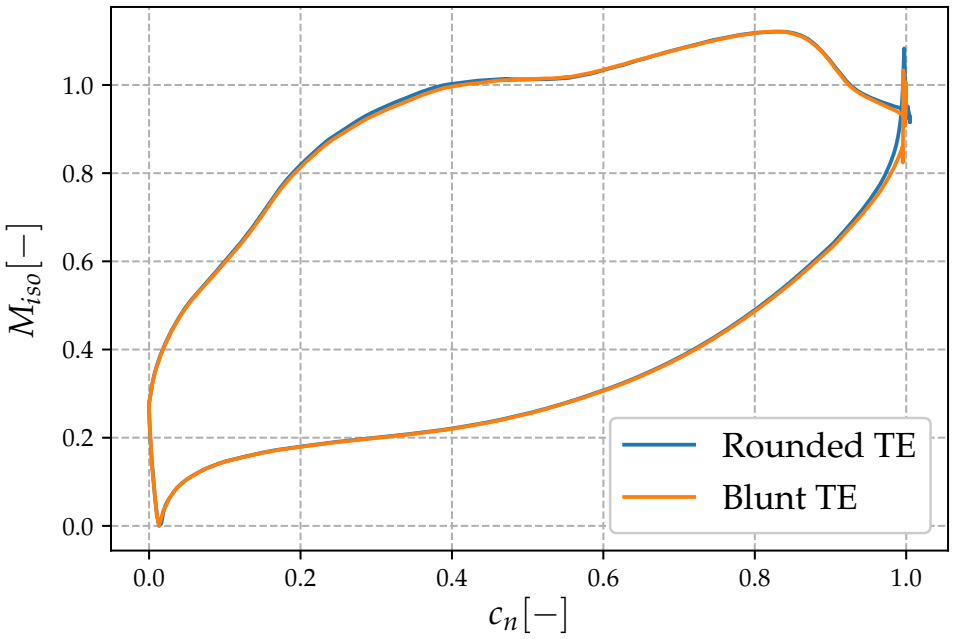

Figure 5.24: STCF4: Blunt vs round TE M_{iso} comparison

Case 624 was selected as the reference case to determine the influence of the trailing edge geometry for the same mesh. Figure 5.24 shows the results from this specific case for both configurations. There are not any significant differences when comparing the isoentropic Mach number at 50% span but at the trailing edge. The differences rise only at around 97% of the chord, which is at close to the trailing edge. The round case predicts a higher variation of pressure gradient, whereas the blunt configuration predicts a smoother mixing region. The physical insight of the difference is found in Figure 5.25. In the blunt case the low momentum vortex is shifted slightly towards the SS region, the flow at the PS has enough

momentum to recapture the flow allowing less pressure gradients. On the other hand the rounded case, produces two vortex at the wake, leading to a higher pressure gradient. The two vortex are located within the highlighted regions. It is clear that the vortex of the round tip at the PS has a higher influence in the flow field with respect to the blunt case. However, the round geometry does not have a critical effect. Thus, the rounded geometry was chosen, as it will provide a further control for the blade vibration in the unsteady case, as shown in subsection 5.2.2.

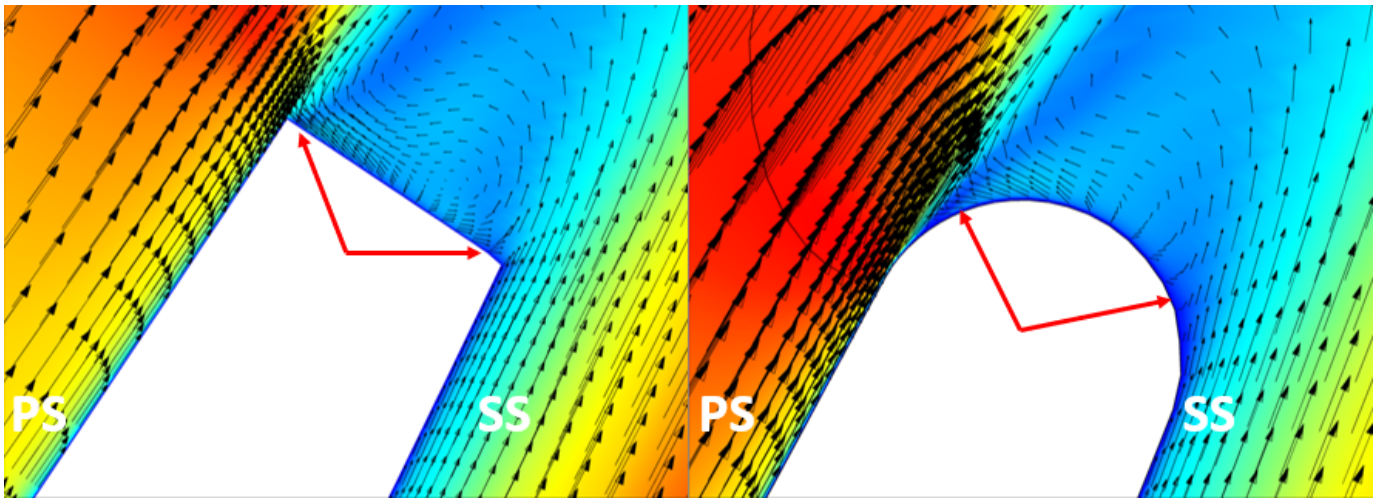

Figure 5.25: STCF4: Velocity field differences from blunt and round TE

5.2.1 Mesh independence

A mesh independence study was performed on case 624. Three meshes were generated, with the difference in y^+ and span wise points leading to a coarse, medium and fine meshes. Characteristics of each mesh and its machine physical properties outputs are shown in Table 5.9. The differences between Mesh 2 and Mesh 3 in terms of efficiency, torque, trust, mass flow and pressure ratio are from the order of 0.5%.

	Mesh 1 Coarse	Mesh 2 Medium	Mesh 3 Fine
Number of points [1E6]	≈ 0.65	≈ 1.6	≈ 2.2
y^+	7	1	0.5
Span wise points	53	89	121
Efficiency[%]	89.74	85.7	85.29
Torque $[N \cdot m]$	307.6	305.6	305
Thrust $[N]$	3917	3895	3898
Mass flow $[kg/s]$	6.387	6.372	6.352
Pressure ratio [-]	0.9496	0.9297	0.9277

Table 5.9: STCF4: Mesh independence results

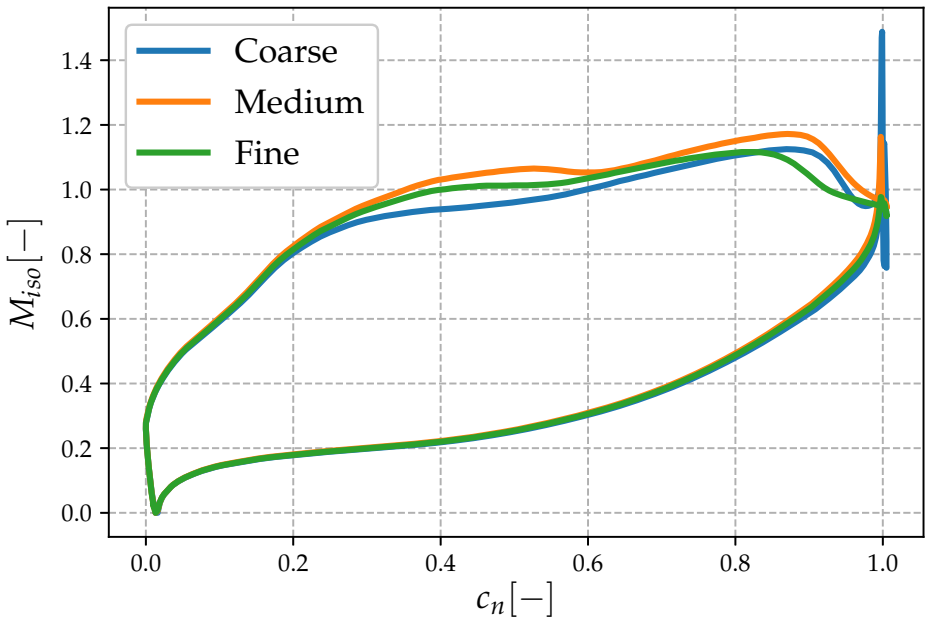

Figure 5.26: STCF4: Mesh independence of M_{iso} vs c at 50% span

A further comparison from these three meshes is performed by contrasting the isoentropic Mach number (M_{iso}) at 50% span, shown in Figure 5.26. No difference is found at the pressure side but at the suction side and trailing edge regions. Both coarse and medium meshes predict the maximum Mach around 90% of the span whereas the fine mesh predicts it before. Clear differences are also found at 40% of the chord where there is a variation of 0.1 Mach. Finally, the highest difference is at the trailing edge, with a variation up to 0.4 Mach. The higher the refinement of the blade, a better capture of the trailing edge. This region is important as it is expected that a high unsteady pressure influence might take place.

It has been proven that the differences in the physical properties of the machine, e.g. Pressure ratio, are negligible between medium and fine mesh. The effect of the wake on the trailing edge is captured in further detailed with a finer mesh. Due to slight variations in the isoentropic Mach, the results between medium and fine meshes were compared against the experimental reference data. It was found that the fine case, was able to reproduce in better agreement the experimental results (Section 5.2.2). Therefore, the fine mesh is taken as reference of mesh independent results.

5.2.2 Case 624

Steady state results: Case 624

This configuration corresponds to a transonic case with a designed isoentropic Mach outlet of 1.04. The main characteristic of this configuration is that the incident angle is high ($\alpha_1 = -21.4°$) but it does not produce any flow separation at the leading edge along the suction side. Figure 5.27 contrasts experimental and numerical results. A general good agreement between results is found, in both pressure and suction side.

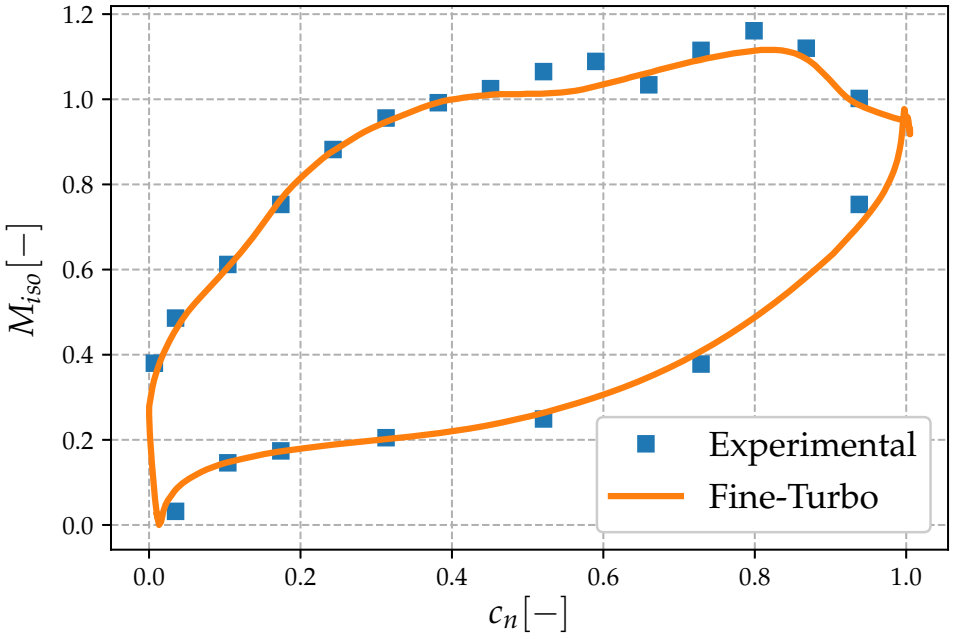

Figure 5.27: STCF4 case 624: M_{iso} vs c at 50% span validation

Along the suction side the flow turns supersonic and leaves the trailing edge at subsonic conditions producing a normal shock wave. Experimental results at SS, predict an isoentropic Mach number drop at around 65% of the chord. This, indicates a local adverse pressure gradient that is not captured by the numerical result. The experimental trend shows that after this region there is an increase of the Mach number until the normal shock wave takes place. This transition, might be that during the experiments at 65% of the chord a local normal shock wave was found that caused a Mach variation. The numerical location of the maximum Mach number is in agreement with the experiments (80% chord). After this region the flow becomes subsonic towards the trailing edge.

Figure 5.28, displays a blade to blade view of the absolute Mach number at 50% of the span. The SS shows a gradual increase of the Mach number, from a region close to a stagnation point at the leading edge to a supersonic condition towards the trailing edge. A normal shock wave is present close to the trailing edge along the suction side. The wake seems to have a localized region in which is highly present with a smoother dissipation in comparison with STCF11 cases. Additionally, due to the high stagger angle, the wake of the surrounding blades have a clear effect downstream. Downstream the passage, the effect up to the second neighbor blade is present.

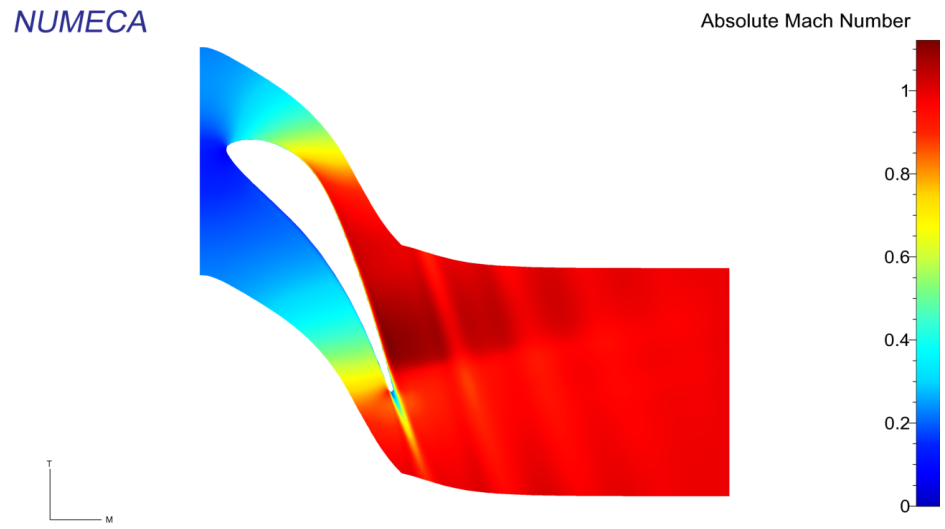

Figure 5.28: STCF4 case 624: B2B Mach number view at 50% span

Unsteady results: Case 624

For this case, the reference pressure recovered by the wizard from the steady state solution is $P_{ref} = 5606\ Pa$, the recovered blade vibration is $f = 149\ Hz$, with a physical displacement of 0.3 mm. The wizard ran in B case because the hub had an imposed displacement. All the possible IBPA variations were set up in less than a minute and the full stability was obtained after $\approx$ 95 hrs with 3 processors. Figure 5.29 shows the reconstructed aerodynamic damping coefficient from the wizard's output. In this figure, seven unsteady cases are found, all of them in a backward traveling wave. The least and most stable cases are found at $\sigma = -72°$ & $72°$, respectively. Thus, the main outcome from the flutter wizard is that the system is unstable.

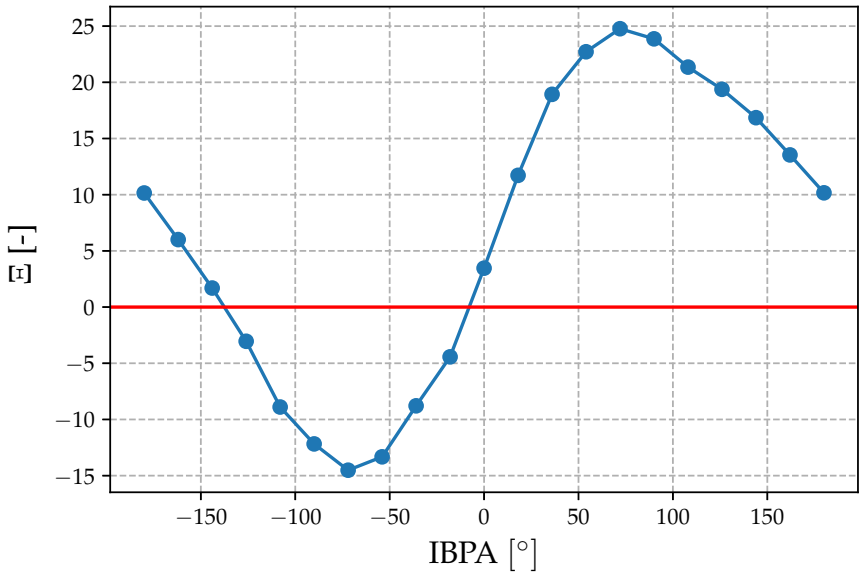

Figure 5.29: STCF4 case 624: Aerodynamic damping coefficient output from Flutter Wizard tool

On a similar basis as in Section 5.1, the first reference case to be compared manually is at $\sigma = 180°$, followed by its least and most stable IBPAs. For the first case, the aerodynamic damping coefficient is $\Xi = 10.16$ and the experimental is $\Xi_{exp} = 3.4$. There is a clear difference between the two values but this variation in magnitudes could be associated to the scaling factor used, and the integration method from experimental data which was proved by Fransson [39] to be highly sensitive to the harmonic content. Nevertheless, both of them predict an stable condition, which indicates a qualitative agreement of results. As the experimental aerodynamic damping coefficient is different in magnitude to the obtained, the harmonic content is contrasted manually for a deeper analysis. Figure 5.30, displays the difference of experimental and numerical results for the harmonic content in terms of phase and pressure coefficient at 50% span at $\sigma = 180°$. Regarding the phase, there are differences mostly at the PS in magnitude but both results predict an unstable effect. At SS, the experimental data predicts a change of phase in a clockwise direction whereas numerical results are anti-clockwise, but the in-phase and out of phase angle magnitudes match between both results, except on the transition region. Regarding the harmonic pressure coefficient, most of the harmonic amplitude is captured at the first quarter of SS with a good overall correlation between experimental and numerical data at SS and PS. At this figure a peak in amplitude is found at the trailing edge in both blade sides, as there is no reference data close to the TE, it is uncertain to determine if this is a numerical or physical effect. However this could also be related to the fact that the wake harmonic content and that the mesh elements move within this regions going from different pressure gradients.

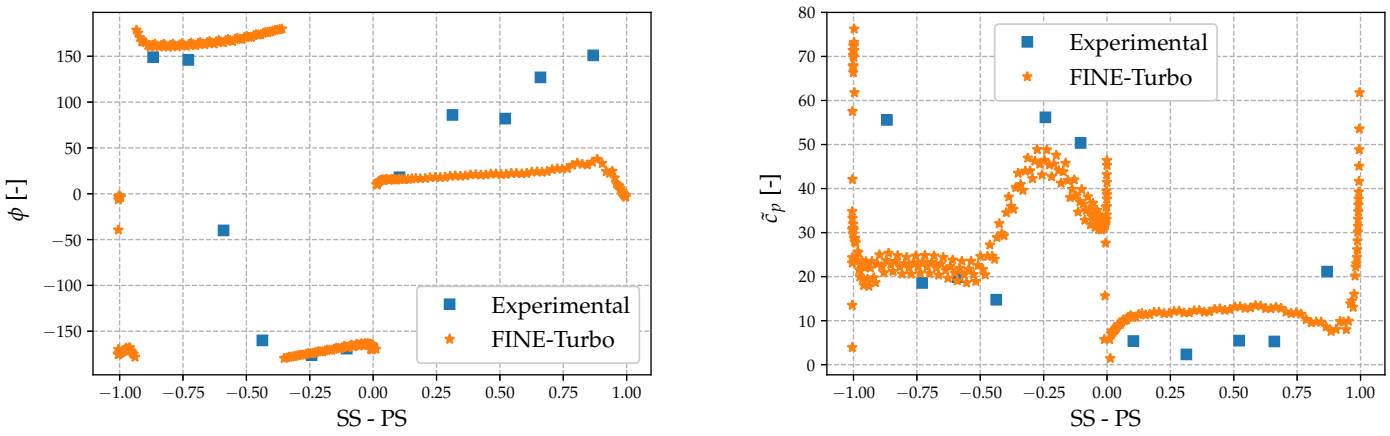

(a) ϕ: $\sigma = 180°$

(b) $\tilde{c}_p$: $\sigma = 180°$

Figure 5.30: STCF4 case 624: Harmonic content at $\sigma = 180°$ at 50% span

Figure 5.31, contrast the experimental and the wizard output of the aerodynamic damping coefficient against all IBPAs, reproducing the forward and backward traveling wave. One particular characteristic from the experimental results are the sudden jumps of the stability parameter. Thus, $\sigma = 36°$ & $72°$ have a high stable magnitudes whereas its neighbors are unstable. The coefficient variation is attributed to the sensitivity of magnitudes of $\tilde{c}_p$, along with the fact that the shock position fluctuations are not purely harmonic, however its clear source is unknown. Numerical results do not predict any jump in the aerodynamic coefficient and also show an unstable region from $\sigma = -126°$ to $-18°$ where as experimental are extended from $\sigma = -144°$ to $0°$. The magnitudes of the aerodynamic damping coefficient are highly different on a forward traveling wave with regions up to seven times the experimental value.

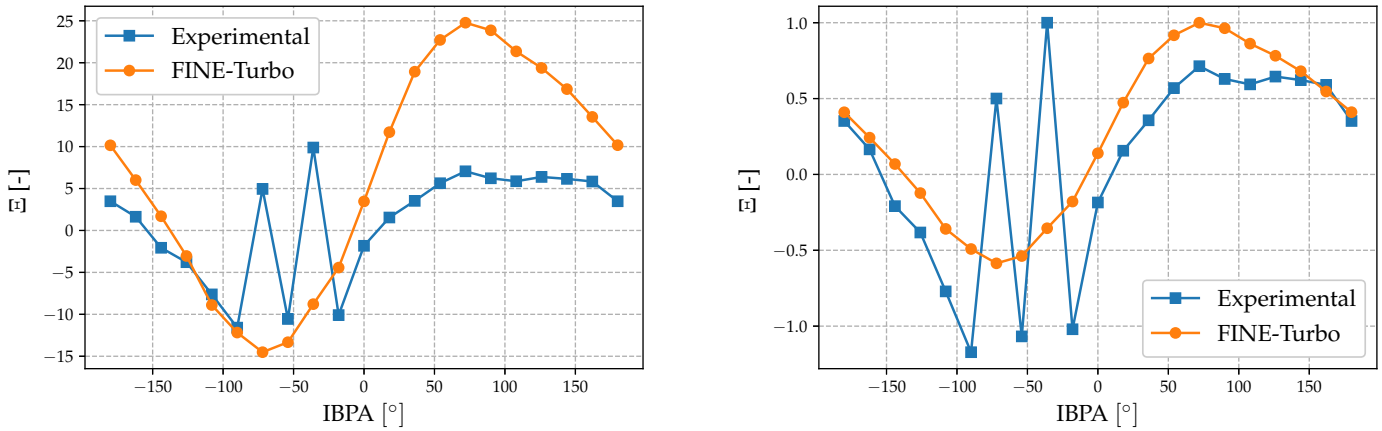

(a) Ξ vs IBPA

(b) Normalized Ξ vs IBPA

Figure 5.31: STCF4 case 624: Aerodynamic damping stability curve validation

The proportional aerodynamic power ratio between experiments and numerical results is shown in sub Figure 5.31b. At regions with high IBPA the results have the same ratio, but along the BTW the differences increase considerably towards the least stable condition, this trend is also found on the FTW but with a lower difference. It appears that the more blades have a different phase position, the greater the difference. Numerically, the least and most stable conditions are found at $\sigma = -72°$ & $\sigma = 72°$. Experimentally, the prediction is at $\sigma = -90°$ & $\sigma = -36°$, providing a great disagreement on the most stable case. However, if the harmonic trend would be recovered, specially on the BTW the values would be updated to $\sigma = -90°$ & $\sigma = 72°$, which is a better agreement between results. As these two locations provide the maximum an minimum, these will be assessed within its harmonic content. Figure 5.32 shows the contrast between the numerical and experimental results for the least and most stable conditions at 50% of the blade height.

Sub figures 5.32a & 5.32c display the phase of the least and most stable condition, respectively. On a global scale, the PS for both conditions predicts an almost constant value and slowly increases to its opposite initial phase condition. The suction side is, in both cases, the region that contributes in higher magnitude with the stability or instability of the system. The least stable condition has a better agreement with experimental data, whereas the most stable case has a difference in phase direction towards the trailing edge. Similarly, sub Figures 5.32b & 5.32d, display the harmonic pressure coefficients for the least and most stable conditions. It is clear that in general, there is a good agreement along the PS, with slight differences between both cases. Along the SS, a good agreement happens up to $\approx 30\%$ of the chord. The highest differences occur after this region, where multiple jumps in amplitudes are predicted experimentally. The highest jump is located towards the trailing edge in both cases, which is shifted from numerical to experimental results. It is assumed that this last shift is due to the difference in shock wave location predicted from steady state results. Additionally, the amplitude varies in its distribution but not in its total magnitude, therefore the main key driver player is the phase variation.

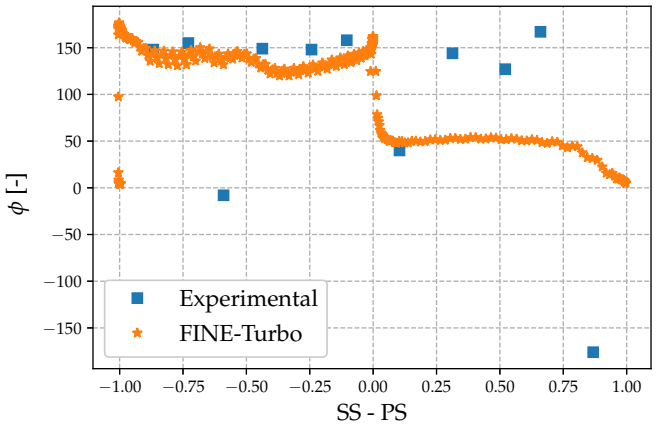

(a) Least stable: ϕ at $\sigma = -90°$

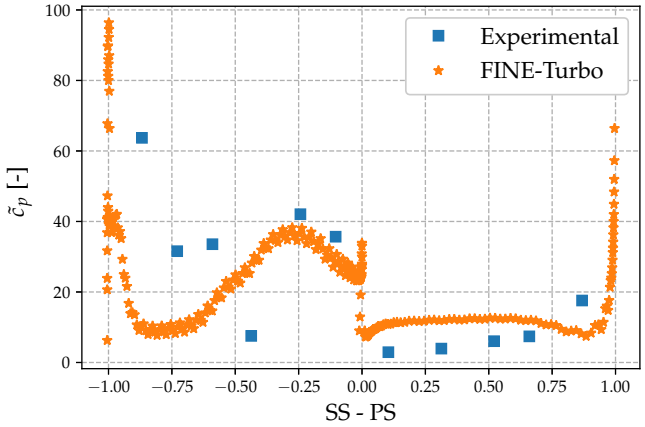

(b) Least stable: $\tilde{c}_p$ at $\sigma = -90°$

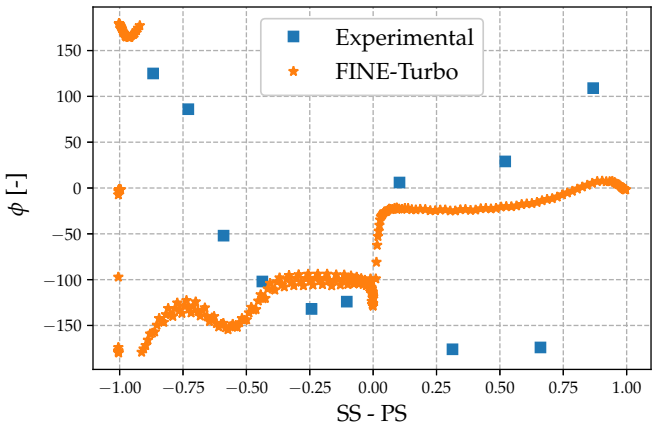

(c) Most stable: ϕ at $\sigma = 72°$

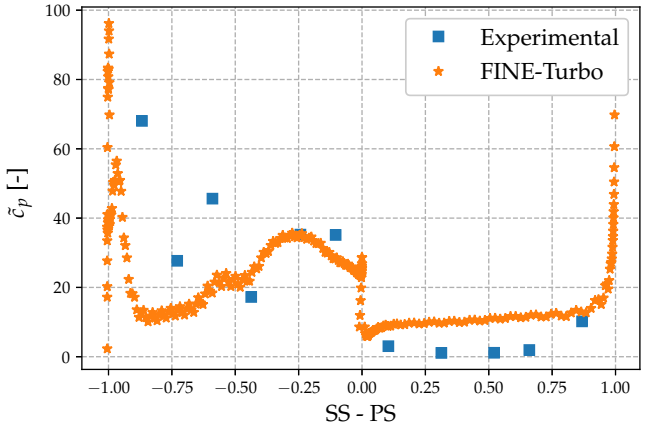

(d) Most stable: $\tilde{c}_p$ at $\sigma = 72°$

Figure 5.32: STCF4 case 624: Harmonic content at most and least stable at 50% span

For this case, in general the aerodynamic damping coefficient varies as approaching to an in phase blade motion, specially at the forward traveling wave. The proportional aerodynamic power shows that the higher differences rise at a backward traveling wave. The least and most stable IBPAs are in agreement between results only when the experimental results are treated as being a continuous function. The variation of aerodynamic damping coefficient might have been due to the finite number of pressure sensors over the blade, and or a different reference pressure. It is unclear the root cause of these variations in aerodynamic damping coefficient. The suction side is the region which produces the highest instability information in phase and in pressure coefficient amplitude. Along the PS, it has been found that the increase in phase correlates where the Isotropic Mach number starts to increase rapidly $\approx 50\%$, around this region a quick increase in phase was observed for least and the reference IBPA configuration. Regarding the harmonic pressure coefficient, there are slight variations in magnitude when compared to experimental data, most of the harmonic content is encountered at the suction side around 60% of the chord. The reference IBPA and the most unstable conditions predict an agreement between numerical and experimental data, but not for the most stable condition.

5.2.3 Case 627

Steady state results: Case 627

The following case, corresponds to a design condition of an isoentropic Mach of 0.9 with smoother incidence angle as the in Subsection 5.2.2. Figure 5.33 displays the variation of the isoentropic Mach number at 50% of the span. The numerical data correlates closely to the reference experimental values. Around 60% of the pressure side presents a low Mach number, $M \leq 0.3$, and a high acceleration rate after this location. Along the suction side, around 50% of the blade has an almost constant Mach number of ≈0.85, and this region is extended from 30%c_n to 80%c_n. This almost constant flow field, produce a smooth mixing between PS and SS, leading to a gentle wake. Neighboring blades will have a lower wake effect downstream the main passage compared to Section 5.2.2.

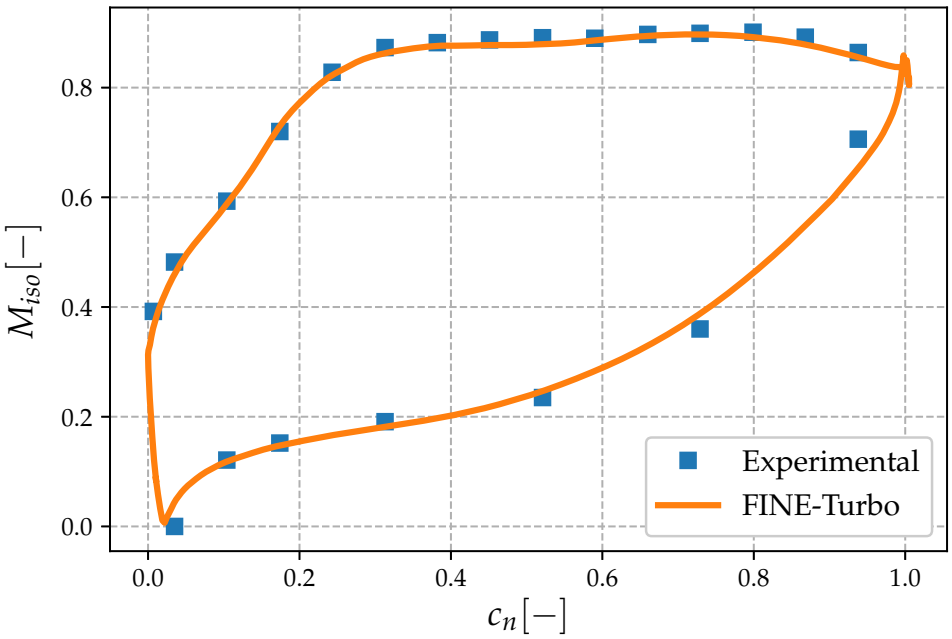

Figure 5.33: STCF4 case 627: M_{iso} vs c at 50% span validation

Figure 5.34 shows the Mach number contour at 50% of the span. In this figure, it is shown in higher detail that the wake is localized and it does not produce a high perturbation of the surrounding flow, producing a faster wake diffusion downstream, compared to subsection 5.2.2, and 5.1. Additionally, it shows an almost constant velocity field along the suction side. This region is expected to have an almost constant phase as when the blade motion is prescribed, the induced velocity due to the motion will be small. On the other hand, the pressure side presents a highly smooth favorable pressure gradient with a significant variation at the trailing edge, due to the wake.

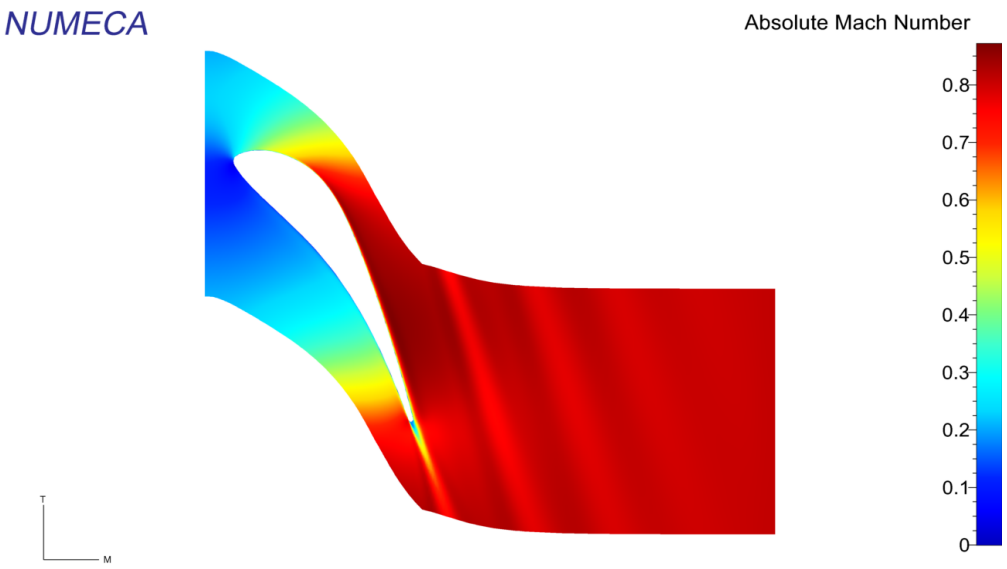

Figure 5.34: STCF4 case 627: B2B Mach number view at 50% span

Unsteady results: Case 627

For this case the wizard provided the full set up in less than a minute and it ran for $\approx$ 50 hrs with 3 processors. Figure 5.35 shows the recovered aerodynamic damping coefficient from the flutter wizard. In this case the reference pressure is $P_{ref} = 4121\ Pa$ with the same physical displacement and same vibration frequency as Section 5.2.2. In this case, the wizard predicts that eight conditions will onset flutter, from $\sigma = -144°$ to $\sigma = -18°$. The least and most stable conditions are found at $\sigma \pm 72°$, respectively. The main outcome is that the system is providing a non flutter free configuration. In order to gain more insight of the result a manual detailed analysis against experimental data is performed.

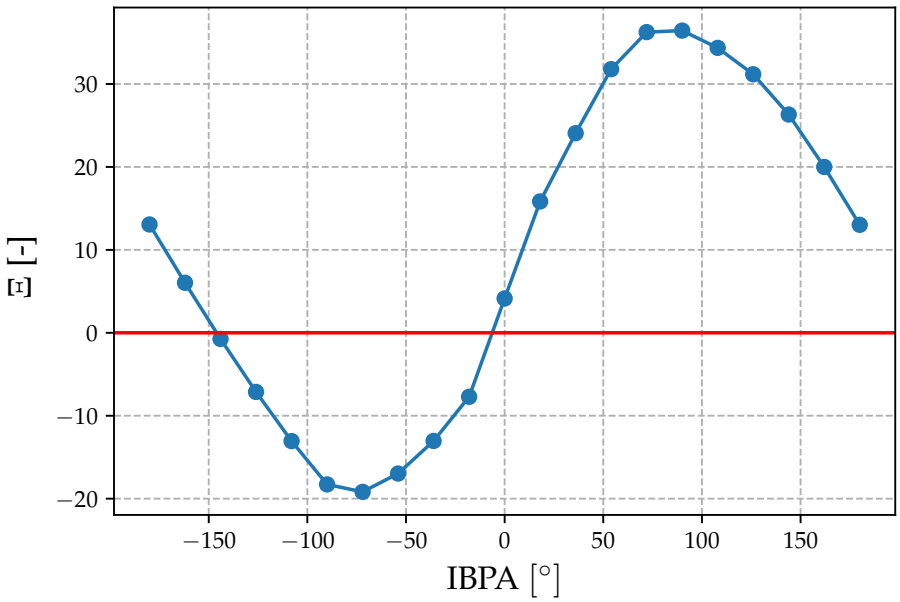

Figure 5.35: STCF4 case 627: Aerodynamic damping coefficient output from Flutter Wizard tool

The first reference IBPA to be compared with its experimental data is $\sigma = 180°$ followed by the most and least stable conditions and in all of them the harmonic content is contrasted. For the former IBPA the obtained aerodynamic damping coefficient was $\Xi = 13.06$, whereas the reference is $\Xi_{exp} = 10.52$. Both results predict an stable condition with close agreement in magnitude. Despite, the good quantitative and qualitative agreement the harmonic content is analyzed manually in detailed in terms of phase and harmonic pressure coefficient at 50% span in Figure 5.36.

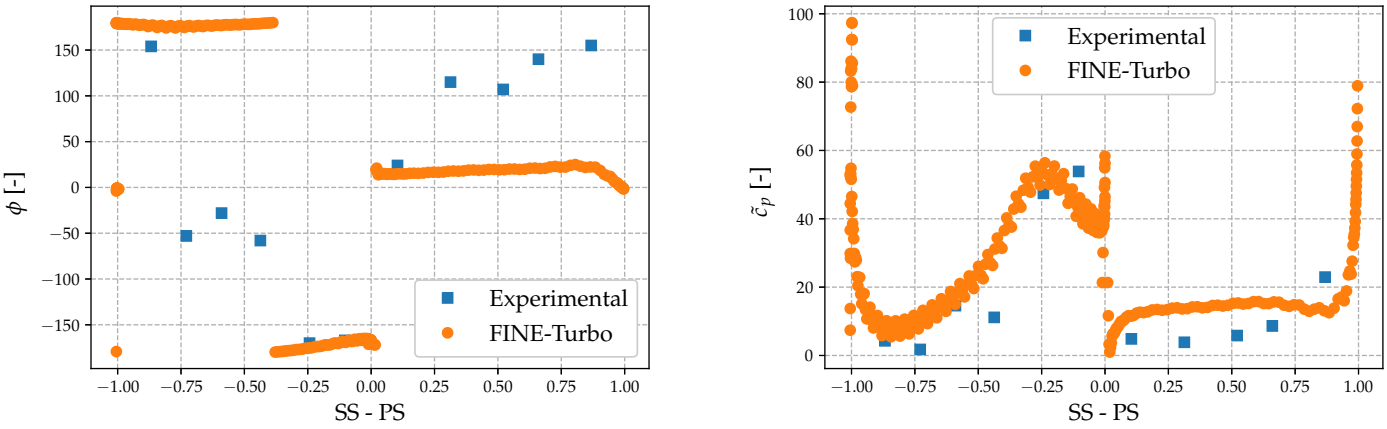

(a) ϕ: $\sigma = 180°$ (b) $\tilde{c}_p$: $\sigma = 180°$

Figure 5.36: STCF4 case 627: Harmonic content at $\sigma = 180°$ at 50% span

Sub figure 5.36a shows a quantitative difference in both pressure and suction sides of the phase. Regarding the pressure side, an unstable condition is predicted by both results but the magnitudes and trends are considerably different. At PS, experimental data predict a gradual increase of in-phase but numerical results display an almost constant phase with a trend towards a stable condition closer to the trailing edge. Regarding the suction side, along the first quarter of this section both results are congruent to one another. After this region, the experiments predict a gradual change of phase towards the trailing edge whereas the numerical results report a phase shift at 50% with no variation afterwards. The unsteady effect in both real and imaginary components has the same ratio along the suction side generating an almost constant phase. The clear numerical change of phase is attributed to the definition of the non-continuous phase angle definition. Nevertheless, the phase direction variation root cause is unclear. Sub figure 5.36b shows the variation of the harmonic pressure coefficient along the chord. Along the SS, there is a high rate of amplitude variation from point to point. However, the main trend followed by the suction side matches with the experimental data with magnitude variations in the first quarter of the chord. Regarding the pressure side, the amplitude is being overestimated by the numerical results, but the trend of an almost constant amplitude with an increase towards the trailing edge is conserved for both results. The regions with an almost constant velocity field, (30%c_n - 80%c_n), produced similar magnitudes as predicted by the steady state results.

Figure 5.37 display the aerodynamic damping coefficient from the wizard and its contrast with the experimental data. Sub Figure 5.38a shows a clear magnitude difference between the current numerical results and the experimental data. In particular at $\sigma = \pm 54°$ in which an opposite trend with respect to its neighbors is predicted, this trend is assumed to be associated to the integration of the harmonic content as it was proved by Fransson [39] the sensitivity of the aerodynamic damping coefficient for small variations in phase and amplitude. The proportional aerodynamic power ratio shown in Sub Figure 5.37b displays

a similar trend on the backward traveling wave from both references. The forward traveling wave trend contains clear differences, in particular at $\sigma = 54°$. Nevertheless, both results predict almost the same flutter region, providing a good qualitative match. From the current results, the most and least stable conditions are found at $\sigma = -72°$ & $90°$, respectively. Figure 5.38 displays its corresponding harmonic content.

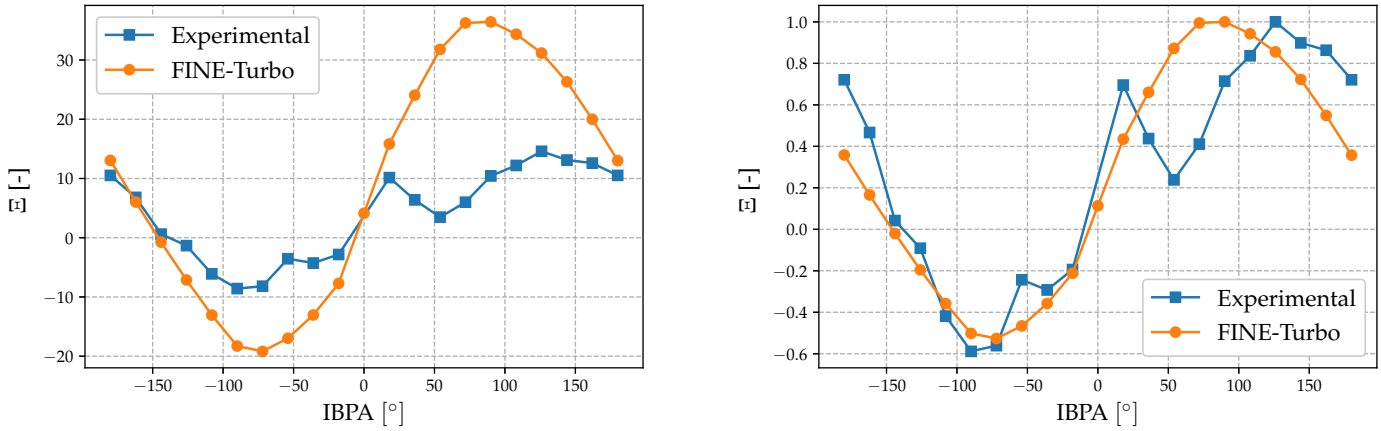

(a) Ξ vs IBPA

(b) Normalized Ξ vs IBPA

Figure 5.37: STCF4 case 627: Aerodynamic damping stability curve validation

Sub Figures 5.38a and 5.38c display the phase at the least and most stable conditions. The prediction along the suction side in both cases match with the experimental data. Regarding the pressure side, the agreement is on a qualitative level only on the former Figure. The latter, shows a discrepancy as numerical results predict a small out of phase condition, and the experimental a tendency to a high in-phase. At this region, the phase behaves on the same trend as shown in sections 5.2.2 and 5.2.3. The phase changes from the leading edge towards the trailing edge, ending with a different phase sign.

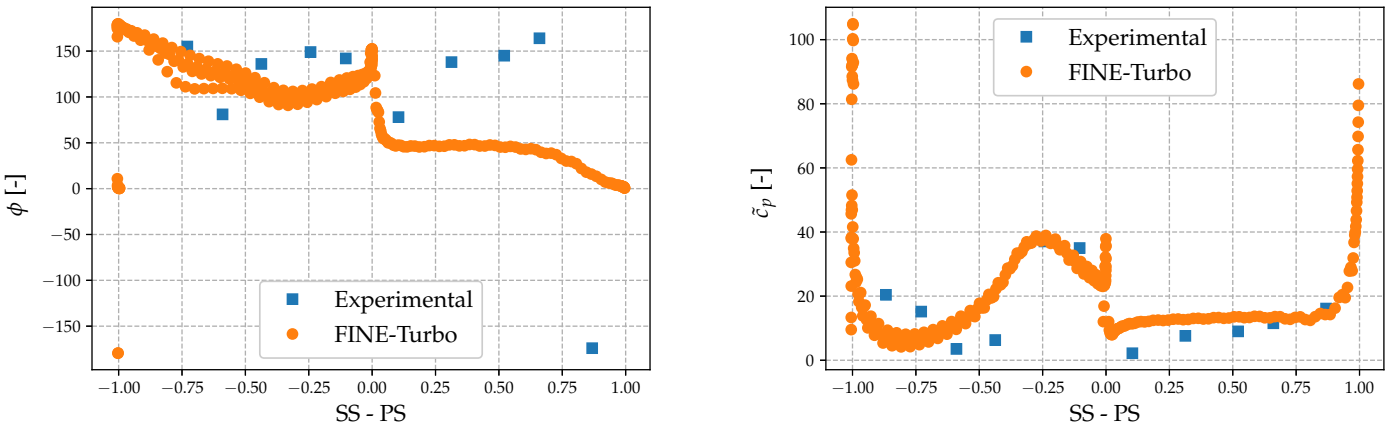

(a) Least stable ϕ: $\sigma = -72°$

(b) Least stable $\tilde{c}_p$: $\sigma = -72°$

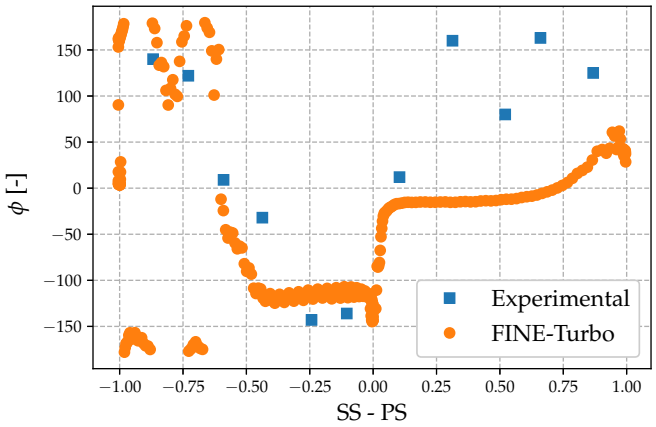

(c) Most stable ϕ: $\sigma = 90°$ SS

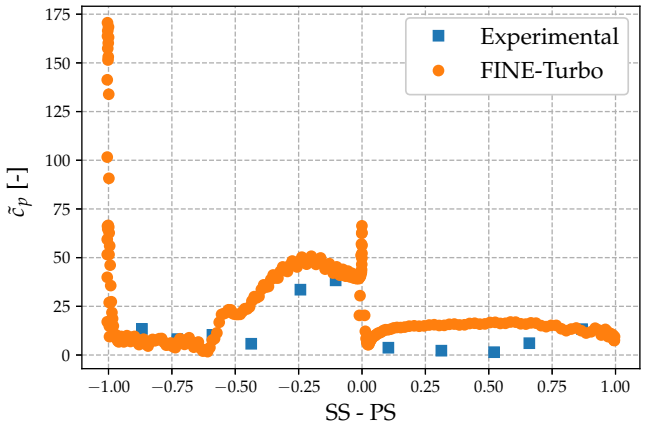

(d) Most stable $\tilde{c}_p$: $\sigma = 90°$ SS

Figure 5.38: STCF4 case 627: Least and most stable harmonic content 50% span validation

Sub Figure 5.38b and 5.38d show the amplitude of the harmonic pressure coefficient for the least and most stable case. In general $\tilde{c}_p$ has a good agreement with the experimental reference in both pressure and suction sides. Most of the harmonic variation occurs at the first half of the suction side. The pressure side in both cases predicts and almost constant amplitude towards the trailing edge. At $\sigma = 90°$, numerical results predict that the pressure side peak at the trailing edge is totally vanished but there is a clear increase in magnitude at the trailing edge of the suction side. It is assumed that the IBPA has a clear effect on the harmonic content of the wake at the pressure side, producing a shift to the SS.

The rate of change of the aerodynamic power has a similar trend from experimental and numerical results, but the experimental peaks are not recovered numerically. Additionally, for this case the $\tilde{c}_p$ has a very good agreement with experimental data in both suction and pressure side, for the reference IBPA, so as with the least and most stable conditions as well. Regarding the phase, the suction side has a qualitative agreement along the suction side. However, at the pressure side the phase has a qualitative match except at the least stable condition. In all cases, experimental data predicted an increase in clockwise direction of the phase as moving towards the trailing edge, which is not captured numerically.

5.2.4 Case 628

Steady state results: Case 628

Case 628 corresponds to a supersonic case with an isoentropic outlet Mach number of 1.42. The incidence angle is the lowest compared to the two previous cases, $\alpha_1 = -12°$. Figure 5.39, shows the isoentropic Mach number at 50% span comparison with experimental data. Numerical results match in a general trend with the experimental data, in particular at the pressure side. Along the suction side the main difference occurs around 50% of the chord. At this region there is a local increase in Mach followed by a decrease around 60% of the chord. This trend is captured numerically but slightly shifted towards the trailing edge. This region corresponds to the reflection of the oblique shock wave occurring at the trailing edge from the most proximate neighbor blades. Towards the trailing edge, the isoentropic Mach is slightly under predicted which changes slightly the oblique shock angle.

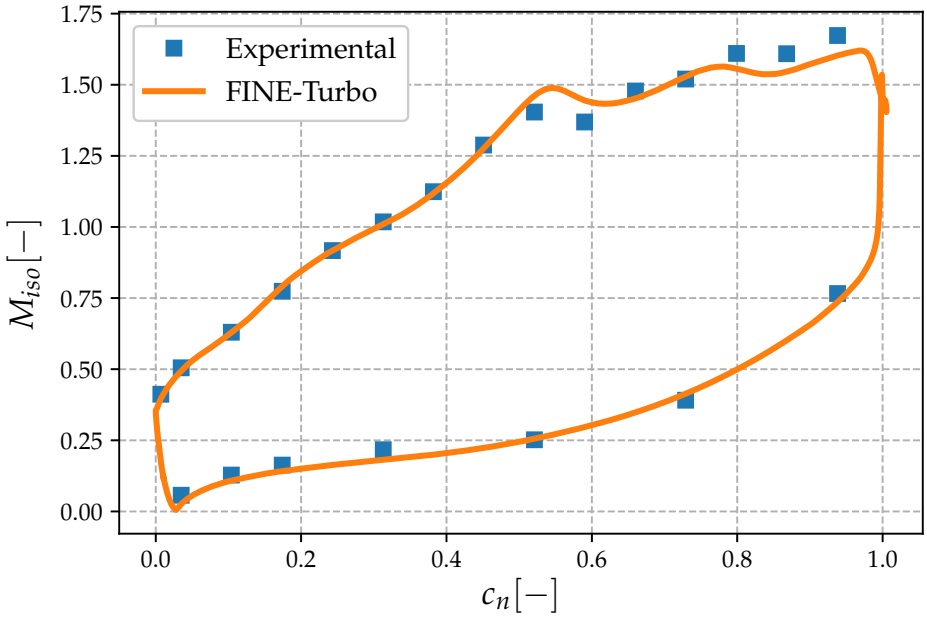

Figure 5.39: STCF4 case 628: M_{iso} vs c at 50% span validation

Figure 5.40 shows a blade to blade view from the absolute Mach number contour at 50% of span. In this figure the interaction of one neighbor row is included. The flow is fully supersonic along the suction side and at the trailing edge there is an oblique shock wave known as *fish tail*. Downstream the wake, the flow is still supersonic but with a lower Mach number as before the fish tail, which is typical of an oblique shock wake. The effect of further downstream wakes is reduced due to the shock in comparison with Sections 5.1, 5.2.2, and 5.2.3. The fish tail shock is impinging the suction side of the neighbor blade. This produces a local increase in the Mach number and after it, the static conditions increase similar to a normal shock wave producing a decrease in the Mach number as shown in Figure 5.39. Thus, the impingement shift might be slightly influenced by the leaving Mach number at the trailing edge.

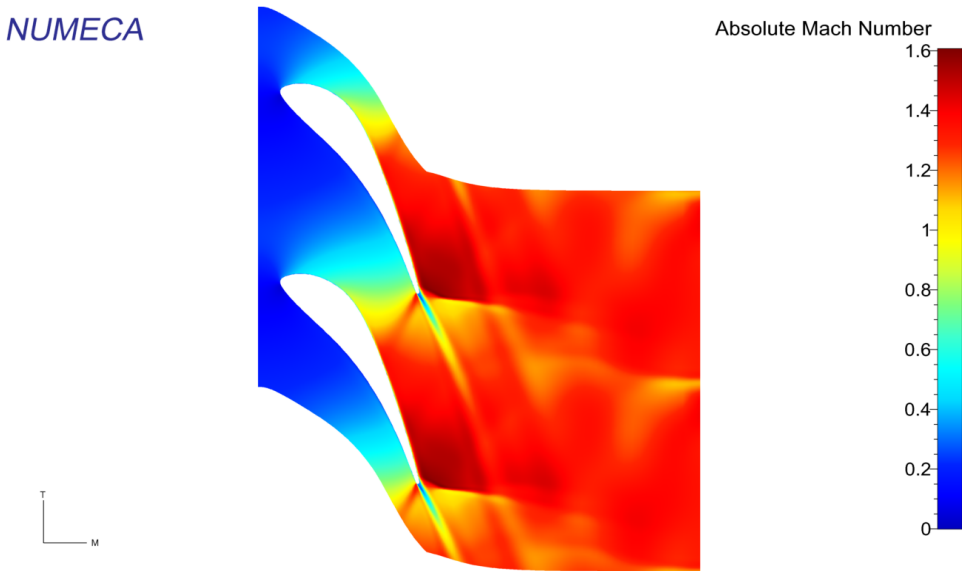

Figure 5.40: STCF4 case 628: B2B Mach number view at 50% span

Unsteady results: Case 628

For this case the wizard set up took less than one minute as in the previous cases but it ran for ≈ 30 hrs with three processors. Figure 5.41 shows the recovered aerodynamic damping coefficient from the flutter wizard. For this case the reference pressure is $P_{ref} = 6297\ Pa$ with the same physical displacement and same vibration frequency as Sections 5.2.2 & 5.2.3. In this figure, the wizard predicts four IBPAs will produce an onset of flutter and again on a backward traveling wave within an IBPA range of $\sigma = -72°$ to $\sigma = -18°$. The least and most stable conditions are found at $\sigma = -54°$ & $108°$, respectively. A manual comparison against experimental data is performed first at the first reference IBPA, $\sigma = 180°$. At this IBPA, the retrieved aerodynamic damping coefficient is $\Xi = 18.2$, whereas the experimental reference is $\Xi_{exp} = 7$. Both results predict a qualitative agreement, whereas the magnitudes have a clear difference, which it might be related to scaling factors rather than flow physics. In order to assess this assumption, a deeper understanding of the variations in magnitude of these coefficients is assessed by its harmonic content. Figure 5.42 contains the harmonic content in terms of phase and pressure coefficient at 50% of the span where the experimental data can be compared.

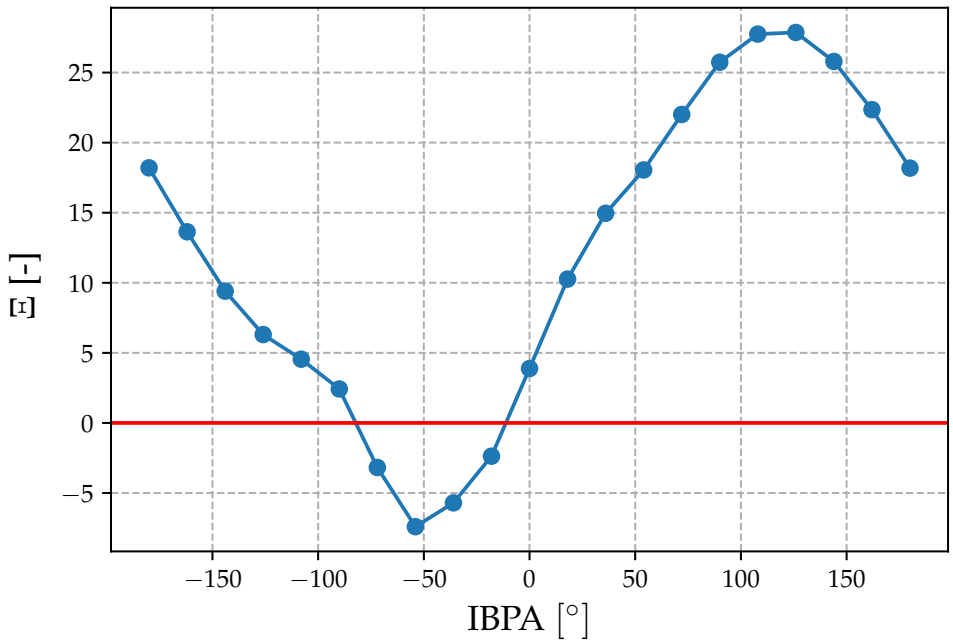

Figure 5.41: STCF4 case 628: Aerodynamic damping coefficient output from Flutter Wizard tool

Sub Figure 5.42a, shows the phase over the PS and SS. Along the PS the phase is positive with a tendency of increasing its magnitude towards the trailing edge. This effect might be related to the upstream wake effect and not to the fish tail as this effect is also captured in Section 5.2.2. At this same region, numerical results predict a phase increase afterwards, starting from 75% of the chord. Both, numerical and experimental predict, have a qualitative agreement as on both it is predicted an unstable phase. At the SS, there is an apparent strong difference between both data in terms of phase. Experimental results display an unstable case for most of the chord, whereas numerically most of the chord is stable. These high differences in phase are assumed to be by the the definition of the phase angle, which has a discontinuity from 180 ° to -180 °, as the difference in angle are small ≈ 5°. Nevertheless, the differences provide an opposite phase that affects directly the stability. The experimental sudden change around 60% of the chord

correlates with the prediction of the reflection oblique wave. A clockwise increase of phase is also found numerically but shifted around 75% of the chord however, this seems not to be related to the steady flow physics.

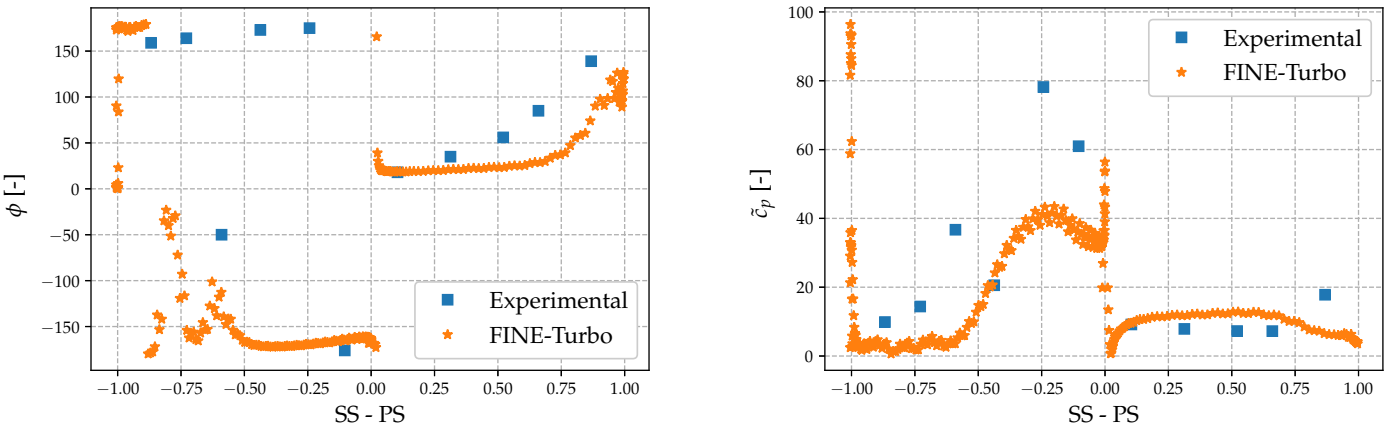

(a) ϕ: $\sigma = 180°$

(b) $\tilde{c}_p$: $\sigma = 180°$

Figure 5.42: STCF4 case 628: Harmonic content at $\sigma = 180°$ at 50% span

Sub figure 5.42b shows the amplitude of the harmonic pressure coefficient. Along the PS there is a good agreement between the numerical and experimental data, with a difference in trend towards the trailing edge but reproducing small amplitudes in both cases. Additionally, this case is the first one in which at $\sigma = 180°$ the peak of the trailing edge is fully vanished. However, the SS contains a high content, which might lead to an indication that in fact the harmonic content has shifted towards the SS by the TE, similar to the most stable case from Section 5.2.3. Along the SS, the amplitude of the numerical results is under predicted by almost a factor of 2. The main difference rises around 60% of the chord, which correlates with the region of fish tail shock reflection. At this region, experimental results show a peak on $\tilde{c}_p$, whereas the numerical approach does not capture the reflected shock harmonic content as it displays a low amplitude at this region even further downstream. For this case, the addition of the dot product of the harmonic pressure coefficient and the sine of the phase at each location provides a positive value, meaning the system is unstable. However, this instability is not found in the aerodynamic damping coefficient, leading to the assumption that the damping coefficient was obtained not exclusively by the shown experimental data.

Figure 5.43 displays the comparison of stability curve from the flutter wizard and the experimental reference. Sub Figure 5.43a shows that both data predict an onset flutter condition on a backward traveling wave. The experimental and numerical flutter regions are, $\sigma = -126°$ & $-18°$ and $\sigma = -72°$ & $-18°$, respectively. The experimental and numerical least stable conditions are at $\sigma = -90°$ & $-36°$ respectively, whereas the most stable conditions are found at $\sigma = 90°$ & $108°$, respectively. On a backward traveling wave, apparently, the trend between experimental and numerical results is captured better than the forward traveling wave. Sub figure 5.43b shows the recovered proportional aerodynamic power for each case, here the highest differences rise at the backward traveling wave, and the forward traveling wave has a better agreement between results. Nevertheless the differences in BTW are dominant and the results are in high difference by the proportional aerodynamic work.

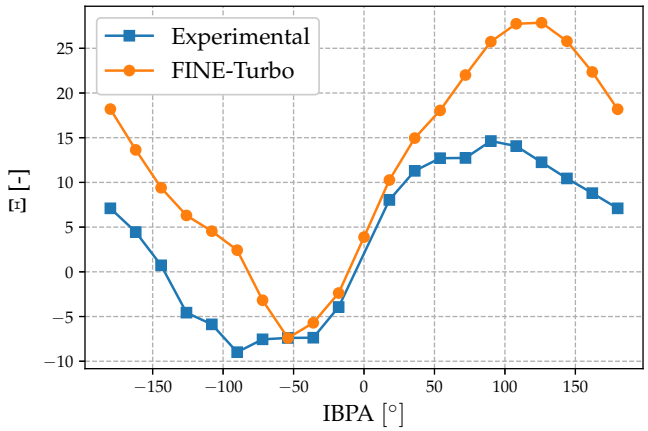

(a) Ξ vs IBPA

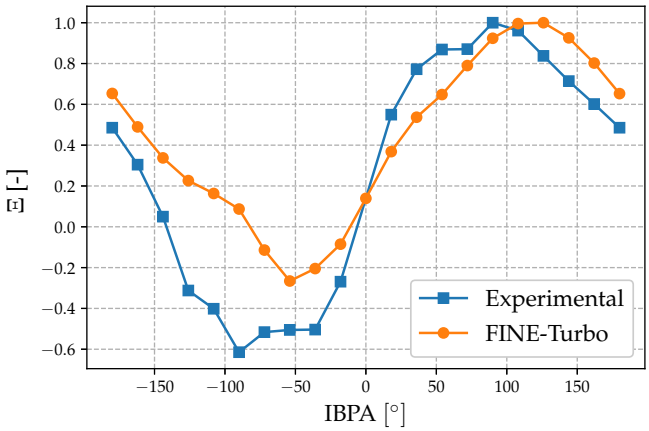

(b) Normalized Ξ vs IBPA

Figure 5.43: STCF4 case 628: Aerodynamic damping stability curve validation

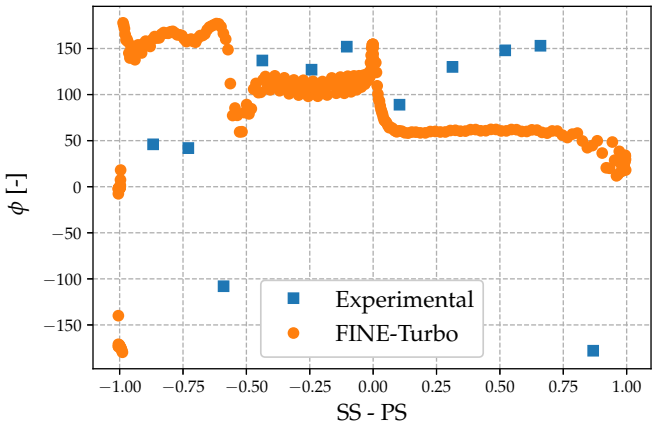

(a) Least stable ϕ: $\sigma = -54°$

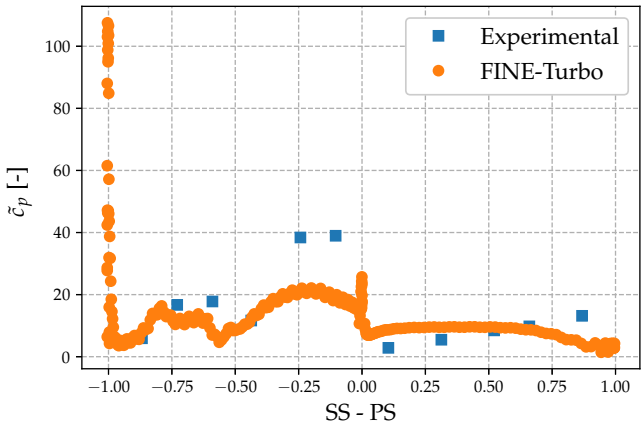

(b) Least stable $\tilde{c}_p$: $\sigma = -54°$

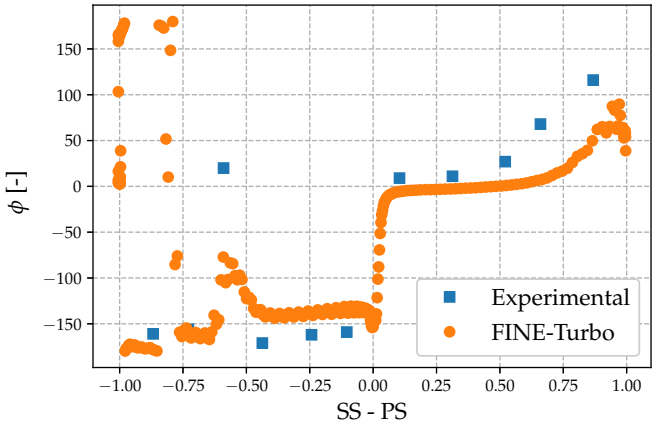

(c) Most stable ϕ: $\sigma = 126°$ SS

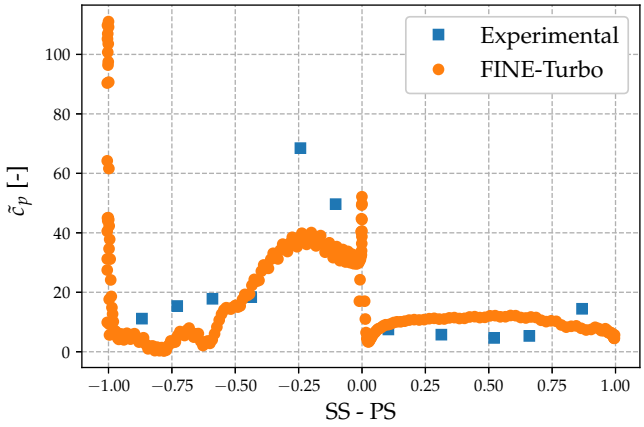

(d) Most stable $\tilde{c}_p$: $\sigma = 126°$ SS

Figure 5.44: STCF4 case 628: Least and most stable harmonic content 50% span validation

The selected IBPAs to obtain the harmonic content as least and most table conditions are $\sigma = -54°$ & $72°$ respectively, and its harmonic content is found in Figure 5.44. Sub figures 5.44a and 5.44c, show the phase content for the least and most stable conditions, respectively. Qualitatively, both cases match with the experimental data along the PS and with slight differences at the SS. Along the PS, the phase changes from an almost constant high in-phase to an increasing phase towards the trailing edge. At the SS there is a jump in phase at $\approx 60\%$ of the chord due to the oblique shock reflection that is slightly captured numerically. In these figures, there is clear the effect of the IBPA over the general phase along the chord in which the SS is much more sensitive. Sub figures 5.44b and 5.44d display the variation of $\tilde{c}_p$ for the last and most stable case. In both cases the trends along the PS and SS are in agreement with experimental data. Quantitatively, numerical results match with the experimental at almost all regions but at the first quarter of the suction side where the amplitudes are underestimated. At $\approx 60\%$ of the chord there is a slight capture of the shock by numerical results, which experimental results predict slightly as well. At the PS near the trailing edge it is clear that for the most and least stable condition the harmonic amplitude is almost vanished, as this effect occurs for all IBPAs it might be related to the fact that there is a high steep Mach number variation at the PS due to the fish tail. Therefore, despite the difference in aerodynamic damping coefficient from the most and least stable cases, the harmonic content is highly similar between experimental and numerical results, thus the results can be taken as reliable. Additionally, in this Figure is clear the effect of the phase as the amplitude between both cases is similar but the phase changes dramatically and so the the entire system.

5.2.5 Annex 5

The cases shown from Sections 5.2.2 - 5.2.4 are not included in [57] which contains eight different reference cases for STCF4. Those cases vary in terms of IBPA, inlet flow angle, and outlet Mach number with respect to the previous shown. Multiple publications refer to cases 3, 6, 7, and 8 from STCF4 which are contain in Annex 5 from [57]. These are four unsteady cases that have the same operational conditions but just vary its IBPA. These configurations provide a valuable reference as experimental data regarding phase, pressure coefficient amplitude and aerodynamic damping coefficient are available. Therefore, these data lead to a five point stability curve that is used as reference.

In Annex 5 there is a detailed record of experimental data in terms of average flow conditions, blade vibration amplitude, and the harmonic content along the pressure and suction sides. Nevertheless, it has been found a discrepancy in the blade vibration normalized by the chord ($u/c * 1000$). The reference value shown in the Annex does not correspond to the mentioned within the main text. For instance in the main text, Case 3 is prescribed with a vibration amplitude $u/c * 1000 = 3.8$, whereas in the Annex the ratio is 3. Cases 6, 7 and 8 are specified with a displacement ratio of $u/c * 1000 = 3.3$, meanwhile in Annex 5, is $u/c * 1000 = 3$ corresponding to a physical displacement of 0.22 mm. The referenced literature that has compared results with the Annex 5 cases are: Cinella et al. [60], who provides results for an Euler and a Navier-Stokes (NS) solver and Arnone et al. [65]. Therefore, the vibration amplitude and its corresponding ratio that will be used within this section will be in agreement with Annex 5.

Steady state Annex 5

Cases 3, 6, 7 and 8 share the same steady operational conditions. In contrast with all the previous cases in which a detailed inlet and outlet boundary conditions were provided, for this case only mean values at mean span are known by [57]. These cases corresponds to a transonic flow with a target isoentropic Mach outlet of 0.9. The operational conditions characteristics are found in Table 5.10

Annex 5	
P_{t_1} $[kPa]$	205.8
α_1 $[°]$	45
P_2 $[kPa]$	121.2
$M_{is_1}[-]$	0.29
$M_{is_2}[-]$	0.9
f $[Hz]$	150
u $[mm]$	0.22

Table 5.10: STCF4 Annex 5: Operational conditions

The steady state results are compared in Figure 5.45 in which experimental and numerical results are included. It is shown that this high inlet flow angle, corresponds to a small incidence as the stagnation point is located at almost the leading edge of the blade. The result matches with the experimental ones at both pressure and suction sides but with a slightly better agreement at the suction side. Additionally, there is a good agreement with respect to other references results, as regions with high overlapping are shown. In general the flow at this operational condition is highly subsonic at all regions of the blade and the SS has an almost constant magnitude around 0.98 Mach from around 40% of the blade chord. At the trailing edge the presented results are the ones that do not over predict the Mach number, in contrast the reference data from Cinnellla et al. shows peaks at the trailing edge with supersonic conditions, which it is assumed that occur because of a lack or refinement of the trailing edge.

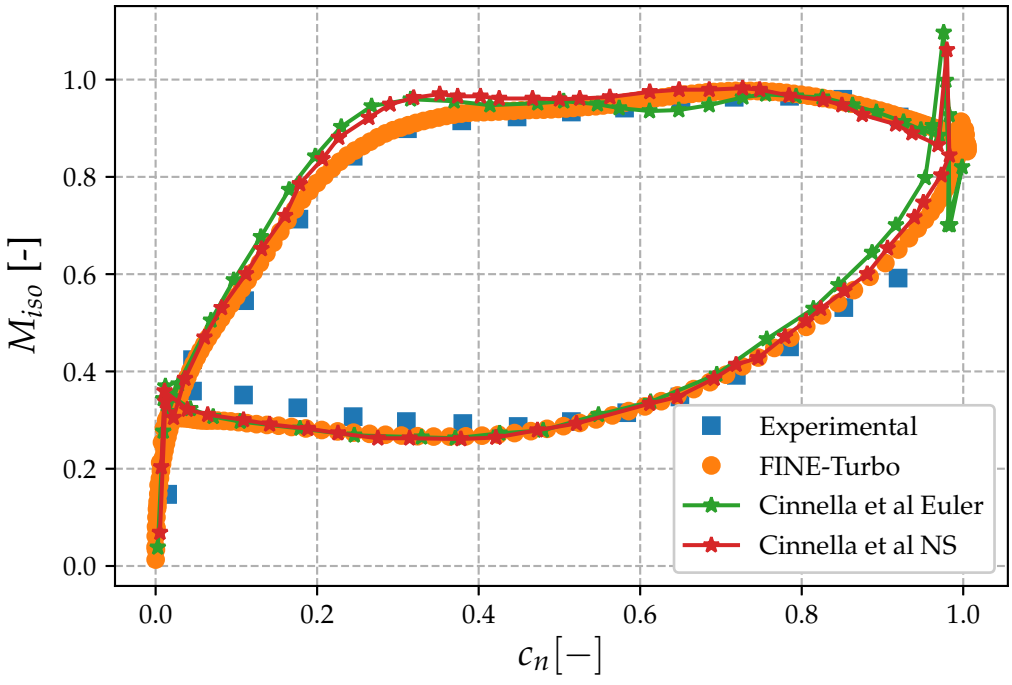

Figure 5.45: STCF4 Annex 5: M_{iso} vs c at 50% span validation

The contour of the absolute Mach number is shown in Figure 5.46. The stagnation point is located slightly at the pressure side, with a fast flow acceleration along the suction side within the first third of the chord. After this region the flow filed velocity is relatively the same until the trailing edge where a localized wake occurs, along this region an almost constant phase is predicted as few gradients along the chord occur. The localized wake in the contour is in agreement with Figure 5.45 that predicts a smooth merge of pressure and suction sides close to the trailing edge. Downstream the effect up to the third neighbor blade is captured. The pressure side on the other hand, presents a smooth velocity gradient up to $\approx 70\%$ of the blade, with a fast acceleration towards the trailing edge.

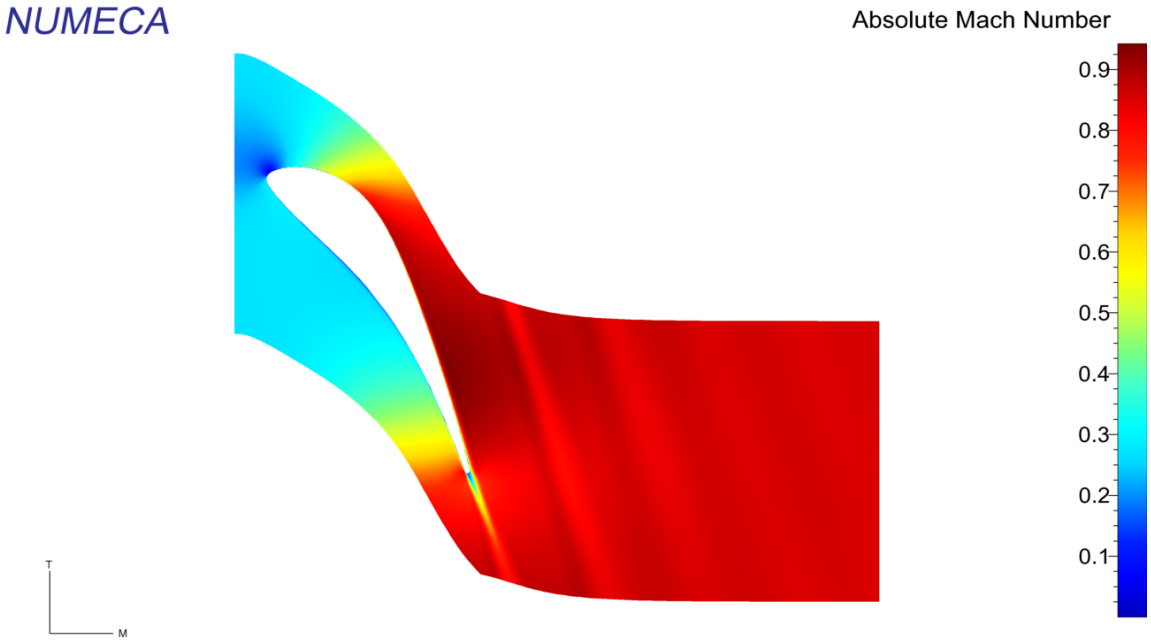

Figure 5.46: STCF4 Annex 5: B2B Mach number view at 50% span

Unsteady Annex 5

The last case from this chapter as well required less than 1 minute to be set up as it has the same geometry as the previous cases shown, however it ran for ≈ 61 hrs with three processors. The physical displacement was set to $u = 0.22\ mm$ and the generalized displacement to 0.5, into the wizard because the modeshape is the same as the imposed displacement, but in this case the vibration frequency is $f = 150\ Hz$ which differs from Sections 5.2.2, 5.2.3 and 5.2.4. Figure 5.47 shows the recovered aerodynamic damping coefficient from the flutter wizard output. For this case the reference pressure is $P_{ref} = 9042\ Pa$. The output form the wizard indicates that the system is not stable, as eight IBPAs predict flutter onset. All flutter region is captured on a backward traveling wave from $\sigma = -144°$ to $\sigma = -18°$. Where the least and most stable conditions are found at $\sigma = -72°$ & $90°$. The first IBPA to be taken as reference is at $\sigma = 180°$ in which it was obtained an aerodynamic damping coefficient of $\Xi = 3.73$, whereas the experimental reference is $\Xi_{exp} = 2.7$. Both results have a good qualitative and quantitative agreement. Additionally, Table 5.11 contains a summary of the predicted aerodynamic damping coefficient from all the references that are compared. The prediction from FINE™/Turbo is in agreement with the magnitude of other references and all of them are stable conditions. The variation source could be due to a different reference pressure or aerodynamic power from each software.

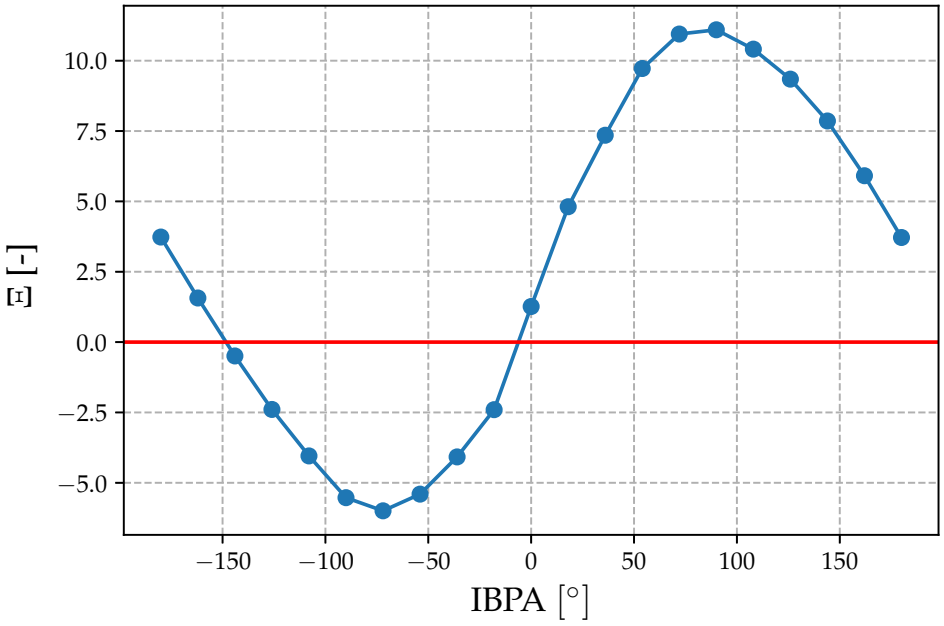

Figure 5.47: STCF4 Annex 5: Aerodynamic damping coefficient output from Flutter Wizard tool

$\sigma = 180°$	
Reference	Ξ
Arnone	4.8
Experimental	2.7
Cinella et al. Euler	3.68
Cinella et al. NS	4.31
FINE™/Fine	3.73

Table 5.11: STCF4 Annex 5: Unsteady aerodynamic damping comparison at $\sigma = 180°$

In order to determine if this result is correct a manual detailed analysis of the harmonic content is performed at 50% span which is shown in Figure 5.48. Regarding the following results, some clarifications are introduced. The first, Arnone et al. only provided only results for $\sigma = 90°$ and that both results presented by Cinnella are in great agreement between one another so these results are refer just as one. Sub Figure 5.48a shows a good agreement of all methods along the suction side up to 30% of the chord. After this region, the aerodynamic force is in a high in-phase condition with the motion of the blade due to the phase angle definition, as the magnitude of the angle decreased further than 180 degrees, and this trend is also captured by the reference data. The most relevant difference is shown along the pressure side at 50% of the chord. In this region all references predict a transition towards a highly in-phase condition at the trailing edge, whereas this trend is not captured by the current result. Regarding the numerical result along the PS, it predicts an almost constant phase as expected from the steady state analysis, but it also predicts a slight change of phase towards the trailing edge, which has been found also in Sections 5.2.2 - 5.2.4.

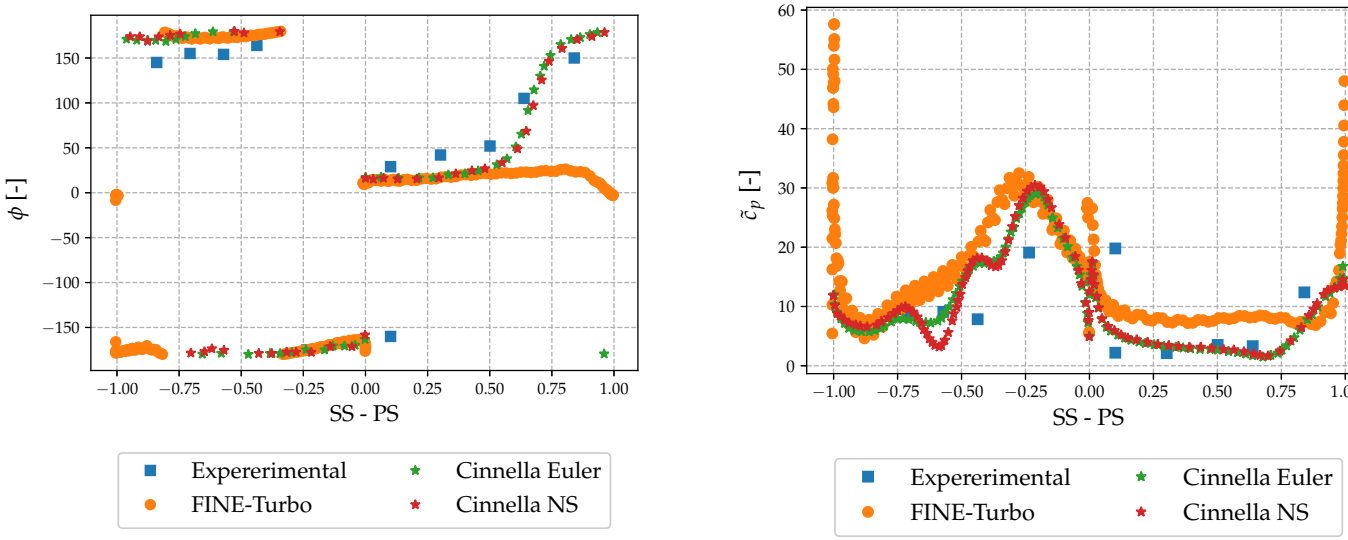

(a) ϕ: Annex A5 at $\sigma = 180°$

(b) $\tilde{c}_p$: Annex A5 at $\sigma = 180°$

Figure 5.48: STCF4 Annex 5: Harmonic content at $\sigma = 180°$ at 50% span

The harmonic pressure coefficient amplitude is shown in sub Figure 5.48b. The numerical results along the pressure side have a similar trend but all references predict an increase of $\tilde{c}_p$ around 75% which is not captured by the current result. Also there is a clear effect at the TE of predicting a high harmonic content whereas this trend is not found by any other authors. However, from the steady state Mach number, the references have an over estimation and a steep Mach variation right at the TE, which was found to vanish the harmonic content. It is assumed that this effect is being caused due to a mesh influence in the TE. In general, most of the amplitude takes place along the suction side before half the chord, at this region there is an agreement between numerical results with slight variation from the experimental ones. After 50% of the chord there are clear differences between the three numerical results but the three of them are in the nearby of of one another. The overall operational condition is stable, as most of the amplitude is taking place out of phase with the motion and the clear difference in phase at the PS towards the TE does not have a big effect in the stability of the system as the harmonic pressure coefficient has a low magnitude and its unstable effect is reduced.

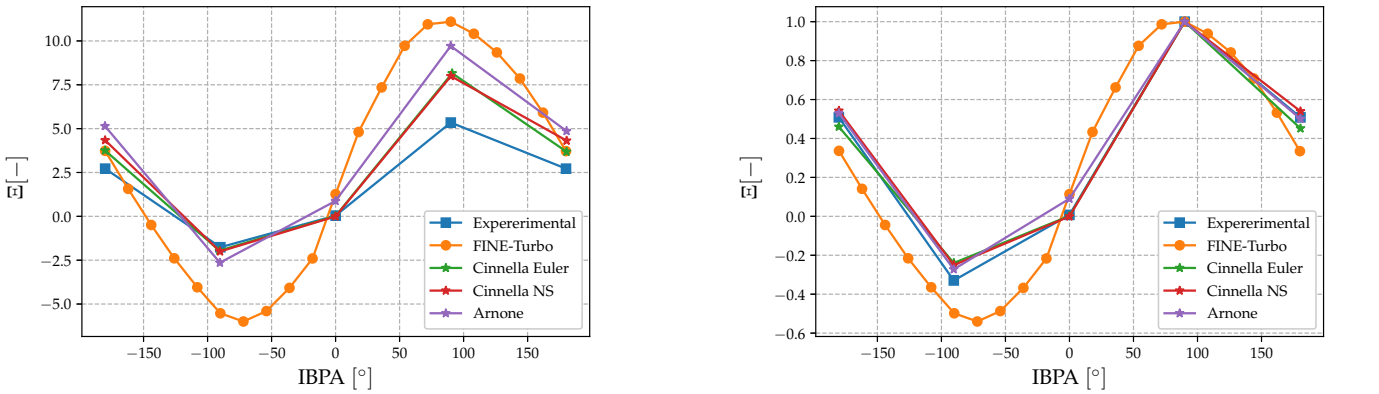

(a) Stability Parameter vs IBPA

(b) Normalized stability Parameter vs IBPA

Figure 5.49: STCF4 Annex 5: Aerodynamic damping stability curve validation

Figure 5.49 displays the aerodynamic stability curve obtained by the flutter wizard for this given operational condition and compares all the reference authors. Sub figure 5.49a shows a good qualitative agreement at $\sigma = 180° \ \& \ 0°$, but there is a clear difference in magnitude at $\sigma \pm 90°$, which is an indication that there might be a different scaling factor from author to author. However, sub Figure 5.49b displays that the proportionality of aerodynamic work per IBPA from all the references is in close agreement from one another. All cases predict a flutter condition on the backward traveling wave at $\sigma = -90°$. Due to the limited amount of IBPAs information from other references, it is unclear weather or not the most and least stable conditions agree from one another. Thus, the least and most stable conditions are assumed to be at $\sigma = -90°$ and $\sigma = 90°$, as experimental data is available. The harmonic content of these conditions is shown in Figure 5.50.

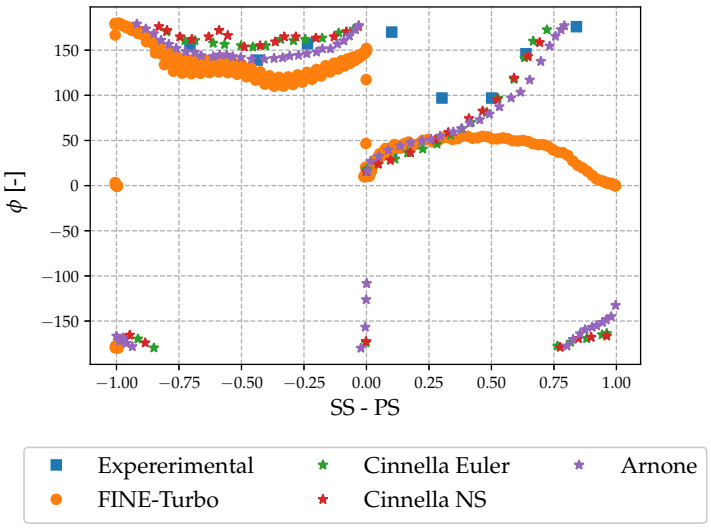

(a) Least stable ϕ: $\sigma = 90°$

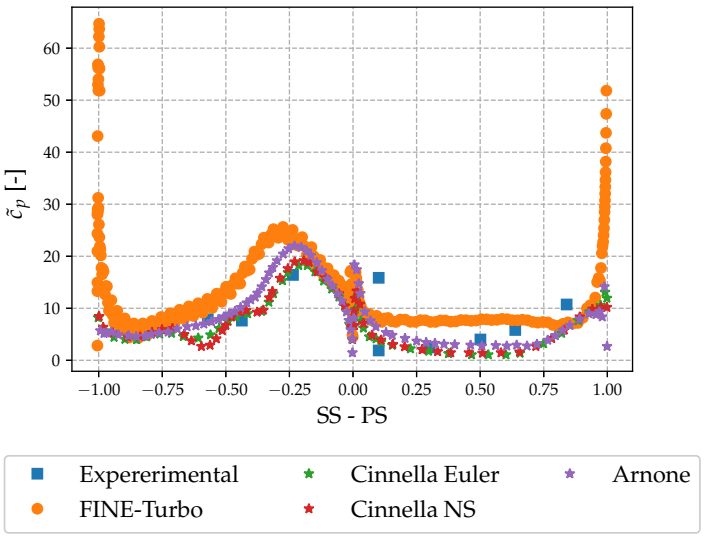

(b) Least stable $\tilde{c}_p$: $\sigma = 90°$

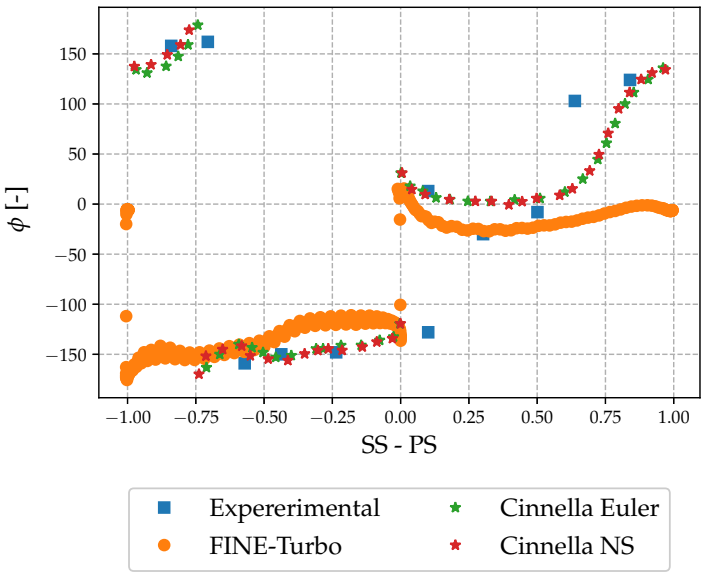

(c) Most stable ϕ: $\sigma = -90°$

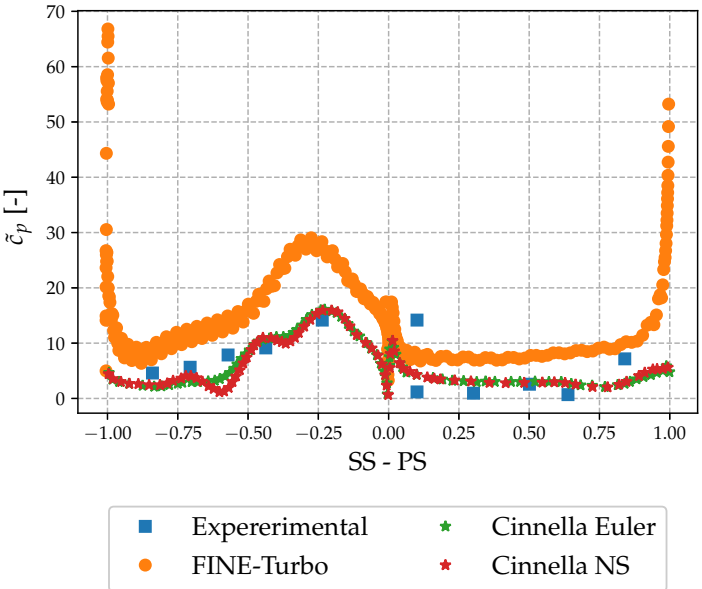

(d) Most stable $\tilde{c}_p$: $\sigma = -90°$

Figure 5.50: STCF4 Annex 5: Least and most stable harmonic content 50% span validation

Sub figures 5.50a and 5.50c, show that there is a good phase agreement between all references along the suction side. The highest difference is found at the most stable phase condition, in which the current results always maintain an out of phase condition showing discrepancy with all other references. However, the angle difference is small but due to the phase definition, this has a consequence on the system stability. On the other hand, at the PS FINE™/Turbo results presents discrepancies in particular after 50% of the chord with respect to the experimental and numerical data, the root cause is unclear but might be related to the wake effect, as the correct trend was only found when the flow was supersonic and the wake had a slighter diffusion (Case 628). However, as the PS predicts a very small harmonic amplitude, this phase variation does not produce any critical effect. All numerical references show a close agreement with experimental data but only after 50% of the chord. There is the same trend from the current results with the numerical ones before 50%, but none of them match the experimental data. At the most stable condition the thesis' results have a match with experimental data up to 50% of the chord. Sub figures 5.50b and 5.50d display the harmonic pressure coefficient. In both figures the increase of the harmonic pressure coefficient at the TE is clear and it does not occur in any other reference, this is could be related to the mesh refinement in this region. In the least stable case, there is a close agreement along the pressure and suction side among all numerical results. The highest differences are found in the first quarter of the chord at the SS. Cinnella results are the ones that have a better agreement with experimental data at the least and most stable cases. Additionally as the PS predicts a very small harmonic amplitude, it does not provide any critical instability the fact that the phase changes at the PS as moving towards the TE, as shown by most the experimental and numerical references. Therefore, these results can be taken as reliable as they are in agreement with the harmonic content of the multiple references. The normalized aerodynamic damping produced similar magnitudes, only small differences in $\tilde{c}_p$, but a better agreement in phase at the SS which is the most critical region.

5.3 Chapter conclusion

A complete flutter analysis of six operational conditions from two turbine Standard Configuration cases (STCF11 & STCF4) have been analyzed in FINE™/Turbo with Spalart-Allmaras as turbulence model. These configurations represent a 20 bladed non-rotating turbine, which its 3D blade geometry is the result of staggering its 2D airfoil along its center of gravity. The blades are moving with an imposed bending motion, that is producing a hub motion as well. For each Standard Configuration a mesh independence study was performed to guarantee a trade-off between CPU cost and accuracy. The flutter wizard developed in Chapter 4 was used to set up each case to retrieve automatically the aerodynamic damping coefficient curve, which provided a clear assessment of the global flutter stability per case. By using the wizard in all cases, the total analysis time was split into engineering and computational time. The former being around 45 seconds for each case and the latter varied in a rage of 30 to 95 hrs. The generalized displacement was kept constant throughout the six evaluated conditions as the imposed motion was the assumed modeshape, producing a generalized displacement of 0.5, whereas the physical displacement was selected per case to agree with the reference data scaling factor. All analyzed cases were compared first with reliable experimental data in terms of the harmonic content, and then with different references depending on data availability at the most critical conditions. Steady and unsteady results were obtained and compared at the reference span of 50% against its normalized true chord (c_n) and for unsteady results a reference IBPA of $\sigma = 180°$. The results within this thesis proved to have a close agreement with respect to experimental data, except in cases in which shock waves occurred. The unsteady analysis was performed by an energetic method in which the stability of the system is determined by the sign of the aerodynamic power done over the blade by the unsteady aerodynamic force. Thus, a negative value represents that the flow field is reducing energy from the system producing a stable condition, whereas a positive sign represents an unstable condition. The aerodynamic damping coefficient was chosen to be in agreement with Fransson & Bölcs criteria, which is retrieved from the aerodynamic power, and as it is used up to date as a standard reference. Furthermore, in all cases the aerodynamic damping coefficient was also normalized against its maximum value per reference, which provided the recovery of the proportional variation of the aerodynamic power per case without any scaling bias.

STCF11 was analyzed at high-subsonic (OPC1) and transonic off-design conditions (OPC2). At high subsonic conditions the flow showed a high acceleration at the leading edge of the suction side with the flow fully attached. There is a very good agreement at 50% of the span of the isotropic Mach number (M_{iso}) with respect to the experimental data. The unsteady analysis was performed by the wizard tool on a B case, it showed that there are two unstable IBPA configurations, with a physical displacement $u = 0.42mm$ at 50% of the span and a vibration frequency of $f = 209Hz$. The highest content of aerodynamic damping is located at the blade tip, as the highest displacement is also located at the tip. At the reference IBPA, $\sigma = 180°$, there is a close match of the aerodynamic damping coefficient against the reference data, with a maximum difference of 4.5%. At this IBPA, the harmonic content had a very close agreement with experimental data, whereas the phase displayed differences specially at the suction side. The least and most stable conditions were found at $\sigma = -36°$ & $122°$ respectively. The proportional aerodynamic power proved to have a good agreement between the current results and the literature references, by predicting the same most stable condition. However, the prediction of the least stable IBPA and the general curve stability after $\sigma > 200°$ differs from author to author. There was almost no variation in magnitude of the harmonic content along the blade for the least and most stable IBPAs. The harmonic content of the least stable condition showed an agreement against experimental results in terms of the harmonic pressure coefficient but not quantitatively in the phase, only qualitatively. The phase was proved to be the key parameter that onsets flutter, when a high in-phase condition along the blade is determined. But as the

numerical results only underestimate the magnitude compared to the experimental ones, but both of them predict an unstable condition, it is concluded that the presented results are in agreement with the flow physics and are reliable. Regarding a correlation with steady state results, after the maximum steady Mach number ($\approx 25\% c_n$) of the suction side there is a tendency of $\tilde{c}_p$ to decrease its magnitude, which was kept regardless of the IBPA. Additionally, the peaks of harmonic amplitude close to the trailing edge are assumed to be due to the high wake harmonic content and due to the mesh refinement at this region.

OPC2, shows the most complex steady state flow around the blade as viscous and non-linear effects are involved. At the reference blade height, the flow has a laminar separation bubble at the SS near the leading edge, a reattachment location, and a normal shock wave towards the trailing edge. The results were compared against experimental and numerical reference data (FINSUP solver, Cinnella et al., Patil et al.). The current steady state results differ with experimental data on the reattachment location of the flow and at the steep Mach number variation due to the normal shock wave. The current results match at its maximum Mach number, right after this region it is not captured the sudden Mach decrease. Further numerical references predict earlier the shock wave with a lower Mach number, with a better agreement with the experimental data after the shock wave. This is assumed to be due to a variation at the outlet static pressure set as boundary condition, as this is the main driver to change the shock position. An additional analysis was performed with a much refined mesh and SST as turbulence model and no significant effect was found, straightening the assumption that the outlet pressure must have been modified in some degree. The output from the flutter wizard showed three unstable regions at a backward traveling wave, and its least and most stable conditions are at $\sigma = -54°$ & $122°$ respectively, with a physical displacement $u = 0.27\ mm$ at 50% span and a vibration frequency of $f = 212\ Hz$. Different maximum and minimum IBPAs are shown by Cinnella and Patil whereas FINSUP solver has a match with the current results. At the reference comparison IBPA of $\sigma = 180°$ the aerodynamic damping coefficient is in range of further references predictions, showing a stable condition $\Xi = 6.32$ whereas the viscous solver and harmonic balance references show a range between 7.9 to 8.9, providing the current results to be the most conservative. Regarding the harmonic content at this reference IBPA, the amplitudes along the first quarter of the SS show a high difference between results, this region corresponds to the laminar bubble separation. Additionally, at the location of the shock wave, quantitative differences in all references are found, but it was always predicted an increase of the harmonic pressure coefficient. Regarding the phase, all results are in agreement at the pressure side but there are high qualitative and quantitative variations at the suction side from author to author. Nevertheless, in the current results the pressure side showed an almost constant phase which is not in agreement with the reference data, the root cause of this is unclear. Finally, regarding the aerodynamic damping coefficient the highest differences exist at low stability regions with a clear trend difference from Cinnella et al. A comparison of the obtained harmonic content against the experimental data at the least stable condition showed a good agreement in phase with an under prediction of the harmonic amplitude, concluding the unstable numerical condition can be taken as a reliable result. However, as a future work this case should be analyzed with further numerical references to determine the true variation trend, in particular the phase from the suction side. The high variation among numerical data is assumed to be due to its case complex steady state flow physics.

Four configurations were evaluated with different operational conditions in STCF4, which its geometrical properties differ in chord, stagger angle, blade vibration frequency and physical displacement with respect to STCF11. These configurations are: Case 624, 627, 628 & Annex 5. All cases contain experimental data from the harmonic content and aerodynamic damping coefficient, making them highly valuable. The first three cases could only be compared against experimental data but the fourth also with literature references. Case 624 has a transonic flow with an outlet $M_{iso} = 1.04$ with a stagnation point along the

pressure side near the trailing edge. The steady results at the reference blade height, show a general good agreement with respect to experimental data. Nevertheless, experimental results show a drop of Mach number around $65\%c_n$ that is not captured numerically, assuming it occurs due to a local normal shock found experimentally. The main shock wave is located at $\approx 85\%c_n$, which is captured with good agreement. The flutter wizard output predicts seven unstable conditions on a backward traveling wave, producing the least and most stable conditions at $\sigma \pm 72°$ with a blade vibration frequency $f = 149\ Hz$ and a physical displacement $u = 0.3\ mm$. These critical IBPAs match only on the most stable condition against the experimental data. At the reference IBPA, the aerodynamic damping coefficient had clear quantitative difference ($\Xi = 10.16$ & $\Xi_{exp} = 3.4$). However, the harmonic pressure coefficient amplitude showed to be in close agreement to the experimental data but there are multiple differences in the phase. The pressure side displayed the highest differences in phase, the current results were estimating a lower magnitude leading to a higher aerodynamic damping. The recovered proportional aerodynamic damping showed that experimental values predict two peaks that do not match the harmonic behavior at $\sigma = -36°$ & $-72°$ with high stability, meanwhile its neighbors are unstable cases. Therefore the least stable condition was changed to be at $\sigma = -90°$ to compare the numerical results with a high unstable experimental case. The highest differences in trend were found at low magnitudes of IBPA whereas at higher IBPA values it is clear a better agreement of experimental and numerical results. The least and most stable cases show a good agreement in terms of harmonic pressure coefficient along the pressure side however, clear differences took place in normal shock waves regions. Regarding the phase, there is a qualitative agreement but not fully along the chord. Small differences were found at the least and most stable conditions regarding the harmonic pressure coefficient compared to the ones obtained regarding the phase. Therefore, the phase is proven to be the key driver for stability. The shock wave produced a high harmonic content regardless of the IBPA. The shock effect on the phase showed that the phase has a tend to change to the opposite condition as before the shock. Finally, at any IBPA, the phase at the PS towards the trailing edge was unable to capture the experimental results and in all cases provided a tendency towards a stable condition meanwhile experimental data predicted an unstable one.

Case 627 is a case with a high subsonic flow, with $M_{iso} = 0.85$. The numerical steady state results at the reference blade height are in very good agreement with experimental data, in particular along the suction side. The suction side has the characteristic of having an almost constant Mach ≈ 0.9 with a very smooth mixing of the pressure and suction side flows. The output of the flutter wizard predicted eight unstable regions at a backward traveling wave, with the most and least stable conditions at $\sigma = -72°$ & $90°$ respectively, at the same blade vibration frequency and physical displacement as Case 624. Only the least stable condition match with the experimental data, experimentally the most stable is at $\sigma = 126°$. At the reference IBPA there is a good agreement between aerodynamic damping coefficient and the experimental one with $\Xi = 13.06$ and $\Xi_{exp} = 10.52$, respectively. Also, the harmonic pressure coefficient has a close agreement with experimental data, and regarding the phase it has an almost constant magnitude at the pressure side and at the suction side as predicted from the steady state condition. This is assumed to be as the induced unsteady velocity due to the blade displacement will cause almost the same effect on the flow field on a region with constant velocity field. Nevertheless, the trend in phase mismatches highly with experimental data in particular along the PS, the root cause of the variation of the experimental results is unknown. The least and most stable conditions show a high agreement in harmonic pressure coefficient at both SS and PS against experimental data. At the most stable condition there is a complete vanish of the peak at the trailing edge along the PS but the peak at the SS was increased, thus the IBPA showed a clear effect on the wake. Also, a close agreement is shown in the phase along the SS but not at PS. It is assumed that the quick variation of pressure field towards the trailing edge is being highly affected by the harmonic motion of the blade. All aerodynamic damping coefficients obtained by the flutter wizard

and the experimental results present a quantitative discrepancy up to three times the experimental value at some IBPAs and a difference in trend at $\sigma \pm 54°$. However, the recovered proportional aerodynamic damping variation showed a closer trend between the results by removing the scaling factor but only along the backward traveling wave, with high discrepancies at $\sigma = 36°,\ 54°$ & $72°$. At all IBPAs the maximum harmonic content of $\tilde{c}_p$ was found at 25% of the chord along the SS. This is assumed to be due to a steady state condition and correlates with the location where the maximum Mach number is reached.

Case 628 is a supersonic flow condition with $M_{iso} = 1.42$ at the outlet. The steady results show a general agreement against the experimental ones. The differences took place at the predicted maximum Mach at the trailing edge and the influence of the reflection oblique shock from the fish tail, in which numerically a slight shift towards the trailing edge is predicted. The blade vibration frequency was $f = 152\ Hz$ with the same physical displacement as Case 624 and 627. The aerodynamic damping coefficient curve obtained by the flutter wizard predicted four regions in which flutter will be onset on a backward traveling wave configuration. The least and most stable conditions are at $\sigma = -54°$ & $108°$, respectively. The experimental data predicted the critical conditions at $\sigma \pm 90$. At the reference IBPA, the aerodynamic damping coefficients differs from $\Xi = 18.2$ to $\Xi_{exp} = 7$, thus the harmonic content is compared to determine the validity of this result. The harmonic pressure coefficient is under estimated at the first quarter of the SS and a peak at the shock reflection is not captured numerically but at the PS there is a good agreement between results. Regarding the phase, the pressure side is in a qualitative agreement with respect to experimental data. Along the SS, numerical results predict an out of phase condition whereas experimental a high in-phase. This difference in phase angle occurs as the variation appear on the limit of the phase definition continuity, as the difference is $\approx 5°$. However, the combination of the experimental phase and $\tilde{c}_p$ is producing an unstable condition whereas its global aerodynamic damping coefficient predicts a stable one. It is assumed that the provided data is not the only one used for obtaining the full blade stability. For this case the normalized aerodynamic damping coefficient between results present a clear difference in trend on a backward traveling wave as experimental results show seven unstable conditions and numerical predicts just four. The most and least stable conditions obtained numerically were compared against its corresponding experimental data. A good qualitative agreement in the both cases was obtained over both blade sides in terms of $\tilde{c}_p$. The harmonic amplitude showed a good agreement in general except at the first quarter of the SS, in which the numerical amplitude was under predicted but in all cases at the PS the peak towards the TE was vanished. As in all analyzed IBPAs the harmonic peak at the trailing edge was vanished, it is assumed that this is due to a steady state flow field, in specific due to fish tail shock, which leads to a high Mach variation at the trailing edge. However, this effect increases the harmonic content at the SS, which would affect the system depending on the phase at this region. It might be due to the fact of a high steep variation in Mach number at the trailing edge in which the influence of the blade motion is not producing a significant effect. Regarding the phase, the reflection shock predicted a local increase towards the opposite phase before the shock, with agreement at the SS but not at the PS, which its root cause is unknown. At 25% of the chord along the SS, the maximum $\tilde{c}_p$ was found regardless of the IBPA. At this location no particular flow field physics has been encountered, rather than the fact that the flow is turning transonic. The reflection shock produced a change in phase towards the opposite value before the shock. Additionally, it produced a local increase in $\tilde{c}_p$ regardless of the IBPA.

Annex 5 is a case which was designed for $M_{iso} = 0.9$. The results were compared against the experimental data and three numerical results from literature (Cinnella et al. and Arnone et al.). The isotropic Mach was compared against experimental results and only two numerical references due to data availability. The current steady result have a good agreement with all other references and in particular with the experimental data. Other numerical references shows a high variation at the trailing edge over

predicting the Mach number, which is an indication of a not fully refined mesh at the TE. Along the SS there is an almost constant Mach for ≈ 40% of the chord, in which was expected an almost constant harmonic content. Regarding the unsteady results, the flutter wizard predicted eight unstable cases, on a backward traveling wave as in all previous analysis, with a blade vibration frequency $f = 150\ Hz$ and a physical displacement $u = 0.22\ mm$. At the reference IBPA the is a good match between numerical and experimental results of the aerodynamic damping coefficient with magnitudes $\Xi = 2.7$ & $\Xi_{exp} = 3.73$, and the obtained magnitude is also in agreement with the numerical results obtained by Arnone et al. and Cinnella et al. The harmonic content at the reference IBPA showed a slight variation of $\tilde{c}_p$ between the current results and the references. The current results over predict the amplitude at the PS. At the SS, the highest differences arose from 25% to ≈70% of the chord but the predicted maximum amplitudes are in agreement. Regarding the phase, along the PS the current results does not followed the increase in-phase trend showed experimentally whereas Cinnella et al. results does, but an overall good agreement occurred among all results at the SS. The proportional aerodynamic damping coefficient from each reference have almost the same change per IBPA and the current results is in close match with all references, showing that the normalizing process removes the scaling factor and retrieves the real variation from case to case. The least and most stable cases were chosen based on the data availability, being $\sigma \pm 90$, respectively. At the least stable case, there is a good match among references regarding the harmonic pressure coefficient with a better trend that at the reference IBPA. The highest differences are found in the first quarter of the chord at the SS. For both least and most stable conditions, the phase at the PS from FINE™/Turbo results presents discrepancies in particular after 50% of the chord with respect to the experimental and numerical data, the root cause is unclear but might be related to the wake effect, as the correct trend was only found when the flow was supersonic around the wake as occurred in Case 628. However, as the PS predicts a very small harmonic amplitude, this phase variation does not produce any critical effect. These results can be taken as reliable as they are in agreement with the harmonic content of the multiple reference, and also in magnitude and trend of the proportional aerodynamic damping coefficient. As in all previous cases the maximum amplitude of $\tilde{c}_p$ is found at $25\%c_n$, which in this case correlates to the region in which the Mach number tends to stabilize.

It is also concluded, that as in all cases the maximum $\tilde{c}_p$ amplitude was found at the same location regardless of the operational conditions, it is assumed this correlation is due to the blade geometry. The rate of change of the geometry along the chord, proved that when the slope tends to zero, it corresponds to the 25% of the normalized chord, matching the maximum $\tilde{c}_p$ location. This region, usually correlates to the maximum Mach, but not always as shown in Case 628. It was determined as well that at the phase of the SS, within this region the phase kept almost constant. On a similar basis, the phase at the PS always had a tendency to predict an out-of-phase condition, which is in disagreement with the experimental and numerical references.

Chapter 6

Last stage steam turbine (LSST)

The last stage rotor within a steam turbine are the most slender components which sustain high aerodynamic loads, thus this components are prone to encounter flutter. In this chapter a typical rotor blade of the last stage steam turbine (LSST), located at Durham University, that vibrates on a first mode (bending) is analyzed. This blade has been developed on a theoretical approach as its performance was meant to achieve pure aerodynamic targets as specified by Burton [67]. Nevertheless, it provides a new open source as a reference test case on a 3D geometry with available numerical results. This reference geometry has been assessed by Qi et al.[49], Sun et al. [48], and Fuhrer and Vogt [50]. Among these three numerical reference cases, there is a discrepancy in tip gap, imposed maximum physical displacement and number of blades. Thus, the reference that will be used to be compared within this chapter is Sun et al. as it contains results from two solvers, being able to provide a valuable comparison. The main layout of the stage is found in Figure 6.1. The stage consists on a stator, rotor and a diffuser downstream the rotor. For this current analysis, the three domains are merged into two, the first corresponds only to the stator, the second to the rotor and diffuser. Therefore both domains are in the relative reference frame as specified by Burton and Sun et al. This configuration, allows a simplification of the domain by reducing the possible mixing interaction between rotor and diffuser.

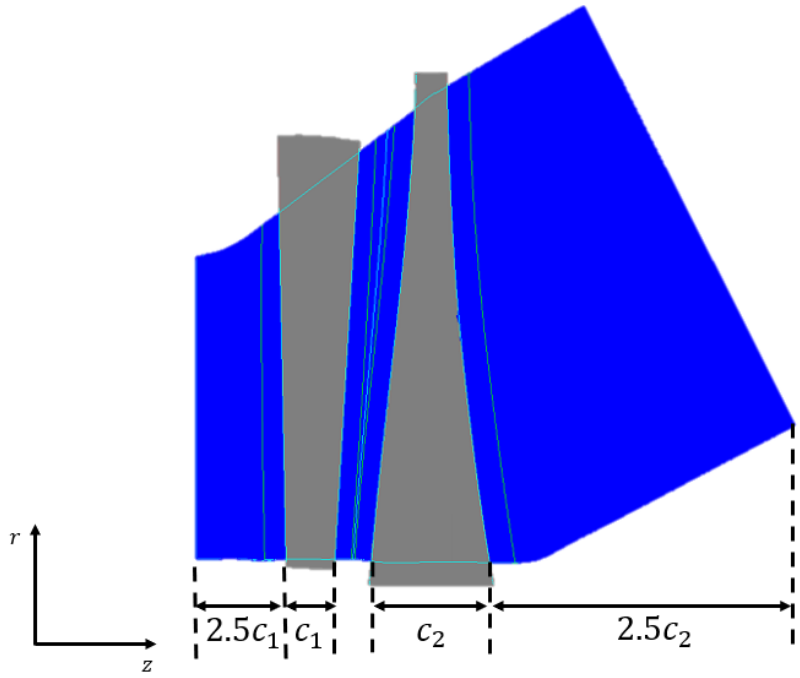

Figure 6.1: LSST: Domain layout

The geometrical characteristics of the stage are described in Table 6.1, its corresponding boundary conditions are retrieved from [68] that provides a detailed variation along the span regarding total pressure, total temperature, circumferential and radial angles. The mean boundary conditions at this operating point are shown in Table 6.2. Additionally, this provides a benchmark from FINE™/Turbo to be compared with different solvers, as this case provides steady and unsteady numerical results from an harmonic balance solutions from a commercial solver (CFX™), and a Linearized Unsteady Flow solver for Turbomachinery (LUFT), with $k-\epsilon$ and Spalart-Allmaras as turbulence models, respectively. The fluid within this section is assumed to be a perfect gas, with a specific heat ratio coefficient of 1.2, a specific heat at constant pressure of $c_p = 4153 J/kgK$ and a dynamic viscosity of $\mu = 1.032E-05\ Pa \cdot s$ which as been proven as a good approximation of the hot steam at the last stage turbine [69].

N_{stator} [-]	60
N_{rotor} [-]	65
H [m]	0.92
Ω [RPM]	3000
γ_{tip} [°]	67
c_{tip} [m]	0.17
h_{gap}[mm]	2.3
f [Hz]	132.08
u [mm]	2.05

Table 6.1: LSST: Stage description

P_{t_1} $[kPa]$	266
T_{t_1} $[K]$	339
α_1 [°]	-0.41
Θ_1 [°]	14
P_2 $[kPa]$	8.8

Table 6.2: LSST: Mean boundary conditions

6.1 Steady state results

6.1.1 Mesh independence

The geometry to be evaluated is a last stage turbine with a tip gap of 2.3 mm which corresponds to 0.25% of the blade span. Thus, a mesh independence study was performed for the stage to determine a trade-off between CPU cost and accuracy. The compared reference property is the static pressure over the rotor blade at two different span heights. These heights represent an imaginary shroud intersection with the blade which is described by a linear combination of the axial position and the desired span percentage shown in Equation 6.1 [49]. It includes the shroud gradient, span height, and axial location, K, $X\%$, and Z, respectively. Where K varies linearly from 0 to 0.577, as a function of the percentage of the span.

$$r = 0.713[m] + KX\%(Z + 1.102[m]) \tag{6.1}$$

Three meshes were evaluated within this subsection: Coarse, Medium and Fine. The mesh characteristics so as the output of the physical properties of the stage are shown in Table 6.3. The variation of y^+ among the three meshes is small because all of them have a first wall height of 0.1mm specified by the mesh reference in [49]. The maximum variation in physical properties from Coarse, Medium and Fine meshes is around 0.5%, which can be assumed negligible. Therefore from this result, it could be assumed that even the Coarse mesh would produce reliable results.

	Mesh 1 Coarse	Mesh 2 Medium	Mesh 3 Fine
Number of points [$1E6$]	≈ 1.3	≈ 2.6	≈ 4.5
y^+	0.60 - 13.18	0.61 - 15.85	0.58 - 13.31
Span wise points	45	73	109
Efficiency [%]	91.96	92.72	92.31
Torque $[kN \cdot m]$	-3.663	-3.661	-3.669
Thrust $[kN]$	4.818	4.820	4.835
Mass flow $[kg/s]$	86.85	86.87	86.87

Table 6.3: LSST: Mesh independence results

However, the static pressure variation was analyzed in order to determine if in fact the Coarse mesh could be used as reference or not. Thus, the steady comparison was taken at a span height $X\% = 50$ & $X\% = 90$. Figure 6.2 shows the variation of the static pressure for the three different meshes. Sub figure 6.2a shows a slight difference in the Coarse mesh at $\approx$ 0.49m along the suction side. Sub figure 6.2b also shows a slight variation of results along the SS at $\approx$ 0.435m and 0.465m. The shown variations are small compared with the results from other meshes but, as the results from Fine and Medium are almost the same, it is concluded that by using a Medium mesh it is guaranteed that there will not be any difference in results. Therefore a Medium mesh was selected.

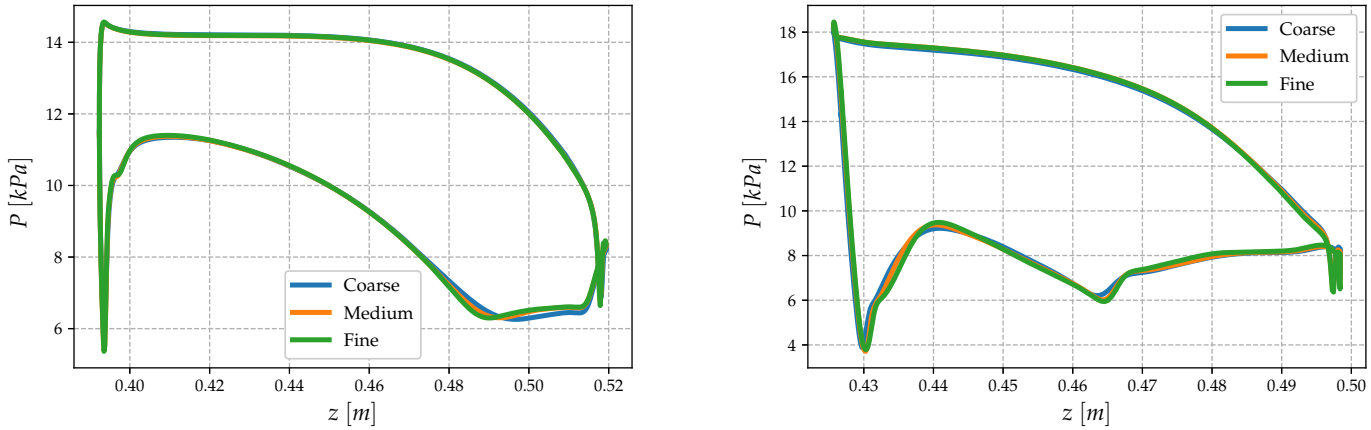

(a) LSST: Static Pressure at 50% span comparison

(b) LSST: Static Pressure at 90% span comparison

Figure 6.2: LSST: Mesh independence of static pressure comparison at different span heights

The results from the Medium mesh were used as reference to compare numerical results from the different software. Figure 6.3 displays the static pressure variation among the reference data at 50% and 90% span. Sub Figure 6.3a displays a good static pressure agreement along the PS at 50% span from the three cases, despite the fact that LUFT results were only available without tip gap. However, clear difference among results arose at the SS, in particular at the stagnation point and close to the trailing edge. In the former location, LUFT did not capture the lower static pressure however it is assumed that is due to a mesh refinement as the nearby region outside the stagnation point matches with the remainder results and a similar trend is found in CFX™. At the trailing edge FINE™/Turbo presented a quick static pressure increase, and as the flow is already supersonic this is consistent with a normal shock wave occuring

before the trailing edge. The shock predicted by LUFT is slightly shifted towards the trailing edge whereas CFX™ shows a full steep variation which is a characteristic of a fish tail. Therefore, the shock location varies from software to software. Figure 6.3b shows the static pressure variation at 90% of the span. At this region a similar trend as at 50% of the span is found, where there is a good agreement among results at the pressure side. A clear difference appeared at the SS in particular with LUFT solver, as the effect of the tip gap on the static pressure was stronger. At the SS close to the stagnation point there is a normal shock wave in which CFX™ predicts a higher increase in static pressure in an almost linear trend, the increase in magnitude matches with LUFT results. The second difference region is at $z = 0.465$m where FINE™/Turbo predicts another increase of static pressure which is due to the reflection of the fish tail from the neighbor blade as shown in Figure 6.4.

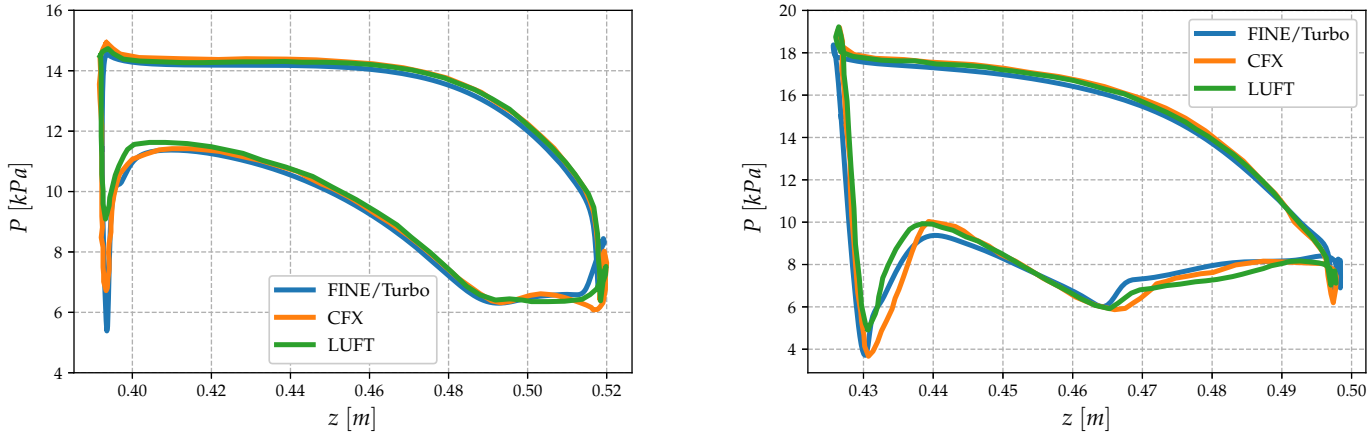

(a) Static Pressure at 50% span comparison

(b) Static Pressure at 90% span comparison

Figure 6.3: LSST: Static pressure comparison at different span heights

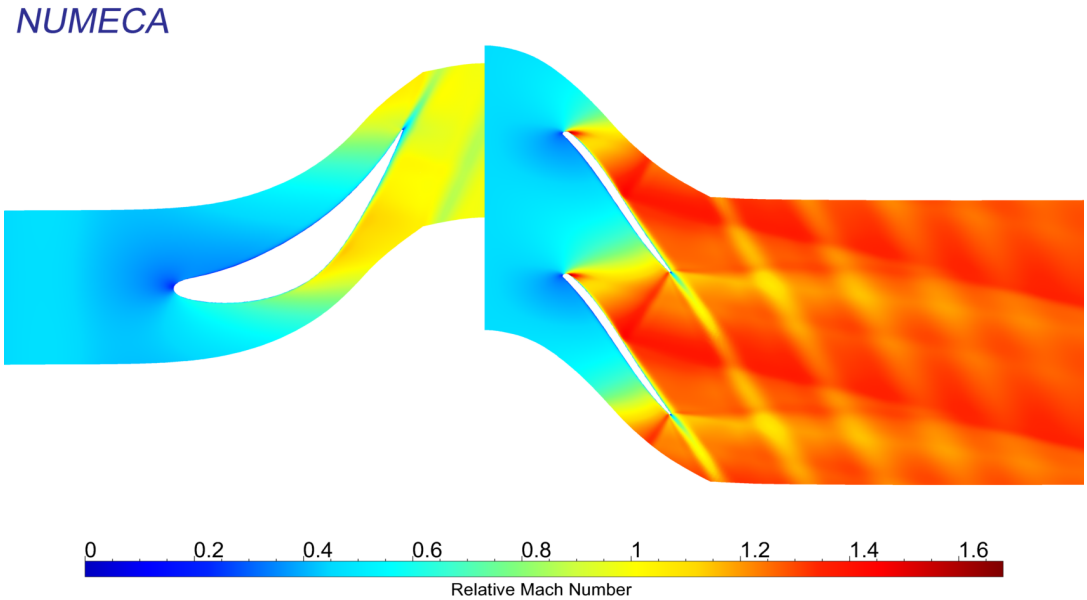

Figure 6.4: LSST: Relative Mach at 90% span

6.2 Unsteady results

It has been proven that, the three solvers provide similar results but with slight physics variations. The variation of shock wave location at 50% of the blade height, the magnitude of normal shock wave and the reflection of the fish tail shock at 90% of the span, might have an effect in the entire stability of the blade as the initial condition is a key factor that affects the aerodynamic damping coefficient.

Despite the differences in steady state results, and as this configuration is a purely theoretical case a full unsteady analysis is performed to assess the differences, if any, on the system stability. The references have only performed an unsteady analysis for this configuration only with the rotor domain. On it, the inlet boundary conditions are set as the outlet conditions from the stator [50] [48]. It is assumed that the number of blades in the rotor was changed, as Sun et al. [48] highlights that an analysis on IBPAs of $\sigma \pm 90°$ & $180°$ were performed. Nevertheless, none of this IBPAs can produce a periodic trend for an odd number of blades (65 blades in rotor). Additionally, Fuhrer & Vogt modified the number of blades in the rotor to match the stator ones. However, this is a numerical tweak that is reproducing results that do not correlate with the physical machine. Therefore, in this thesis no modification of the number of blades was done and just a readjustment of the IBPAs to guarantee a periodic condition after a full revolution. It is from the author's knowledge that currently there is no open literature regarding a flutter analysis which takes into account the stator-rotor interaction with the actual number of blades of the machine. Thus, this thesis tackles this interaction by making use of the Non-Linear Harmonic method. Finally, for this reference case, the aerodynamic damping coefficient definition is switched to the logarithmic decrement which is shown in Eq.6.2, as specified by Sun et al., in order to be in agreement with the reference data.

$$\Xi = -\frac{\dot{W}_{aero}}{\pi H u^2 f P_{ref}} \tag{6.2}$$

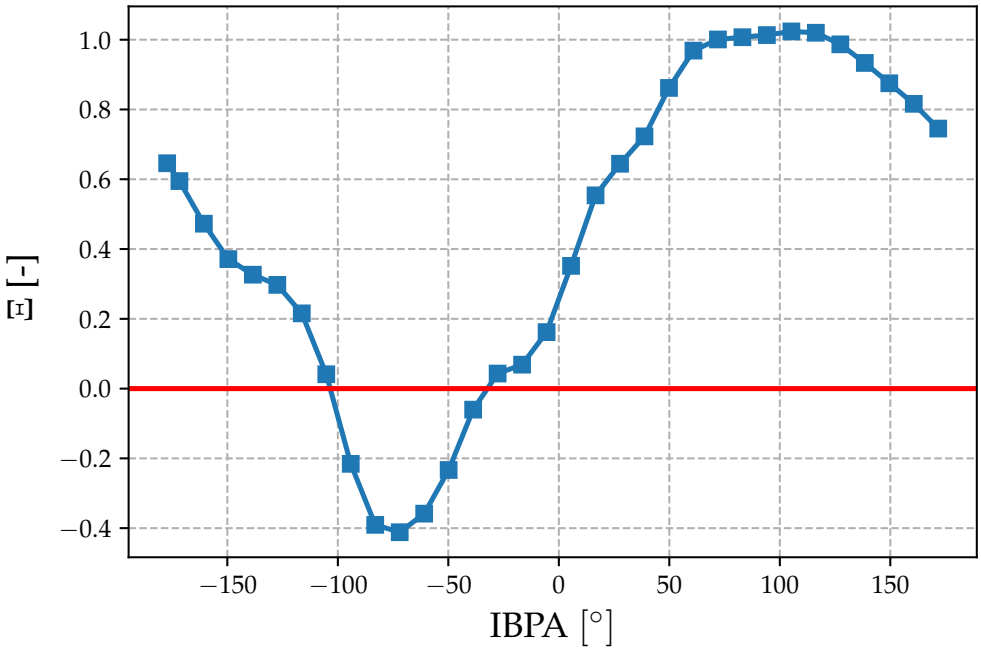

Figure 6.5: LSST: Aerodynamic damping coefficient output from Flutter Wizard tool

Due to time constrain not all IBPAs could be evaluated so just half of them were assessed. The analysis was performed by making use of the flutter wizard tool in which the entire set up took less than 2 minutes and the computation time around 104 hrs. Figure 6.5 shows the post processed aerodynamic power by the logarithmic decrement scaling. With a reference pressure, physical displacement and blade height, $H = 0.92\ m$, $u = 2.05\ mm$ & $P_{ref} = 1938\ Pa$. Six IBPAs cases are proven to be unstable and three more are close to the flutter region in a backward traveling wave. The least stable and most stable modes are at $\sigma = -72°$ & $105.23°$.

Figure 6.6 show the general variation of the aerodynamic damping coefficient by means of the logarithmic decrement among the current results, LUFT, and CFX™. Sub Figure 6.6a displays a relative qualitative agreement between the current results and LUFT, in particular at a backward traveling wave, whereas in the forward differences are clear. On the other hand, Sub Figure 6.6b, shows the proportional aerodynamic damping. In this figure there is a clear agreement between results from LUFT and FINE™/Turbo at both forward and backward traveling waves, where as the commercial software over predicts the magnitudes on a backward traveling wave but tends to produce a different trend on a forward traveling wave.

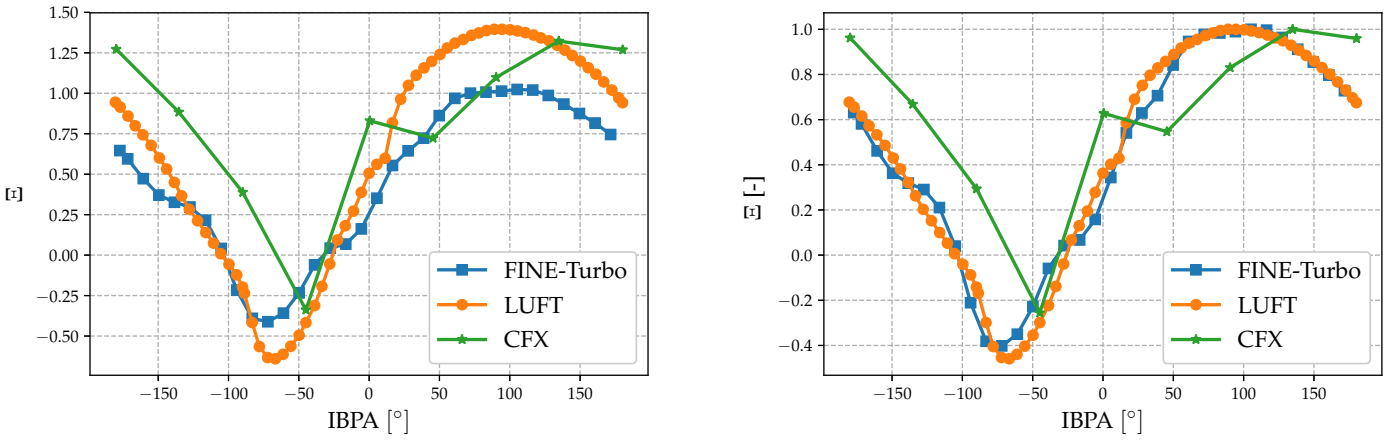

(a) Ξ vs IBPA

(b) Normalized Ξ vs IBPA

Figure 6.6: LSST: Aerodynamic damping stability curve validation

Figure 6.7 displays a comparison of the amount of the aerodynamic power per unit area that are generated at the two different reference blade heights for the most and least stable condition. These results are given as a future reference by taking into account the vibration of the blade, the blade passing frequency of the blade with respect to the rotor and the influence from one another. Sub Figure 6.7a, show that the area covered by the most stable case is smaller but most of the area is on a negative power, which will produce stability. On the other hand, the least stable shows a higher sweep area but the integral over the selected area would produce an unstable condition. This trend is also found in Sub Figure 6.7b, but the scaling variation is by one order of magnitude. This is because as the highest modal displacement occurs towards the tip, producing a higher work. Also, close to the tip the flow filed has a strong influence by the blade tip gap, affecting the aerodynamic forces. Thus, it is assumed that the combination of increase in modal displacement and aerodynamic forces produce the rise of one order of magnitude at 90% span.

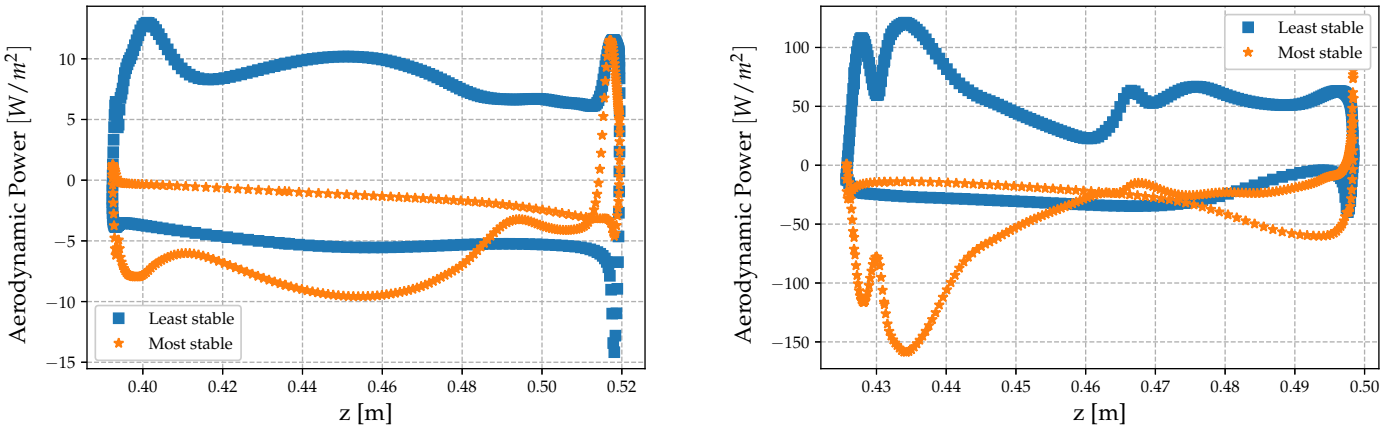

(a) LSST: Aerodynamic power per unit area at 50% span (b) LSST: Aerodynamic power per unit area at 90% span

Figure 6.7: LSST: Aerodynamic power per unit area at different span locations

Furthermore, an additional case was performed in which the number of blades from the rotor was modified ($N_{rotor} = 60$) to be able to compare the results from a NLH method to the references. The selected reference case is at an inter blade phase angle of $-90°$ at 90% of the blade span, and the compared property is the aerodynamic work coefficient as shown by Sun [48]. However, there is no detailed description of the methodology used within the paper regarding how the blade was modified, nor the number of harmonics used within the harmonic balance method from CFX™. The results from this additional case are meant to have a reference contrast from a time domain, harmonic balance and non linear harmonic methods. This case was run without taking into account the effect of the blade passing frequency, leading to just the effect of the vibrating rotor blade. The results are compared in Figure 6.8 with respect to the commercial and in-house solver.

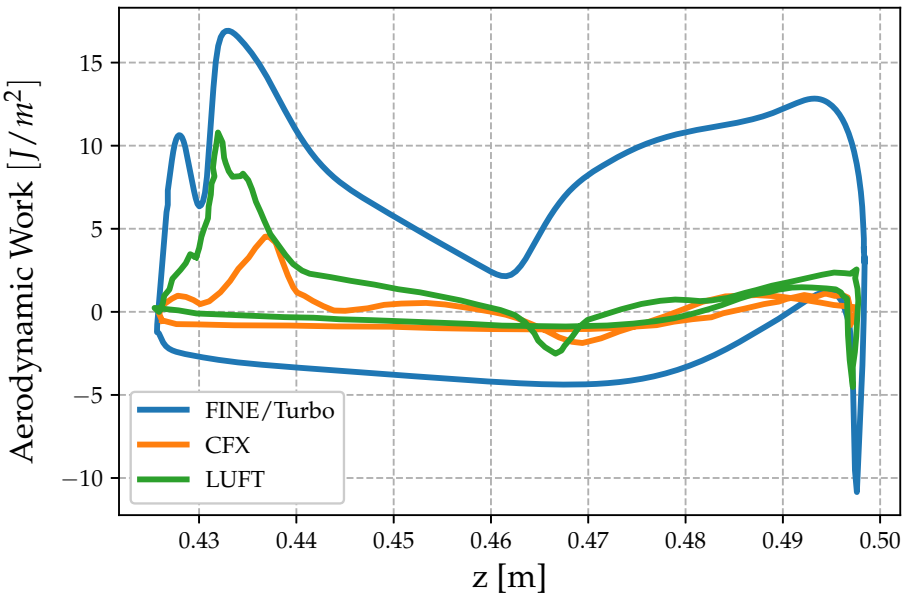

Figure 6.8: LSST: Aerodynamic work coefficient at 90% span comparison

A clear difference in magnitude is observed among the results. In general, all software predict that the suction side would have the highest contribution to the instability of the system, as a remainder all magnitudes above zero would feed energy into the system. FINE™/Turbo show a higher unstable area, in particular towards the trailing edge which might be due to the tip leakage effect. Along the suction side, the valleys correlate with regions of the lowest static pressure from the steady state results on the current results. These regions do not occur on the other two numerical references. LUFT results have a relative trend agreement with the current results, but with lower magnitude. This variation is assumed to occur because LUFT case did not have a blade tip gap, which in fact does not represent the physical machine, which would reduce the aerodynamic forces as no tip leakage vortex is occurring.

Thus, there is a window of opportunity to standardize this reference case in a more robust manner in order to compare in greater detail its corresponding aerodynamic work coefficient and furthermore, its harmonic content as it has been proven in Chapter 5 that it provides a higher insight within the flow physics. Figure 6.9 shows the harmonic content only on the rotor for its least and most stable cases, $\sigma = -72° \ \& \ 105.23°$, respectively. This was applied on the full stage configuration without any modification of the number of blades on the rotor, as it represents the physical machine. Sub Figure 6.9a shows that the amplitude of the harmonic content varies slightly from the most and least stable conditions. The first quarter of the suction side is producing the highest harmonic content whereas, the pressure side has in general the smallest contribution. The phase, shown by sub Figure 6.9b, displays the highest effect on the stability of the system as the least stable condition is highly in-phase where as the most stable is out of phase. At the PS, the least stable case has a high out of phase content but it does not have a strong effect on the global stability as the harmonic content in this region is small, which lead to a small amplitude projection in the global aerodynamic damping coefficient. This conclusion is in agreement with results from sections 5.2.2 to 5.2.5.

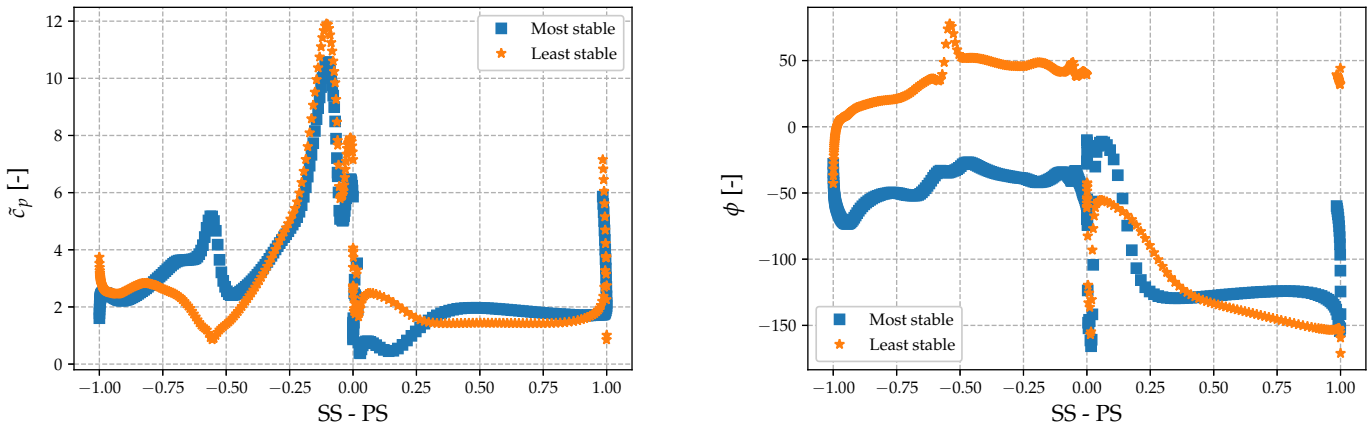

(a) $\tilde{c}_p$: $\sigma = -72° \ \& \ 105.23°$

(b) ϕ: $\sigma = -72° \ \& \ 105.23°$

Figure 6.9: LSST: Harmonic content of least and most stable conditions

The above harmonic content results, are left as a reference if any further numerical data is desired to be compared with. As this is a pure numerical case, trends and magnitudes are of great interest, however it is highly suggested that in order to have a concrete reference target, it is required reliable experimental data to determine which numerical result is actually representing with higher accuracy the unsteady phenomena. This is without a doubt a full project that would contribute to the aeroelasticity community within turbomachinery, that up to date is not abundant in open experimental data.

6.3 Chapter conclusion

A flutter analysis by the energetic method was performed on a typical last stage steam turbine by making use of the flutter wizard tool. The reference case was compared against two open source numerical results from an in-house solver LUFT and a commercial software CFX™ at two rotor blade heights, 50% & 90%. The former uses Spalart-Allmaras as turbulence model whereas the latter $k-\epsilon$, and all cases have the same mesh wall distance of 0.1 mm. A blade tip gap was set to 2.3 mm for this configuration, with a physical displacement of 2.05 mm. LUFT configuration only provides results for a no gap configuration. Regarding the steady state results, there is a general good agreement among software with two main differences in the reference data. At 50% of the span FINE™/Turbo and LUFT results predict a normal shock wave before the trailing edge, whereas CFX™ display a clear fishtail shock. At 90 % span there is a slight difference in the prediction of the shock at the leading edge and at the reflection of the oblique fish tail over the suction side but all cases have a good agreement in the static pressure at the trailing edge.

Despite the flow physics differences, an unsteady analysis was carried out to be compared with the reference software. However, the machine configuration has been modified by the reference data in order to perform an harmonic balance model. This change in configuration most certainty does not represent the actual machine. The current results do not modify the machine blades number, and thus there is a clear difference in analyzed IBPAs. The system was analyzed for half possible IBPAs due to time constrains by the flutter wizard, with a set up time of less than 2 min and a running time of $\approx$ 104 hrs with five processors. The retrieved aerodynamic damping coefficient curve showed a close match between both references but not quite. However, when the proportional aerodynamic power variation per IBPA was compared among results, an almost full match was obtained between FINE™/Turbo and LUFT, in particular on a forward traveling wave. At all IBPAs on a backward traveling wave CFX™ over predicts the stability and on a forward traveling wave there is no clear trend from this software. Therefore, the current results obtained with FINE™/Turbo, thanks to the Non-Linear Harmonic and FSI, can be taken as a benchmark to evaluate this LSST without any modification.

A further reference case was performed by modifying the number of rotor blades to 60, and the aerodynamic work coefficient at 90% of the span at $\sigma = -90°$ was compared among the three software. All software, predict that the suction side contributes to the instability of the system. LUFT showed a similar trend to the current results but by under predicting its magnitude, which is assumed to occur due to the lack of tip leakage on LUFT case. FINE™/Turbo predicts that a great contribution of instability also rises towards the trailing edge along the suction side, which is also assumed to be occurring due to the tip leakage vortex strength. Finally, the harmonic content over the rotor without any modification on its blades number was analyzed and left as future reference for further numerical comparison. The amplitude of the harmonic content did not have a strong variation between the least and most stable IBPAs, $\sigma = -72°$ & $105.23°$, respectively. The highest amplitude occurred during the first quarter of the suction side. However, the key driver for stability is determined by the phase in which in general the most stable case showed a high out of phase angle, whereas the least a high in-phase angle in particular at the suction side. As this is a pure numerical case, it is required more reference data that does not affect the machine characteristics, and takes into account the full stage. However, in order to have a concrete reference target, it is required reliable experimental data to determine which numerical result in the future is actually representing with higher accuracy the unsteady phenomena. This is a full project that would contribute to the aeroelasticity community within turbomachinery, that up to date is not abundant in open experimental data.

Chapter 7

Conclusions

Flutter is a self-excited and self-sustained vibration within an elastic structure that up to date can not be fully foresee within the design of a turbomachine. Flutter is determined by the sign of the aerodynamic power of the system, where a positive value represents an energy feed from the unsteady aerodynamic forces into the vibrating structure producing an unstable condition. There is no standard method to retrieve the aerodynamic damping of the system as it is just a scaling factor of the aerodynamic power. However, Fransson & Bölcs method has been selected as it is used in eleven Standard Configurations and is up to date employed to validate results. In order to guarantee a safe operational condition of the turbomachine, all possible design and off-design conditions must be evaluated, which produce a quick increase in the engineering and computational time.

The engineering time drawback, was satisfied by the development of a flutter wizard tool with Python 2.7 within FINE™/Turbo by producing reliable flutter results automatically. The wizard, has been designed to be flexible and user-friendly, by allowing the set up of particular cases, if desired. The tool works for a single or multiple row configuration, for a single or multiple operational conditions in which only one row has an imposed motion. The tool works with a Non-Linear Harmonic method and sets up one harmonic and one perturbation as flutter in turbomachinery occurs in a single mode. The generalized displacement is retrieved from the imposed modal displacement and is set to be proportional to 0.5% of the blade tip chord by default. The parameter that is changed every time by the tool is the inter blade phase angle to analyze all possible periodic vibration modes. Two cases have been implemented within the wizard, case A & B. Case A has been designed to start from a steady state computation, whereas case B is meant to start from a given harmonic unsteady computation in case any particular set up is required. Case B was used for six operational conditions and case A for one within this thesis. A strong reduction in engineering time was achieved by the development of the wizard. For a single row turbine consisting of twenty blades, the engineering time by making use of the wizard was less than 1.5% of the time required without it.

The wizard provides between two and three outputs, depending on the number of computations given as inputs. Thus, it is possible to impose a full compressor map or just a single operational point. The first output is a **_Aerodamping_stability.dat* file, which contains all the physical properties to recover the aerodynamic damping coefficient such as generalized displacement, physical displacement, reference pressure, among others. It also includes the aerodynamic power obtained from each unsteady computation, in case the user desires a different scaling factor. From this file the aerodynamic damping coefficient is plotted against its available inter blade phase angle and saved for the user with a **_Aerodamping_stability_curve.png* format. The third output is generated in case multiple operational conditions are selected. It corresponds to a flutter stability map, which relates the pressure ratio and mass flow of each

operational point with its corresponding stability status with a **_Flutter_stability_map.png* format.

A full flutter analysis of six operational conditions from two turbine Standard Configuration cases (STCF11 & STCF4) have been analyzed in FINE™/Turbo with Spalart-Allmaras as turbulence model. These configurations represent a twenty bladed non-rotating turbine. The blades are assumed to be vibrating in a bending mode, and it also includes the motion of the hub. The developed flutter wizard tool was used to set up each case to retrieve automatically the aerodynamic damping coefficient curve, which provided a clear assessment of the global flutter stability per case. For all cases the set up time was around 45 seconds, with computational time variation due to a different set up per case. In all cases, the imposed motion was assumed to be the modal shape leading to a generalized displacement of 0.5, whereas the specific physical displacement was set to match the reference scaling factor. All analyzed cases were compared first with experimental reliable data in terms of the harmonic content, and then with different references depending on the data availability at the most critical conditions. Steady and unsteady results were obtained at the reference span of 50% against the normalized true chord (c_n) and for unsteady results a reference IBPA of $\sigma = 180°$ was selected. A proportional aerodynamic damping coefficient was generated for each case by normalizing it against its maximum per reference. This proved to remove the scaling factor and retrieve the actual variation of aerodynamic power per IBPA. All unstable conditions predicted by the current results occurred on a backward traveling wave. Additionally, the highest aerodynamic power is encounter towards the blade tip as the blade displacement for the first mode is higher at the tip.

STCF11 was analyzed at high-subsonic (OPC1) and transonic off-design conditions (OPC2), with experimental and numerical reference data. OPC1 had a good agreement at 50% of the span of the isotropic Mach number(M_{iso}) with respect to the experimental data. The wizard was set to a B case, with a physical displacement of 0.42mm at 50% span. The aerodynamic damping coefficient curve predicted an unstable system, with two unstable IBPAs on a backward traveling wave. The least and most stable IBPAs are at $\sigma = -36°$ & $122°$, respectively showing a good agreement at the most stable condition and discrepancies towards the least. There is a good agreement at the reference IBPA of the aerodynamic damping coefficient (Ξ) with a variation of 4.5% with respect to the reference numerical data. The harmonic pressure coefficient ($\tilde{c}_p$), showed a close agreement between numerical and experimental data. The phase along the suction side from the current results had a qualitative agreement but with an underestimation of magnitude. The results are assumed to be reliable as for the least stable configuration the harmonic content, matched the experimental data by also predicting an unstable condition. From a general view, a slight variation in $\tilde{c}_p$ arose, regardless of the IBPA, whereas the phase was proved to be the key parameter that onsets flutter, when a high in-phase condition along the blade is determined. After the maximum steady Mach number of the suction side, there is a tendency of $\tilde{c}_p$ to decrease its magnitude at around 25% of the chord, regardless of the IBPA. Additionally, the peaks of harmonic amplitude close to the trailing edge are assumed to be due to the high wake harmonic content and due to the mesh refinement at this region.

OPC2 contained the most complex steady flow, with a laminar separation bubble at the SS near the leading edge, a reattachment location, and a normal shock wave towards the trailing edge. The current results differ with the reference numerical (FINSUP, Cinnella. et al., and Patil et al.) and experimental data at the reattachment location and normal shock wave. However, the current results are able to capture the maximum Mach number predicted experimentally, whereas none of the references did. It is assumed that the numerical references modified the outlet static pressure to some degree, as the shock location is governed by the outlet pressure. This case showed three flutter regions on a backward traveling wave, its least and most stable cases at $\sigma = -54°$ & $122°$, respectively with a physical displacement of 0.27mm at 50% of the span. FINSUP reference solver have the same maximum and minimum prediction as the

current results, whereas the remainder software displayed a different trend towards the least stable condition. At the reference IBPA, the current results are in agreement with the reference data as, the predicted aerodynamic damping coefficient is $\Xi = 6.32$ and an harmonic balance reference solver was around 8.9. At this IBPA, the amplitudes along the first quarter of the SS show a high difference between results, which corresponds to the laminar bubble separation region. At regions in which the shock wave occurred, there was an increase in $\tilde{c}_p$. Regarding the phase, there is a high differences among results in particular at the SS; at PS the current results were the only ones predicting an almost constant phase and do not match with the experimental data, however the root cause of this trend is unknown. The recovered proportional aerodynamic damping showed a good agreement among results but only before $\sigma = 144°$, after this IBPA Cinnella et al. results are clearly different. It is suggested that further numerical data needs to be compared against this specific case as due to its complexity there is high variation of harmonic content, in particular at the phase. Nevertheless, the unstable regions predicted in this thesis are assumed to be reliable as at the least stable condition the harmonic content matches with the experimental data.

Regarding STCF4, four cases were assessed: Case 624, 627, 628 & Annex 5. The first three cases were compared only against experimental data and the fourth against numerical and experimental references. Case 624 is a transonic flow with an outlet $M_{iso} = 1.04$, with a close match against experimental data with a normal shock wave at $\approx 85\% c_n$. The flutter wizard predicts seven unstable conditions, meanwhile the reference data also shows seven, but it does not have an harmonic behavior. If the harmonic behavior would be recovered, nine experimental unstable cases would occur. The least and most stable conditions exist at $\sigma \pm 72°$ with a blade vibration frequency $f = 149\ Hz$ and a physical displacement $u = 0.3\ mm$ at 50% span. These critical IBPAs match only on the most stable condition against the experimental data. Quantitative differences of Ξ between numerical and experimental results took place ($\Xi = 10.16$ & $\Xi_{exp} = 3.4$), but there is a close match of $\tilde{c}_p$ with clear differences in phase at the PS that are producing a higher aerodynamic damping. The least stable condition was updated to be $\sigma = -90°$ due to a non-harmonic behavior from the experimental data. The overall proportional variation of Ξ for all IBPAs showed a trend disagreement on a backward traveling wave but a better agreement on a forward traveling wave. The highest variation from case to case was at the phase, showing its high impact on the system stability and in all cases the suction side is the region that produce the highest contribution of harmonic content. Regardless of the IBPA, the normal shock wave produced an increase of $\tilde{c}_p$ and a local change of phase, in the opposite direction as the phase before the shock.

Case 627, is a high subsonic flow with an outlet $M_{iso} = 0.85$. The steady state results at the reference blade height are in very good agreement with experimental data. Around half of the chord along the suction side has an almost constant Mach ≈ 0.9. The flutter wizard, had the same blade vibration, physical displacement and generalized displacement as Case 624, and it predicted eight unstable region whereas the reference data, seven. The most and least stable conditions are at $\sigma = -72°$ & $90°$, respectively. Only the least stable condition match with the experimental data, experimentally the most stable is at $\sigma = 126°$. At $\sigma = 180°$, there is an agreement of the aerodynamic damping coefficient, $\Xi = 13.06$ and $\Xi_{exp} = 10.52$. Regarding the harmonic content, the phase showed an almost constant value, which correlates the fact that the flow is almost constant but this trend does not match with experimental data. The increase in $\tilde{c}_p$ amplitude at the trailing edge was vanished at the PS at the most stable condition, but the amplitude at the TE of the SS was increased, showing that the IBPA can affect the wake. The recovered proportional aerodynamic damping variation showed a closer trend between the results on a the backward traveling wave, by removing the scaling factor but, with high discrepancies at $\sigma = 36°,\ 54°$ & $72°$. Regardless of the IBPA, the maximum $\tilde{c}_p$ was located at 25% of the normalized chord, which might be correlated to the location when the maximum Mach number is reached.

Case 628, is a supersonic flow condition with an outlet $M_{iso} = 1.42$, and a general agreement at the reference blade height with experimental data. However, the differences are located at the predicted maximum Mach at the trailing edge and the influence of the reflection oblique shock from the fish tail. The flutter wizard tool predicted four unstable IBPAs, meanwhile the experimental data predicts seven. The least and most stable conditions are taking place at $\sigma = -54°$ & $108°$, respectively with the blade vibration frequency of $f = 152\ Hz$ and the same physical displacement as Case 624 and 627. The experimental data predicted the critical conditions at $\sigma \pm 90$, showing slight disagreement on the critical IBPAs. Quantitative differences in Ξ were obtained at the reference IBPA, $\Xi = 18.2$ to $\Xi_{exp} = 7$. Regarding $\tilde{c}_p$, the peak increase due to the shock reflection is not captured numerically, but the sudden increase found at the TE of the PS is fully vanished. This effect is assumed due to a steady state flow field, in specific due to fish tail shock that produces a steep change in Mach number at the trailing edge. Regarding the phase, along the SS the current results display an out of phase condition whereas numerical predict a high in-phase, which is assumed to be as the variation occurs on the limit of the continuity of the phase definition. As the phase and harmonic amplitude product is producing an unstable condition by the experimental data, it is assumed that the provided data is not the only one used for obtaining the full blade stability. The proportional aerodynamic damping coefficient, presents a clear difference in trend on a backward traveling wave. At the least and most stable conditions, the harmonic amplitude showed good agreement in general except at the first quarter of the SS, in which the numerical amplitude was under predicted. The reflection shock predicted a local change in phase towards the opposite condition before the shock, which occurs similarly by the reflection shock. Regardless of the IBPA, the maximum $\tilde{c}_p$ was encounter at 25% of the chord along the SS, but its root cause is uncertain.

Annex 5, results were compared against the experimental data and three numerical references from literature (Cinnella et al. and Arnone et al.), this case has a high transonic flow with $M_{iso} = 0.9$ at the outlet. Steady state results at the reference blade height conclude a good agreement with all other references and in particular with the experimental data. Along the SS there is an almost constant Mach for $\approx$ 40% of the chord. The flutter wizard predicted eight unstable cases, on a backward traveling wave as in all previous analysis, with a blade vibration frequency $f = 150\ Hz$ and a physical displacement $u = 0.22\ mm$ at 50% span. At the reference IBPA, the aerodynamic damping coefficient has a close agreement against experimental results ($\Xi = 2.7$ & $\Xi_{exp} = 3.73$) and by the different numerical references. Regarding the $\tilde{c}_p$, the current results over predict the amplitude at the PS. At the SS, the highest differences occurred from 25% to $\approx$70% of the chord but the predicted maximum amplitudes are in agreement. Regarding the phase, along the PS the current results does not followed the increase in-phase trend showed experimentally, whereas Cinnella et al. results does. There is a general overall good agreement at the phase from the SS. The multiple references and the current results showed the same variation of the proportional aerodynamic damping, showing that the normalizing process removes the scaling factor and retrieves the real variation from case to case. The least and most stable cases were chosen based on the available data, being $\sigma \pm 90$, respectively, and due to the few amount of experimental data it is not possible to determine if they actually correspond, or not, to the least and most stable cases. At the least stable case, there is a close match among references regarding the harmonic pressure coefficient with a better trend that at the reference IBPA. The highest differences are found in the first quarter of the chord along the suction side. The least and most stable conditions from the current results, showed differences in the phase along the pressure side in particular after 50% of the chord with respect to the experimental and numerical data. However, as the PS predicts a very small harmonic amplitude, this phase variation does not produce any critical effect. The root cause is unclear but might be related to the wake effect, as the correct trend was only captured when the flow around the wake was supersonic (Case 628). These results can be taken

as reliable as they are in agreement with the harmonic content of the multiple reference with a close agreement in magnitude and trend on the normalized aerodynamic damping. The maximum amplitude of the harmonic content occurred always at 25% of the normalized chord, regardless of the operational conditions. It is assumed that the blade geometry plays an important role to determine the location of the maximum harmonic amplitude. The derivative of the geometry profile tends to zero occurs at $\approx 25\% c_n$, in which relates with the maximum harmonic amplitude. This region also matches in some cases with the maximum Mach number is achieved, so it can be predicted at which point in the chord there might be the highest harmonic content. On the other hand, the phase at the PS always had a tendency to predict an out-of-phase condition, which is in disagreement with the experimental and numerical references and its root cause might be related to the wake diffusion as it only occurs on Case 628, where a supersonic flow surrounds the wake.

The final case was a open source typical last stage steam turbine (LLST) with a tip gap of 2.3 mm, which contained two open source numerical results from an in-house solver LUFT and a commercial software CFX™ at two rotor blade heights, 50% & 90%. The former uses Spalart-Allmaras as turbulence model whereas the latter $k - \epsilon$, LUFT configuration only provides results for a no gap configuration. Regarding the steady state results, at 50% of the span FINE™/Turbo and LUFT results predict a normal shock wave before the trailing edge, whereas CFX™ display a clear fishtail shock. At 90 % span there is a slight difference in the prediction of the shock at the leading edge and at the reflection of the oblique fish tail over the suction side but all cases have a good agreement in the static pressure at the trailing edge. Despite the flow physics differences, an unsteady analysis was carried out to be compared with the reference software, with a physical displacement $u = 2.05\ mm$. The current results do not modify the machine blades number, producing a different IBPAs and thus there is a clear difference in analyzed IBPAs. The proportional aerodynamic power variation per IBPA was compared among results, an almost a full match was obtained between FINE™/Turbo and LUFT, in particular on a forward traveling wave. At all IBPAs on a backward traveling wave CFX™ over predicts the stability and on a forward traveling wave there is no clear trend from this software. Therefore, the current results obtained with FINE™/Turbo, thanks to the Non-Linear Harmonic and FSI, can be taken as a benchmark to evaluate this LSST without any modification. Finally, the harmonic content over the rotor without any modification on its blades number was analyzed and left as future reference for further numerical comparison. The amplitude of the harmonic content did not have a strong variation between the least and most stable IBPAs, $\sigma = -72°$ & $105.23°$, respectively. The highest amplitude occurred during the first quarter of the suction side. However, the key driver for stability is determined by the phase in which in general the most stable case showed a high out of phase angle, whereas the least a high in-phase angle in particular at the suction side. As this is a pure numerical case, it is required more reference data that does not affect the machine characteristics, takes into account the full stage. However, in order to have a concrete reference target, it is required reliable experimental data to determine which numerical result in the future is actually representing with higher accuracy the unsteady phenomena, which would enrich the aeroelastic community in turbomachinery.

Bibliography

[1] K Yusuf Billah and Robert H Scanlan. "Resonance, Tacoma Narrows bridge failure, and undergraduate physics textbooks". In: *American Journal of Physics* 59.2 (1991), pp. 118–124.

[2] IE Garrick and Wilmer H Reed III. "Historical development of aircraft flutter". In: *Journal of Aircraft* 18.11 (1981), pp. 897–912.

[3] Oddvar Bendiksen, Robert E Kielb, and Kenneth C Hall. "Turbomachinery Aeroelasticity". In: *Encyclopedia of Aerospace Engineering* (2010).

[4] AR Collar. "The expanding domain of aeroelasticity". In: *The Aeronautical Journal* 50.428 (1946), pp. 613–636.

[5] IE Garrick. "A survey of aerothermoelasticity". In: (1963).

[6] F Holzinger et al. "Self-excited blade vibration experimentally investigated in transonic compressors: Rotating instabilities and flutter". In: *Journal of Turbomachinery* 138.4 (2016), p. 041006.

[7] JD Jeffers and CE EECE. "F100 fan stall flutter problem review and solution". In: *Journal of Aircraft* 12.4 (1975), pp. 350–357.

[8] T Fransson. *Aeroelasticity in axial flow turbomachines*. Tech. rep. Von Karman Inst. for Fluid Dynamics, 1999.

[9] AV Srinivasan. "Flutter and resonant vibration characteristics of engine blades". In: *TRANSACTIONS-AMERICAN SOCIETY OF MECHANICAL ENGINEERS JOURNAL OF ENGINEERING FOR GAS TURBINES AND POWER* 119 (1997), pp. 742–775.

[10] Damian Vogt. "Experimental investigation of three-dimensional mechanisms in low-pressure turbine flutter". PhD thesis. 2005.

[11] Denis Besnard, David Greathead, and Gordon Baxter. "When mental models go wrong: co-occurrences in dynamic, critical systems". In: *International Journal of Human-Computer Studies* 60.1 (2004), pp. 117–128.

[12] AV Srinivasan, DG Cutts, and S Sridhar. "Turbojet engine blade damping". In: (1981).

[13] Albert Kammerer and Reza S Abhari. "The Cumulative Effects of Forcing Function, Damping, and Mistuning on Blade Forced Response in a High Speed Centrifugal Compressor With Inlet Distortion". In: *Journal of Engineering for Gas Turbines and Power* 132.12 (2010), p. 122505.

[14] Wilfred Campbell. *Protection of steam turbine disk wheels from axial vibration*. General electric Company, 1924.

[15] JG Marshall and M Imregun. "A review of aeroelasticity methods with emphasis on turbomachinery applications". In: *Journal of fluids and structures* 10.3 (1996), pp. 237–267.

[16] Matthew Montgomery et al. "Application of Unsteady Aerodynamics and Aeroelasticity in Heavy-Duty Gas Turbines". In: *ASME Turbo Expo 2005: Power for Land, Sea, and Air*. American Society of Mechanical Engineers. 2005, pp. 635–649.

[17] F Sisto. *AGARD Manual on Aeroelasticity in Axial-Flow Turbomachines, Vol. 1 of*. Tech. rep. AGARD-AG, 1987.

[18] Kuen-Bae Lee, Mark Wilson, and Mehdi Vahdati. "Numerical study on aeroelastic instability for a low-speed fan". In: *Journal of Turbomachinery* 139.7 (2017), p. 071004.

[19] Parthasarathy Vasanthakumar. "Computation of aerodynamic damping for flutter analysis of a transonic fan". In: *ASME 2011 Turbo Expo: Turbine Technical Conference and Exposition*. American Society of Mechanical Engineers. 2011, pp. 1429–1437.

[20] Yaoguang Zhai, Ronnie Bladh, and Göran Dyverfeldt. "Aeroelastic stability assessment of an industrial compressor blade including mistuning effects". In: *Journal of Turbomachinery* 134.6 (2012), p. 060903.

[21] Josef Panovsky and Robert E Kielb. "A design method to prevent low pressure turbine blade flutter". In: *ASME 1998 International Gas Turbine and Aeroengine Congress and Exhibition*. American Society of Mechanical Engineers. 1998, V005T14A052–V005T14A052.

[22] M Nowinski and J Panovsky. "Flutter mechanisms in low pressure turbine blades". In: *ASME J. Eng. Gas Turbines Power* 122.1 (2000), pp. 82–88.

[23] Marcello Benvenuto et al. "Sensitivity Analysis to Flutter for Front Stages Compressor Blades". In: *ASME Turbo Expo 2015: Turbine Technical Conference and Exposition*. American Society of Mechanical Engineers. 2015, V07BT34A003–V07BT34A003.

[24] Joshua J Waite and Robert E Kielb. "Physical understanding and sensitivities of low pressure turbine flutter". In: *Journal of Engineering for Gas Turbines and Power* 137.1 (2015), p. 012502.

[25] Tim Rice, David Bell, and Gurnam Singh. "Identification of the stability margin between safe operation and the onset of blade flutter". In: *Journal of Turbomachinery* 131.1 (2009), p. 011009.

[26] Frank Lane. "System mode shapes in the flutter of compressor blade rows". In: *Journal of the Aeronautical Sciences* 23.1 (1956), pp. 54–66.

[27] Damian Vogt. *Structural Dynamics*. Feb. 2009.

[28] A Meldahl. "Self-induced flutter of wings with one degree of freedom". In: *Brown Boveri* (1946).

[29] Damian Vogt. *Damping*. Feb. 2009.

[30] Joseph F Lubomski. "Status of NASA full-scale engine aeroelasticity research". In: (1980).

[31] JJ Adamczyk, ME Goldstein, and MJ Hartmann. "Supersonic unstalled flutter". In: *NASA TM* 79001 (1982).

[32] Frederic J Blom. "A monolithical fluid-structure interaction algorithm applied to the piston problem". In: *Computer methods in applied mechanics and engineering* 167.3-4 (1998), pp. 369–391.

[33] Jean-Marc Vassen et al. "Strong coupling algorithm to solve fluid-structure-interaction problems with a staggered approach". In: *7th European Symposium on Aerothermodynamics*. Vol. 692. 2011, p. 128.

[34] David Thomas et al. "Staggered strong coupling between existing fluid and solid solvers through a Python interface for fluid-structure interaction problems". In: *Proceedings of the VII International Conference on Coupled Problems in Science and Engineering*. 2017.

[35] Robert E Bartels and AI Sayma. "Computational aeroelastic modelling of airframes and turbomachinery: progress and challenges". In: *Philosophical Transactions of the Royal Society A: Mathematical, Physical and Engineering Sciences* 365.1859 (2007), pp. 2469–2499.

[36] Vasily Vedeneev, Mikhail Kolotnikov, and Pavel Makarov. "Numerical analysis of compressor blade flutter in modern gas turbine engines". In: *10 th European Conference on Turbomachinery Fluid dynamics & Thermodynamics*. EUROPEAN TURBOMACHINERY SOCIETY. 2013.

[37] U.S. Deparament of Transport Federal Aviation Administration. *Aeroelastic Stability Substantiation of Transport Category Airplanes 25.629-1B*. https://www.faa.gov/documentLibrary/media/Advisory_Circular/AC_25_629-1B.pdf. 2014.

[38] CS25 EASA. *Certification Specifications for Large Aeroplanes CS-25*. 2007.

[39] TH Fransson et al. "Viscous and inviscid linear/nonlinear calculations versus quasi 3d experimental cascade data for a new aeroelastic turbine standard configuration". In: *ASME 1998 International Gas Turbine and Aeroengine Congress and Exhibition*. American Society of Mechanical Engineers. 1998, V005T14A043–V005T14A043.

[40] Peter D Silkowski et al. "CFD investigation of aeromechanics". In: *ASME Turbo Expo 2001: Power for Land, Sea, and Air*. American Society of Mechanical Engineers. 2001, V004T03A031–V004T03A031.

[41] Wei Ning and Li He. "Computation of unsteady flows around oscillating blades using linear and nonlinear harmonic Euler methods". In: *ASME 1997 International Gas Turbine and Aeroengine Congress and Exhibition*. American Society of Mechanical Engineers. 1997, V004T14A039–V004T14A039.

[42] Kenneth C Hall, Jeffrey P Thomas, and William S Clark. "Computation of unsteady nonlinear flows in cascades using a harmonic balance technique". In: *AIAA journal* 40.5 (2002), pp. 879–886.

[43] Stéphane Vilmin et al. "The nonlinear harmonic method: from single stage to multi-row effects". In: *International journal of computational fluid dynamics* 27.2 (2013), pp. 88–99.

[44] MT Rahmati. "Comparison of frequency domain and time-domain methods for aeromechanical analysis". In: *International Journal of Rotating Machinery* 2016 (2016).

[45] Sunil Patil et al. "Investigation of Time/Frequency Domain CFD Methods to Predict Turbomachinery Blade Aerodynamic Damping". In: *ASME Turbo Expo 2016: Turbomachinery Technical Conference and Exposition*. American Society of Mechanical Engineers. 2016, V07BT34A028–V07BT34A028.

[46] NUMECA International. *NUMECA FINE/Turbo and FINE/Design3D 13.2 Theory Guide*. 2019.

[47] François Debrabandere et al. "Fluid–structure interaction using a modal approach". In: *Journal of Turbomachinery* 134.5 (2012), p. 051043.

[48] Tianrui Sun, Paul Petrie-Repar, and Di Qi. "Investigation of tip clearance flow effects on an open 3d steam turbine flutter test case". In: *ASME Turbo Expo 2017: Turbomachinery Technical Conference and Exposition*. American Society of Mechanical Engineers. 2017, V008T29A024–V008T29A024.

[49] Di Qi et al. "Establishment of an open 3d steam turbine flutter test case". In: *12th European Conference on Turbomachinery Fluid Dynamics and Thermodynamics, ETC 2017, Quality Hotel Globe-Stockholm, Sweden, 3 April 2017 through 7 April 2017*. KTH Royal Institute of Technology. 2017.

[50] Christopher Fuhrer and Damian M Vogt. "On the impact of simulation approaches on the predicted aerodynamic damping of a low pressure steam turbine rotor". In: *ASME Turbo Expo 2017: Turbomachinery Technical Conference and Exposition*. American Society of Mechanical Engineers. 2017, V008T29A007–V008T29A007.

[51] Franklin O Carta. "Coupled blade-disk-shroud flutter instabilities in turbojet engine rotors". In: *Journal of Engineering for Power* 89.3 (1967), pp. 419–426.

[52] Joseph M Verdon. "Linearized unsteady aerodynamic theory". In: *In AGARD Aeroelasticity in Axial-Flow Turbomachines*. 1 (1987).

[53] Maria Angelica Mayorca. "Numerical methods for turbomachinery aeromechanical predictions". PhD thesis. Royal Institute of Technology, 2011.

[54] F. Debrabandere. *Computational methods for industrail fluid-structure interactions*. Tech. rep. Faculté Polytechnique de Mons et Numeca International, 2014.

[55] Python org. *Python org*. url: `https://www.python.org/` (visited on 02/11/2019).

[56] NUMECA International. *FINE™/Turbo v13.1, User Manual*. 2018.

[57] Albin Bölcs and Torsten Henry Fransson. "Aeroelasticity in Turbomachines. Comparison of Theoretical and Experimental Cascade Results." In: *ECOLE POLYTECHNIQUE FEDERALE DE LAUSANNE* (1986).

[58] Markus Jöcker. *Information for 3D computations of the STCF11 test cases*. Tech. rep. Report HPT-11/01, Lausanne, EPFL Switzerland, 2001.

[59] P Ott. "Information for 3D computations of the STCF 4 test cases". In: *Lausanne: EPFL* (2002).

[60] Paola Cinnella et al. "A numerical method for 3D turbomachinery aeroelasticity". In: *ASME Turbo Expo 2004: Power for Land, Sea, and Air*. American Society of Mechanical Engineers. 2004, pp. 539–550.

[61] François Debrabandere. "Computational methods for indistrial fluid-structure interactions". PhD thesis. Faculté Polytechnique e Mons et Numeca International, 2014.

[62] L He. "Harmonic solution of unsteady flow around blades with separation". In: *AIAA journal* 46.6 (2008), pp. 1299–1307.

[63] Anupama Aggarwal. *Standard Configurations for Unsteady Flow Through Vibrating Axial-Flow Turbomachin Cascades (STCF)*. url: `%5Curl%7Bhttp://www.energy.kth.se/proj/projects/Markus%20Joecker/STCF/default.htm%7D` (visited on 2019).

[64] NUMECA International. *FINE™/Turbo v13.1, Theory Guide*. 2018.

[65] Andrea Arnone, Francesco Poli, and Claudia Schipani. "A method to assess flutter stability of complex modes". In: *Unsteady Aerodynamics, Aeroacoustics and Aeroelasticity of Turbomachines*. Springer, 2006, pp. 31–40.

[66] Kenneth C Hall and Christopher B Lorence. "Calculation of three-dimensional unsteady flows in turbomachinery using the linearized harmonic Euler equations". In: *Journal of Turbomachinery* 115.4 (1993), pp. 800–809.

[67] Zoe Burton. "Analysis of low pressure steam turbine diffuser and exhaust hood systems". PhD thesis. Durham University, 2014.

[68] KTH. *3D Steam Turbine Flutter Test Case*. url: `%5Curl%7Bhttps://www.kth.se/en/itm/inst/energiteknik/forskning/kraft-varme/ekv-researchgroups/turbomachinery-group/aeromech-test-cases/3d-steam-turbine-flutter-test-case-1.706654%7D` (visited on 2019).

[69] Paul Petrie-Repar et al. "Advanced flutter analysis of a long shrouded steam turbine blade". In: *ASME Turbo Expo 2014: Turbine Technical Conference and Exposition*. American Society of Mechanical Engineers. 2014, V07BT35A022–V07BT35A022.

Appendix A

Flutter Wizard flow chart: Case B

Figure A.1 displays the workflow of the flutter wizard case B, which is initialized by a given Harmonic simulation. This layout is very similar to case A, but there are two blocks, named B1 and B2. These blocks retrieve the steady state simulation and the prescribed NLH settings from the unsteady case. Afterwards the already existing blocks are used to accomplish case B.

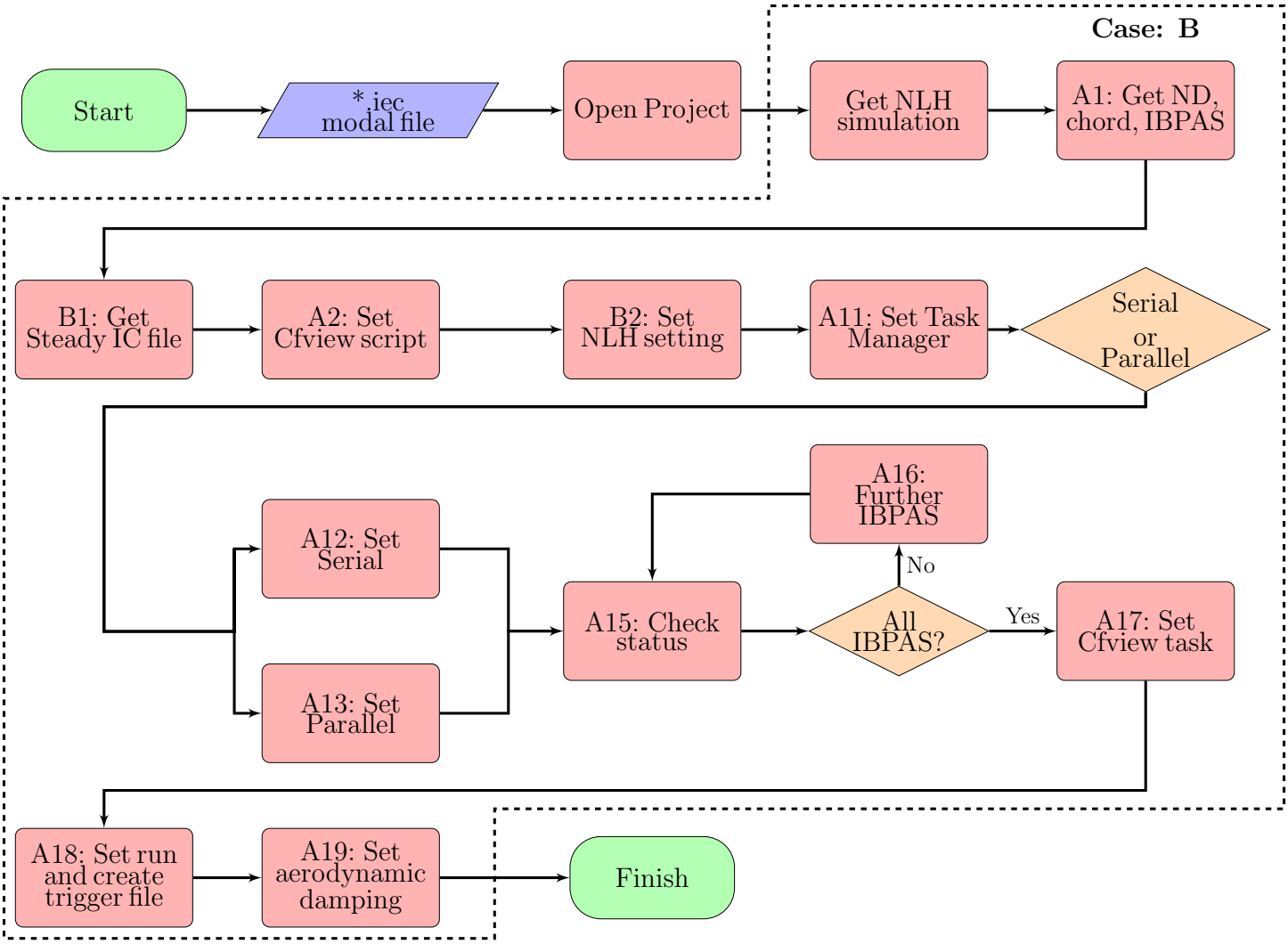

Figure A.1: Flutter Wizard Flow chart: Case: B

Appendix B

STCF11 Harmonic displacement

Figure B.1 displays, the harmonic content of the displacement modulus along the pressure and suction side. The selected contour allows to identify the harmonic displacement variations, in particular at the hub. At the hub, there is a clear trend of harmonic oscillations in the displacement as shown with red arrows. These oscillations, produce harmonic variations in all subsequent harmonic properties over the blade, such as the harmonic pressure. The harmonic pressure variations are reflected in the harmonic pressure coefficient and the phase. This peaks variations are assumed to be due to the interpolation of the modal properties into the CFD mesh. The harmonic trend observed is directly related to the amount of data provided by the modal displacement, as this effect was not found in Chapter 6.

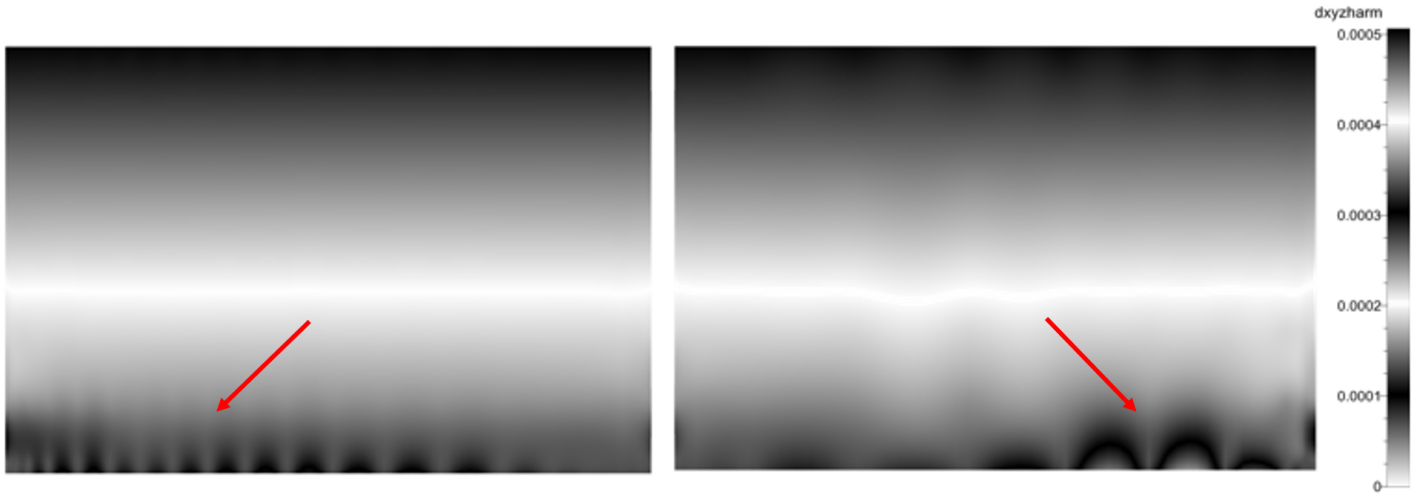

Figure B.1: Harmonic displacement *waves* at PS and SS

Appendix C

Expert parameters

When making use of the CPU-booster from FINE™/Turbo within a computation, some oscillations of residuals and in consequence of physical properties occur. The stability of the result were controlled with the following solver parameters, which were modified based on the best practices within NUMECA International. A full description of these parameters can be found in the User and Theory Guide [56], [64]. Thus, the convergence was enhanced but this did not produce any significant change in the global results compared to a case without these modified parameters. A summary of the effect of the modified parameters is shown below:

1. In order to enforce that there is a zero modal displacement between the solid boundaries and the moving surfaces at its connections regions CORMOD parameter needs to be activated

2. In order to control the harmonic oscillations due to harmonic pressure gradients. This is done by setting a pressure sensor type (HAVMOD) and a harmonic sensor pressure coefficient (HARAV2) that controls the variation of the second difference artificial dissipation into the time-mean and harmonic equations, needed to be modified to 3 and 1e-3 respectively

3. Physically, in order to allow the blade vibration there is a blade tip gap, in which the mesh in this region can be set to move as the surrounding domain, allowing a better mesh quality. This configuration is activated by MVGAP parameter

4. In order to include the physical, viscous dissipation, and the artificial dissipation in the Runge-Kutta dissipation terms, the IBOTH expert parameter is activated

5. The dissipation along the physical boundaries and removing fourth order dissipation near the walls is controlled by IDISMO expert parameter which was set to 42

6. Finally, to control the dissipation coefficients of the second and fourth order in the central scheme, the expert parameteres VIS2 and VIS4 were set to 0.5 and 0.05 respectively